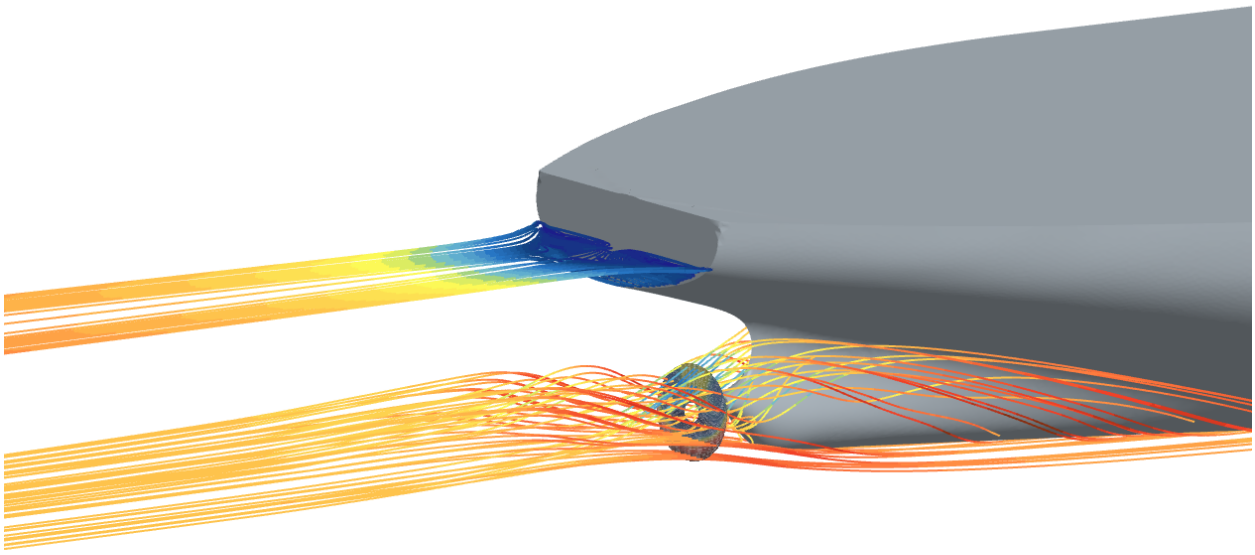

Systematic Analysis of Scale Effects on Form Factor

Master's thesis in Maritime Engineering

MINAS ARGYROS

DEPARTMENT OF MECHANICS AND MARITIME SCIENCES

CHALMERS UNIVERSITY OF TECHNOLOGY
Gothenburg, Sweden 2023
www.chalmers.se

DEPARTMENT OF MECHANICAL ENGINEERING

TECHNICAL UNIVERSITY OF DENMARK
Kongens Lyngby, Denmark 2023
www.dtu.dk

Master's thesis 2023

Systematic Analysis of Scale Effects on Form Factor

MINAS ARGYROS

Department of Mechanics and Maritime Sciences
Division of Marine Technology

Chalmers University of Technology
Gothenburg, Sweden 2023

Department of Mechanical Engineering
Section of Fluid Mechanics, Coastal and Maritime Engineering
Technical University of Denmark
Kongens Lyngby, Denmark 2023

Systematic Analysis of Scale Effects on Form Factor
MINAS ARGYROS

Supervisors:

Arash Eslamdoost, Associate Professor at Department of Mechanics and Maritime Sciences, Division of Marine Technology, Chalmers University of Technology

Yanlin Shao, Associate Professor at Department of Civil and Mechanical Engineering Section of Fluid Mechanics, Coastal and Maritime Engineering, Technical University of Denmark

Simone Mancini, Senior Team Leader at Department of Hydro and Aerodynamics, FORCE Technology

Master's Thesis 2023
Department of Mechanics and Maritime Sciences
Division of Marine Technology
Chalmers University of Technology
SE-412 96 Gothenburg
Telephone +46 31 772 1000

Department of Mechanical Engineering
Section of Fluid Mechanics, Coastal and Maritime Engineering
Technical University of Denmark
2800 Kgs. Lyngby
Telephone +45 45 25 25 25

Cover: Visualization of the flow in the wake of transom and propeller disc of the KVLCC2 benchmark hull.

Typeset in LaTeX
Printed by Chalmers Reproservice
Gothenburg, Sweden 2023

Systematic Analysis of Scale Effects on Form Factor

MINAS ARGYROS
Department of Mechanics and Marine Sciences
Division of Marine Technology
Chalmers University of Technology

Abstract

The purpose of the present master thesis is to investigate the difference between model scale and full scale form factor Computational Fluid Dynamics (CFD) computations, using a new established method. This method called the two-form factor method (or 2-k method) exposed in two recent research papers shows improvements in the accuracy of form factor estimation, providing consequently better results by applying the full scale process, especially in case of stern flow separation phenomena, such as bubble type flow separation and recirculation type flow separation. The present master thesis will investigate this form factor procedure using five benchmark hulls, as well as two commercial hulls being provided by the database of FORCE Technology with the aim of having better insights about the aforementioned investigated phenomena. First of all, Verification and Validation (V&V) of the CFD results is executed by comparing the CFD form factor results obtained with the available model scale experimental results. Furthermore, a systematic analysis of changing the scale factor of the test cases is applied in order the scale effects to be studied. Moreover, sensitivity analysis of different roughness heights is implemented so as the effect of the equally distributed roughness to be investigated in full scale CFD computations. All in all, implementing the systematic analysis in scale, roughness and draft variations, the results show that the two form factor method is considered an holistic and trustworthy method which can provide reliable prediction of form factor even for the case of intense turbulence phenomena in the wake of transom.

Keywords: CFD, Systematic analysis, Scale effects, Form factor, 2-k method

Preface

The present thesis is submitted as partial fulfilment of the requirements for the double degree of Nordic Master in Maritime Engineering at the Chalmers University of Technology, Gothenburg, Sweden and Technical University of Denmark (DTU), Lyngby, Denmark.

The work has been performed over the time period January 2023 to June 2023. The project was carried out at the Division of Marine Technology at the Department of Mechanics and Maritime Sciences of Chalmers University of Technology with cooperation with FORCE Technology. The thesis has been supervised by Arash Eslamdoost (Chalmers), Yanlin Shao (DTU) and Simone Mancini (FORCE).

Minas Argyros

Gothenburg, Sweden
June 2023

Acknowledgements

Of the many people who helped me during this master thesis, I would first like to thank my two supervisors, Arash Eslamdoost and Yanlin Shao for their guidance and support as well as for the precious discussions we had throughout the present project. I would like also to thank Claus Simonsen and Simone Mancini, who gave me the opportunity to be engaged with such an interesting and challenging topic, which can be considered as one of the most topical subjects in the field of Computational Fluid Dynamics and Ship Hydromechanics. Moreover, I feel grateful that they share state-of-the-art knowledge of numerical modelling and the maritime world.

Furthermore, I would like to express my sincere gratitude to Pablo Esquivel de Pablo for his help, guidance, as well as for giving me precious tips and advice as far as the execution of the simulations are concerned. Furthermore, I would like to express my acknowledgements to Janne Flensborg Otzen for offering me valuable experimental results from the database of FORCE Technology, which were used as the main comparative data with the one extracted from the CFD simulations. Also, I would like to thank Rui Miguel Alves Lopes, who had the willingness and provided me his help during the post-process of the results of my thesis.

Last but not least, I would like to thank my parents, who gave me the chance to experience this beautiful journey of the last two years and open the path for the upcoming ones.

Minas Argyros, Gothenburg, June 2023

List of Acronyms

Below is the list of acronyms that have been used throughout this thesis listed in alphabetical order:

AHR	Average Hull Roughness
ATTC	American Towing Tank Conference
BL	Boundary Layer
BPG	Best Practice Guideline
CFD	Computational Fluid Dynamics
DB	Double-Body Model
DFBI	Dynamic Fluid Body Interaction
DNS	Direct Numerical Simulation
DoF	Degrees of Freedom
DTMB 5415	US Navy Combatant
DWT	Deadweight Tonnage
EFD	Experimental Fluid Dynamics
ESD	Energy Saving Device
FS	Full Scale
F-S	Free-Surface Model
GCI	Grid Convergence Index
IMO	International Maritime Organization
ITTC	International Towing Tank Conference
JBC	Japan Bulk Carrier
KCS	Kriso Container Ship
KVLCC2	MOERI Tanker KVLCC2
LSR	Least Squares Root
MS	Model Scale
ONRT	ONR Tumblehome Ship
RANS	Reynolds-Averaged Navier-Stokes
RE	Richardson Extrapolation
RZ	Refinement Zone
SST	Shear Stress Transport
TEU	Twenty-foot equivalent unit
VoF	Volume of Fluid
V&V	Verification and Validation
2D	Two-dimensional
2-k	Two form factor

Nomenclature

Below is the nomenclature of indices, Latin and Greek letters that have been used throughout this thesis.

Indices

d	Disturbed waves
i,j	Indices for three spatial directions
I	Incident waves
S	Index for full scale
M	Index for model scale

Latin Letters

A_{max}	Maximum cross-section area for a given draft	$[m^2]$
A_{tr}	Area of the submerged transom	$[m^2]$
B	Beam of ship	$[m]$
C	Resistance coefficient	[-]
C_A	Correlation coefficient	[-]
C_{AAS}	Air resistance coefficient	[-]
C_B	Block coefficient	[-]
C_F	Frictional resistance coefficient	[-]
C_R	Residuary resistance coefficient	[-]
C_T	Total resistance coefficient	[-]
C_V	Viscous resistance coefficient	[-]
C_W	Wave resistance coefficient	[-]
$\vec{F}$	Force vector	[N]
Fn	Froude number	[-]
g	Gravitational acceleration	$[m/s^2]$

k	Form factor	[-]
k_e	Turbulence kinetic energy	$[m^2/s^2]$
k_s	Nikuradse's equivalent sand roughness	[m]
l^*	Non-dimensional cell size	[-]
L_{OA}	Overall length of ship	[m]
L_{PP}	Length between perpendiculars	[m]
L_{WL}	Waterline length of ship	[m]
n	Number of cells	[-]
N	Number of layers	[-]
p	Pressure	[Pa]
p_∞	Static freestream pressure	[Pa]
p	Observed order of grid convergence	[-]
R	Discrimination ratio	[-]
R	Resistance	[N]
R_{AWL}	Added resistance due to waves	[N]
R_F	Frictional resistance	[N]
R_s^+	Equivalent sand-grain roughness height	[m]
R_T	Total resistance	[N]
R_V	Viscous resistance	[N]
R_W	Wave making resistance	[N]
Re	Reynolds number	[-]
S	Wetted surface area	$[m^2]$
$S_{i,j}$	Rate of strain tensor	[-]
t	Time	[s]
$tr_{fullness}$	Fullness of wetted-transom	[-]
tr_{ratio}	Area ratio of wetted-transom	[-]
t^*	Non-dimensional time step	[-]
t_0	Near wall thickness	[m]
T_{AP}	Draft at aft perpendicular	[m]
T_b	Ballast draft	[m]
T_{Design}	Design draft	[m]
T_m	Draft amidships	[m]
T_s	Scantling draft	[m]
T_H	Total thickness of boundary layer	[m]
T_{FP}	Draft at fore perpendicular	[m]
U	Velocity vector	$[\frac{m}{s}, \frac{m}{s}, \frac{m}{s}]$

U_r	"Imaginary" force used for water-air fraction in VoF method	$[N]$
u_*	Frictional velocity	[m/s]
$u^{'}$	Fluctuating part of velocity	[m/s]
V	Speed	[m/s]
V_∞	Freestream fluid velocity	[m/s]
y	Distance to wall	[m]
y^+	Non-dimensional wall distance	[-]
y_{tr}	Transverse dimension of wetted-transom	[m]
x	Spatial direction	[m]
X	First cell thickness	[m]

Greek Letters

	Smooth wall log-law intercept	[-]
$\delta_{i,j}$	Kronecker delta	[-]
ΔC_F	Roughness allowance coefficient	[-]
ΔU^+	Roughness function	[-]
ϵ	Dissipation rate	$[m^2/s^3]$
∇	Volume displacement	$[m^3]$
κ	von Karman constant	[-]
λ	Model-ship scaling factor	[-]
λ_s	Stretch ratio	[-]
μ	Dynamic viscosity	$[Ns/m^2]$
μ_t	Eddy viscosity	$[Ns/m^2]$
ν	Kinematic viscosity	$[m^2/s]$
ρ	Fluid density	$[kg/m^3]$
σ	Viscous stresses	$[N/m^2]$
τ_w	Wall shear stress	[Pa]
ω	Specific turbulence dissipation rate	$[s^{-1}]$

Contents

List of Figures

List of Tables

1

Introduction

During the preliminary design phase of a ship, it is of high importance for the designer to obtain a precise and trustworthy estimation of its performance. The precise prediction is essential with the aim of ensuring achievement of prescribed requirements, minimizing the entire cost of building and operating the ship, as well as designing an eco-efficient ship. The stricter and stricter regulations applied from regulatory bodies for a more sustainable and greener future set the eco-efficiency as a necessary and unavoidable factor for maritime sector.

According to the long-time tradition and knowledge, hydrodynamic testing is the main method to evaluate the performance of a ship. The hydrodynamic tests take place on a model scale version of the real vessel. The aforementioned tests are implemented in towing tanks, which are large basin of water. These tests are applied under controlled conditions. As this type of testing constitutes an old tradition in the field of ship hydrodynamics, an immense experience and knowledge has been obtained, collecting a huge database of ship models, measurements and statistics. Collecting all these precious information about ship hydrodynamics, standard procedures for carrying out towing tank tests have been developed. The association, which is responsible for their organisation and publication is the International Towing Tank Conference (ITTC).

The estimation of ship resistance via towing tank tests conceals essential shortcomings. One shortcoming is the fact that the viscous effects in model scale are not the same as in full scale. The development of extrapolation processes can be considered as solution to this problem. Specifically, these processes separate the components of resistance and scale them individually. The main purpose of the extrapolation methods is the extraction of a more accurate performance prediction of the full scale ship. On the other hand, Computational Fluid Dynamics (CFD) constitutes an alternative way of evaluating the ship resistance. Specifically, through a CFD analysis the set of governing equations, which represent the flow, are solved numerically. In the course of time, CFD is a more and more viable pathway for the designers, as the computational power has rapidly increased.

It is a fact that CFD provides advantages, but it conceals drawbacks as well. The main advantage of CFD is the capability of running full scale simulations, avoiding the risk of errors of the extrapolation from model to full scale. Moreover, precious information of the flow, which can be derived from a CFD simulation, is another positive point of choosing CFD analysis. In contrast to the advantages of CFD, it may have negative impact to the extracted results due to the modelling errors. These errors occur, because the flow physics are simplified, such as use of wall function for representation of turbulence effects in the boundary layer [Mikkelsen H.,L. et al. (2019)].

According to form factor estimation, except for its experimental determination using methods, such as Hughes [Hughes G. (1954)] and Prohaska [Prohaska C. W. (1966)], research studies have presented the last few years that CFD computations as they can handle the scale effects by the Experimental Fluid Dynamics (EFD) can estimate form factor with a combined EFD&CFD method, called

two form factor method [Korkmaz K.B. et al. (2020), Korkmaz K.B. et al. (2022)]. In that case the combination of CFD and EFD on their robust points can lead to a better estimation of form factor and consequently a more accurate power prediction. Finally, a substitute or supplemental method to the Prohaska one is the double body Reynolds-Averaged Navier-Stokes (RANS) computations. Regarding this method, it can duplicate the conditions included in the primary form factor hypothesis while being straightforward in numerical modelling [Korkmaz K.B. (2022)].

1.1 Literature Review

The issue of estimating a ship's form factor and associated scale effects is one of the main topics to many research investigations in recent years. It have been proved that the 1978 ITTC Power Prediction method perform several strict criteria. Such criteria are the viscous pressure resistance coefficient C_{PV} is proportional to the frictional resistance coefficient C_F when turbulence and free form separation is performed, as well as the hull is smooth and symmetrical when towed at zero incidence angle [Korkmaz K.B. et al. (2022)]. Furthermore, the most common method for the determination of form factor is the Prohaska's method (1966). Since this method is based on the assumption that the wave resistance coefficient C_W is proportional to the fourth power of Froude number, there is a percentage of uncertainty that the measurement points do not lie on the resulted straight line. Therefore, the Prohaska method cannot be considered as completely precise.

Except for the previous argument about the criteria of the ITTC standard procedure, the importance of establishing an accurate computational method for estimating the form factor numerically is considered crucial, as it constitutes one of the most decisive factors for the hull performance of a ship and its propulsive power. Based on research studies, which have been published, the CFD-based form factor is closely dependent to scale factor, speed of vessel, turbulence model, as well as it presents dependence of geometrical aspects, such as position and shape of the transom and bulbous bow. The present master thesis is based on the shortcomings of four specific research papers. A general overview about the scope and recommendations, which have being proposed in each of them, is presented below.

First of all, the two form factor method, which is going to be used in the context of this thesis is calculated twice in both model and full scale. Otherwise, using the same form factor for both cases will lead to an under-prediction of the full-scale viscous resistance [Korkmaz K.B. et al. (2022)]. As it is further discussed in Section 2.2.3.2, decomposition of the viscous resistance coefficient C_{PV} is implemented into viscous resistance proportional to frictional one of a friction line and the flow behind the transom. According to this approach, the flow behind the wet transom is considered crucial and this is the reason of the aforementioned decomposition of viscous resistance. This study [Korkmaz K.B. et al. (2022)] indicated that the precision of the prediction of form factor is improved in comparison with the standard ITTC-78 method. This paper proposes that further investigations of more test cases can be performed for hulls with extensive transom submergence with availability of speed trials.

Based on the second investigation being published [Korkmaz K.B. et al. (2020)], the main scope is the attempt of introducing a combined EFD&CFD method, in which double body RANS computations are used for the benchmark hulls KVLCC2 and KCS, taking into account towing tank test of KVLCC2 and an experimental uncertainty analysis for the form factor. The results of this study present that Prohaska method is considered to be deficient, due to the invalidity of its proposed

linear correlation of the experimental data in case of bulbous bow hull designs and because of the increased experimental uncertainty of form factor when the regression analysis is applied. After execution of simulations and validation of the extracted results, it is proposed that the use of combined EFD&CFD and CFD-based form factor can be "an alternative or supplementary method to the Prohaska method" [Korkmaz K.B. et al. (2020)].

In addition to the previous research projects, another study implemented tries to explore numerically the dependence of form factor through the change of vessel speed and turbulence model, making use of a RANS solver [Terziev M. et al. (2021)]. The investigation indicates that the form factor is sensitive to low speeds, regarding the scale factor and turbulence model used. For higher speeds, the form factor displays negligible variations. Consequently, the form factor is considered Froude-dependent via change in the magnitude of Reynolds number Re. Based on the aforementioned paper, to fully determine and obtain more insight of scale effects on form factor, further investigation of Froude (Fn) and Re number dependencies should be implemented, even though several studies have examined the scale effects the last years.

The fourth and last paper taken into account as one of the main references in the context of this thesis presents the study of improved power prediction via combined EFD&CFD method and double body RANS computations, executing also systematic variations to the different CFD set-ups [Korkmaz K.B. et al. (2021)]. Through this investigation, it is proved that combining EFD and CFD provides more accurate estimation on form factor and, consequently, on propulsive power within the range of the studied cases, as well as offers improvements to ITTC-78 method. Due to the uncertainty of the speed trials, more investigations can be performed with more test cases for the comparison of power predictions and speed trials with the CFD-based form factor estimations.

All the aforementioned studies make an attempt to provide an improved estimation on form factor using a combined EFD&CFD method and CFD-based computation. The primary scope of these investigations is a more trustworthy prediction of the performance of ships, which constitutes a vital point for shipowners and generally shipping industry. However, shortcomings and lack of validated data are included in these studies. These mentioned shortages are referred to the high scarcity and uncertainty of sea trial data, the low number of test cases being already examined, the lack of investigation of hulls with large transom submergence and a different CFD set-up, which could provide updates in the current research.

1.2 Scope and Research Question

The scope of the present thesis is an extensive systematic investigation and analysis of the resulted discrepancies, which occur from simulations for CFD-based form factor estimations between model and full-scale computations. The selected studied geometries are five benchmark hulls of Japan Bulk Carrier (JBC) [JBC, Tokyo (2015)], Kriso Container Ship (KCS) [KCS, Tokyo (2015)] and MOERI KVLCC2 [KVLCC2, Tokyo (2015)], US Navy Combatant (DTMB 5415) and ONR Tumblehome Ship (ONRT), as well as two commercial bulk carriers from the database of FORCE Technology, the 180K BC and the 82K BC. The aforementioned investigation is based on a newly established methodology developed the last years and presented by two research publications, which are [Korkmaz K.B. et al. (2020), Korkmaz K.B. et al. (2022)]. The results of these two studies demonstrate improvements in the precision of form factor prediction, providing also upgrades in the procedure of extrapolation of rest of the results from model to full scale. For reasons of validation and verification the extracted CFD results are compared with model scale experimental ones.

The main research question addressed in this master thesis is formulated as follows:

How is the form factor obtained from CFD simulations using 2-k approach influenced by scale effects, hull roughness and draft variations?

The concentration of this research question lies on the procedure of a systematic investigation of sensitivity on CFD-based form factor. Answering the research question is intended to provide an understanding of which are the possible shortcomings with full scale form factor predictions, which is a fact that can lead to uncertainties in full scale resistance estimations. By making use of the two form factor method is expected to provide also essential improvements to the 1978 ITTC Performance Prediction Method [ITTC (1978)]. Secondly, this thesis constitutes a further study to the ones being already published [Korkmaz K.B. et al. (2020), Korkmaz K.B. et al. (2022)] with more test cases and CFD codes in order to add better insights about the dependency of the combined EFD&CFD two form factor method. Finally, main parameters of existing vessels are studied with the aim of being compared with the CFD-based form factors. The referred data of existing ships are provided from the database of FORCE Technology.

1.3 Limitations

The preparation and execution of the CFD simulations in FORCE Technology represented the first two month on the five-month timeline of the master thesis. Even though the primary scope of the thesis was resistance simulations to be also studied and given that the duration of the present project was limited, the whole focus of the thesis is concentrated on the study of form factor. Furthermore, the fact that commercial data from existing ships could not be used, the entire study is limited to the five benchmark hulls and some basic parameters of several existing hulls.

1.4 Structure of the Thesis

The thesis is composed of five chapters. The current chapter presents a general background, the main aim, the research question and the existing limitations of the project. In the next chapter, the theoretical background related to the present topic is introduced. The resistance components, details of the extrapolation methods and numerical modelling are presented. In the third chapter the main points of the methodology used are presented, such as the test cases, the two form factor method, the double body Reynolds-Averaged Navier-Stokes (RANS) computations and the set-up of the CFD simulations. All the results of the test cases and investigations on CFD-based form factor are covered in the fourth chapter. Finally, the last chapter is dedicated to the presentation of summary of entire thesis, conclusions and recommendations for future work.

2

Theory

The present chapter introduces briefly the theory which serves as the foundation for this master thesis. In Section 2.1, the total ship resistance with its components is presented. Afterwards, Section 2.2 introduces the theoretical background and different ways of extrapolating the resistance of ship from model to full scale. Last but not least, the stages of numerical modelling is introduced in Section 2.3, which are considered the basis of the CFD simulations executed in the context of the this project.

2.1 Resistance Components

In order to comprehend the physical meaning of form factor, the presentation of the total ship resistance in calm water, which is divided into several components, is necessary. The total calm water resistance R_T of a ship can be split up with numerous ways. The most common way is to designate the total resistance as the summation of the frictional R_F and pressure R_P resistance. The former resistance component represents the shear forces acting tangential to the ship surface, while the latter component is the normal forces acting perpendicular the surface of ship. The dominant component of resistance in low speeds is the frictional, while the pressure forces dominate in higher speeds, because of the generation of waves.

Generally, the components of calm water resistance can be divided more into the contributions shown in Figure 2.1. From this figure, it is obvious that the two fundamental resistance components (pressure and frictional) are divided further into viscous effects and wave-making resistance. Therefore, the following two expressions Equations 2.1 and 2.2 are introduced:

$$R_T = R_F + R_P \tag{2.1}$$

$$R_T = R_V + R_W \tag{2.2}$$

According to viscous effects, they are formed due to the skin friction and the form and eddy-making resistance. Regarding the first contributor, the viscosity of a real fluid, such as sea water, gives rise to frictional forces between the particles of fluid, if they move relative to each other. Furthermore, the particles, which are adjacent to the hull, are attached into it and have the same velocity as the vessel. With regard to the form and eddy-making resistance, the fluid particles along the hull present fluctuations in velocity compared to free-stream velocity. Alternatively, the fluid particles near the hull will move faster, because they traverse longer distance and, therefore, the frictional resistance increases [Carlton J. S. (2019)].

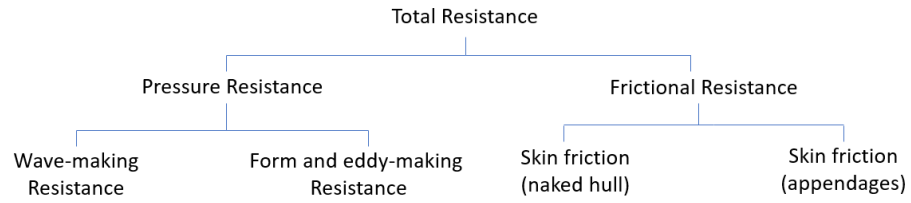

Figure 2.1: Components of ship resistance. [Carlton J. S. (2019)]

2.2 Extrapolation Methods

As it is mentioned in Chapter 1, the prediction of ship performance plays the most essential role in the design phase, because it includes not only the holistic behavior of ship in sea, such as sea-keeping, maneuverability, heave/pitch responses etc., but also gives an estimation about the fuel consumption of ship. For this specific reason, EFD provides a unique data set for a hull form and its propulsive characteristics. As long as the mentioned data sets refer to models tested in towing tank, the estimation of the full scale ship must be obtained via extrapolation procedures. By establishing precise methods, assumptions and testing techniques, William Froude is considered as the pioneer of ship performance prediction. After decades, ITTC introduces standardization and improvements regarding the model testing and extrapolation processes.

According to the primary estimation methods, scaling of self propulsion tests and use of correction factors evaluate the power and propeller rotational rate. In 1969, ITTC demonstrates that the prediction methods differ for each research center regarding the implementation of new concepts and correlation formulas, such as form factor, roughness allowance and friction line. Consequently, it is decided that the several procedures were to be collected and compared and a common methodology to be introduced for ship-model correlation studies in the future [ITTC (1969)]. Several institutions of ITTC assess the software developed by SSPA [SSPA] in 1973, where they have used different assumptions and extrapolation methods. This assessment is based on the comparison between power and propeller rotational rate with speed trials [ITTC (1978)]. The ITTC-78 has gathered and compared one thousand sea trials with model test predictions [Korkmaz K.B. (2022)], while after multiple revisions made for the primary method by applying a new formula for calculation of correlation allowance and air resistance, as well as updating the roughness allowance, the ITTC-78 is still applied for more than four decades [ITTC (Revision 2017) (1978)].

In order to introduce and review the friction line and the form factor in Section 2.2.2 and Section 2.2.3, the full scale ship resistance [ITTC (Revision 2017) (1978)] is presented in Equation 2.3.

$$C_T = (1+k)C_{FS} + C_A + \Delta C_F + C_R + C_{AS} \tag{2.3}$$

where k is the form factor, C_{FS} is the friction resistance coefficient (full scale), C_R is the residual resistance coefficient, ΔC_F indicates the roughness allowance, C_A the correlation allowance and C_{AAS} is the air resistance coefficient.

2.2.1 Model-Ship Scaling

The hydrodynamic motions and forces of ship are used to be measured in model scale, implementing experimental tests in water basins. Therefore, it is mandatory for the model to be geometrically similar to the ship. This procedure cannot be considered an easy task, since the definition of the model speed and the way of scaling the resulted forces require accuracy in the extrapolation phase. The scaling of the velocities and forces is implemented through kinematic and dynamic similarity procedures, respectively. Specifically,

1. **Geometric similarity** defines that the model and the ship must have exactly the same configuration (excluding roughness effect).
2. **Kinematic similarity** determines that all components of velocities in the flow have been scaled by the same scale factor (geometrically similar streamlines).
3. **Dynamic similarity** advocates that all components of forces in the flow have been scaled by the same scale factor (same orientation of force vectors).

These three categories of similarity are based on the method of dimensional analysis. Via this method, non-dimensional quantities are extracted and they are important for scaling from model to full scale. As the dimensional analysis method is out of the scope of this thesis, it is not presented in detail. As a brief reference, the several quantities are converted into non-dimensional using the ship speed V, the kinematic viscosity of fluid ν, the gravitational acceleration g and the length between perpendiculars of ship L_{PP}.

The scale factor between model and full scale is determined as the ratio of a characteristic length of the full scale ship L_S over a characteristic length of the model scale ship L_M (Equation 2.4) [Mikkelsen H.,L. et al. (2019)].

$$\lambda = \frac{L_S}{L_M} \tag{2.4}$$

The two most essential non-dimensional parameters in experimental testing and ship hydrodynamics are Fn and Re, which play crucial role in the form factor methodology (Section 2.2.3), the expressions of which is presented in Equation 2.5 and Equation 2.6, respectively [Larsson, L. et al. (2010)].

$$Fn = \frac{V}{\sqrt{gL_{PP}}} \tag{2.5}$$

$$Re = \frac{VL_{PP}}{\nu} \tag{2.6}$$

Finally, the non-dimensional resistance coefficients C of each resistance component R are normalized dividing the resistance components over the fluid density ρ, the wetted surface area S and the speed V, as it is represented below in Equation 2.7.

$$C = \frac{R}{\frac{1}{2}\rho S V^2} \tag{2.7}$$

2.2.2 Friction Line

Taking into consideration the Equation 2.3 in Section 2.2, which represents the division of total full scale ship resistance into the several components, the two most debated but vital components are

the C_F and C_R. Based on the Froude method, the total model scale resistance is comprised of these two aforementioned coefficients introduced in Equation 2.8.

$$C_{TM} = C_R + C_{FM} \tag{2.8}$$

Specifically, the Equation 2.8 above indicates that the C_F of a flat plate corresponds equally to the C_F of a ship, while the rest percentage of the C_T is equal to the residual resistance, which has exactly the same value in model and full scale. Consequently, it is obvious that the frictional resistance plays essential role in the resistance predictions. In that point, an historical overview is introduced.

In the beginning of 20^{th} century, most of tests were implemented with flat plates and they were according to the Froude methodology. Schoenherr introduced a correlation formula, running plank tests and collecting the results of these experiments in 1932 [Larsson, L. et al. (2010)]. The total resistance for surfaces with different characteristic lengths was derived via integration of the results and, therefore, Schoenherr fitted the formula presented in Equation 2.9 to the extracted data, including the Re for the first time and achieving apparent improvement [Larsson, L. et al. (2010)].

$$\frac{0.242}{\sqrt{C_F}} = log(ReC_F) \tag{2.9}$$

In 1947, American Towing Tank Conference (ATTC) adopted the formula of Schoenherr. The main drawback of Schoenherr formula was the shortcoming of providing valid correlation between the results of small and large models. In order to improve the existing data, Hughes implemented resistance tests reaching values of $Re = 3 \cdot 10^8$ [Hughes G. (1952), Hughes G. (1954)]. The tested surfaces were of a broad range of aspect ratios (fraction of plank's beam over its length) and Hughes managed to extrapolate the resistance coefficients in two dimensional (2D) flow, giving the formula in Equation 2.10.

$$C_F = \frac{0.066}{(logRe - 2.03)^2} \tag{2.10}$$

Not being able to take into account the viscous effects, the ITTC made certain corrections so as the form effect of modern ships to be included introducing the "ITTC-57 model-ship correlation line" (Equation 2.11).

$$C_F = \frac{0.075}{(logRe - 2)^2} \tag{2.11}$$

The last decades, numerical methods have been applied to obtain a formula for the resistance of flat plates. Several studies have used different techniques, such as use of the wall-wake law and the momentum integral equation [Grigson C. W. B. (1993) , Katsui T. (2005)] or using RANS equations [Eça L. et al. (2002)]. The most reasoned study is considered the one from Eca & Hoekstra, who managed to include in their computations the skin friction as function of Re. A graphical representation of friction lines extracted from the three approaches presented above is displayed in Figure 3.2 in order a comparison of the results among the aforementioned approaches to be seen. It is apparent that the higher divergence among the frictional resistance coefficients of the three approaches occurs for low values of Re.

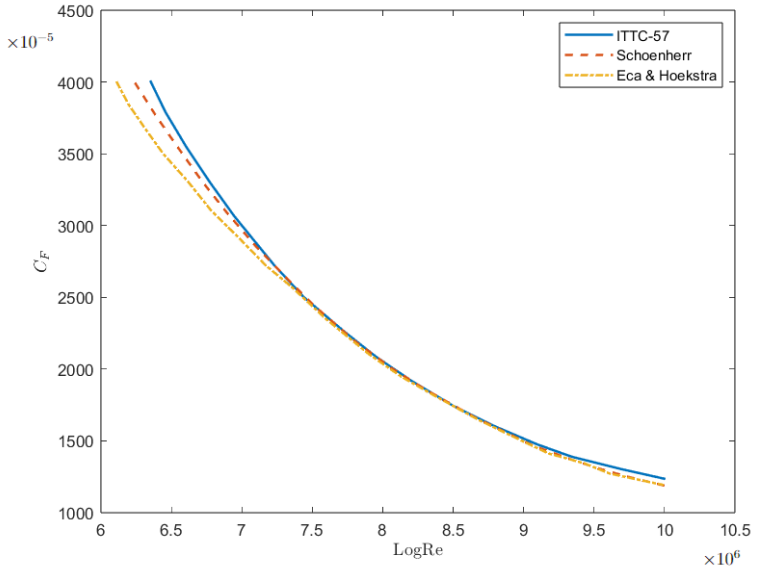

Figure 2.2: Friction lines. [Larsson, L. et al. (2010)]

2.2.3 Form Factor

The main concept of the form factor is the need of having different "extrapolator" for each hull, without being based on an unique 2D flow analysis, such as Froude method. This issue is under consideration from the beginning of the previous century. Moreover, the extrapolation of the resistance from model to full scale must include also the effects of three-dimensional flow [Korkmaz K.B. (2022)], since the 3D frictional resistance of the hull surface cannot be the same as the 2D frictional resistance of a flat plate. On the other hand, the contribution of the hull shape is included implicitly in the C_R, while the C_R is not affected when it is scaled up from model to full scale at the same Fn number, as long as C_R is a function of Fn number $C_R(Fn)$. According to Hughes [Hughes G. (1954)], the residual resistance can be divided into C_{PV} and C_W. Given that C_{PV} constitutes a constant percentage of C_F, only the C_W is scaled up with Fn. Therefore, based on all the aforementioned points, Equation 3.24 [[Korkmaz K.B. et al. (2020)], Eq. (1)] gives the total resistance.

$$C_T = C_F + C_{form} + C_W \tag{2.12}$$

In Equation 3.24, C_{form} represents the form resistance because of the hull shape and it is proportional to C_F when the flow does not have separation and it is turbulent, the hull is smooth and it is symmetrical when it is towed at zero incidence angle. Furthermore, the eddy-making resistance and the added skin friction from curvature effects lead to the inclusion of form resistance [Korkmaz K.B. et al. (2021)]. In Equation 2.13 [[Korkmaz K.B. et al. (2020)], Eq. (1)], the linear relation between the C_{form} and C_F is presented.

$$C_{form} = kC_F \tag{2.13}$$

Regarding the Equation 2.13, the form factor is considered as the percentage of frictional resistance due to the shape of the hull. For this specific reason, to calculate the form factor in a towing tank, the carriage tows the model in low speeds (e.g $Fn < 0.15$) where the wave resistance is negligible. However, the central problem with running a model in low speed is the development of laminar flow, where the forces are extremely small and the measurements can be inaccurate. Therefore, the

CFD-based approach can be considered as a more precise method for the determination of form factor.

In Section 2.2.3.1 and Section 2.2.3.2 which follow, two different approaches for the determination of form factor are presented. Specifically, in Section 2.2.3.2 the two form factor (2-k) method is introduced, which constitutes the main "tool" of the simulations of this thesis.

2.2.3.1 Experimental Determination of Form Factor

The determination of form factor in experiment-wise approach is applied with three different approaches.

First of all, to derive a first estimation of form factor, Watanabe [Watanabe K. (1973)] introduced an empirical expression (Equation 2.14) [[Larsson, L. et al. (2010)], Eq. (8.18)], which is the most widely used.

$$k = -0.095 + 25.6 \cdot \frac{C_B}{(\frac{L_{PP}}{B})^2 \sqrt{\frac{B}{T}}} \tag{2.14}$$

where C_B is the block coefficient, L_{PP} is the length between perpendiculars, B is the beam and T the draft. It is noted that the aforementioned expression is used only in conjunction with the ITTC-57 formula (Equation 2.11).

As it is referred in Section 2.2.3, another possible way to define the form factor is by running the model at low speed taking into account only the frictional contribution in total resistance, where $C_W = 0$ and C_F is computed by the ITTC-57 formula (Equation 2.11). Therefore, the form factor is estimated by the following ITTC-78 expression (Equation 2.15) [ITTC (Revision 2017) (1978)].

$$C_T(Re, Fn) = (1 + k)C_F(Re) + C_W(Fn) \tag{2.15}$$

In Figure 2.3 the depicted plot corresponds to the definition of form factor in low speed, in which the friction coefficient line, the viscous coefficient line and measured points of the total resistance are illustrated.

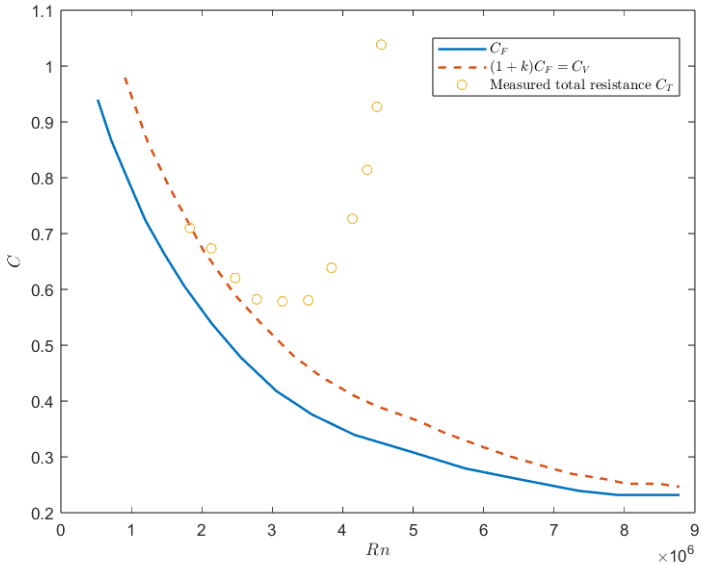

Figure 2.3: Form factor in low speed. [Larsson, L. et al. (2010)]

Prohaska method is the third approach of defining form factor and is considered as the most common one. The main idea about Prohaska method is the expression of C_W with asymptotic expansion representation, which was first introduced in [Toki N. (2008)] and is presented in Equation 2.16 [[Korkmaz K.B. et al. (2020)], Eq. (3)] and afterwards the expression of C_{TM} in Equation 2.17 is introduced in conjunction with the asymptotic [[Korkmaz K.B. et al. (2020)], Eq. (4)].

$$C_W = a \times Fn^4 + b \times Fn^8 + c \times Fn^{12} + d \times Fn^{16} \tag{2.16}$$

$$C_{TM} = (1 + k) \times C_F + a \times Fn^4 + b \times Fn^8 + c \times Fn^{12} + d \times Fn^{16} \tag{2.17}$$

Eliminating the higher order terms, since they are almost equal to zero at low speed numbers and dividing both sides of Equation 2.17 by C_F, the linear expression of Equation 2.18 is derived [[Korkmaz K.B. et al. (2020)], Eq. (5)].

$$C_{TM}/C_F = (1 + k) + a \times Fn^4/C_F \tag{2.18}$$

Significant improvements have been achieved in model-ship correlation in favour of the application of Prohaska method. The report published by Prohaska refers that extracting the results of 200 model runs is observed that the ratio C_T/C_F for the higher percentage of the models tend to be plotted on straight lines for a range of $0.1 < Fn < 0.2$, as it is observable in Figure 2.4 [Prohaska C. W. (1966)] . According to the graph of this figure, the form factor is defined by the intersection of the straight line formed by the measured points and the y axis.

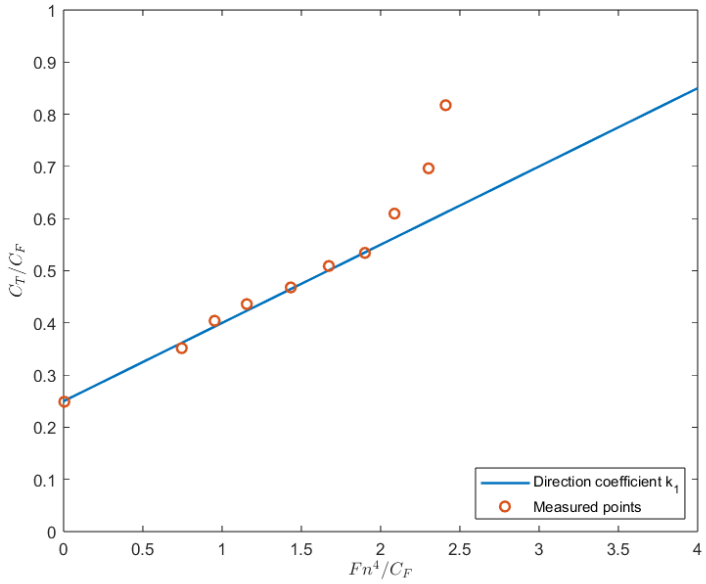

Figure 2.4: Prohaska method. [Larsson, L. et al. (2010)]

Given the fact that Prohaska method was developed before 1966, the method has basic shortcomings. These shortcomings are related to the existence of bulbous bow, in case of twin-screw models with appendages or models with full stern body lines. In these three circumstances, the measured values of ratio C_T/C_F deviate from the aforementioned straight line, making Prohaska method controversial. For this certain reason, the CFD-based approaching for the estimation of form factor is considered necessary and inevitable, specifically when modern hull designs are investigated with partly submerged bublous bow in partial loaded conditions or deeply submerged transoms.

2.2.3.2 CFD-Based Determination of Form Factor

The second way to determine the form factor is the CFD-based approach, which tries to confront the drawbacks and shortcomings of Hughes [Hughes G. (1954)] and Prohaska [Prohaska C. W. (1966)] methods. According to the CFD-based approach, it follows the assumptions of Hughes and is calculated via the Equation 2.19.

$$(1+k) = \frac{C_F + C_{PV}}{C_{FM}} = \frac{C_V}{C_{FM}} \tag{2.19}$$

By using the double-body CFD simulation (Section 2.3.3) for deriving the C_F and C_{PV}. On the other hand, the C_{FM} corresponds to the equivalent flat plate resistance in 2D flow and it is estimated based on the same Re as the computations. It is mentioned that via the same friction line, the C_{FM} in Equation 2.19 and the C_{FS} in Equation 2.3 are obtained, when the CFD-based form factor determination is used [Korkmaz K.B. et al. (2022)].

The disadvantages and weaknesses of Prohaska method, which are presented in Section 2.2.3.1, also concern the CFD-based form factor methodology in a similar manner, in cases such as hull shapes with large bulbous bows and deeply immersed transoms and it can lead to its either under-estimation or over-estimation. Furthermore, another case where the CFD-wise approach is considered inadequate is when a large bulb is in the proximity of the free surface of still water [Korkmaz K.B. et al. (2022)], which corresponds to the mirror plane of the double body simulations, and there is possibility for flow to be separated in the region of bulb, since high level of acceleration takes place. A possible solution to this problem could be the trimming of the hull bow down [Raven, H., C., A. et al. (2008)] in order for all the entire bulbous bow to be submerged. The same practise can be applied for the case of large immersed transom which leads the flow to be separated in the region of wake.

For the aforementioned reasons, an alternative approach of defining the form factor is necessary. As it was referred previously, the two form factor method can be applied efficiently in cases where the preconditions of Hughes and Prohaska methods are not satisfied [Korkmaz K.B. et al. (2022)]. Because of the persistent recirculating flow in the area of transom through the model scale to full scale Re numbers, the full scale viscous resistance is under-predicted, leading to the decomposition of the viscous resistance coefficient to the frictional resistance of a friction line and the flow in the wake of transom. More thorough description of the 2-k method is presented in Section 3.2.

2.3 Numerical Modelling

The main scope of the present thesis is the modelling of numerical simulations for the determination of form factor based on a specific methodology (2-k method). In this section the theoretical background behind the implemented CFD simulations is introduced. The flow around the ship is modelled using single phase flow of water, since the free surface of water is not included in the problem, because the viscous resistance is the only contributor for the estimation of form factor and no the wave-making resistance. Inclusion of turbulence in the flow takes place in order turbulent phenomena to be captured.The best practise would be the use of Direct Numerical Simulation (DNS), because it would be possible to simulate the turbulence the smallest scales in the flow, which are called Kolmogorov scales [Larsson, L. et al. (2010)]. However, in case of using DNS, an extensive computational power is required and it is considered impossible to be used based on the availability in the current practical applications. The most widely used approach is the solution of RANS equations using a closure model, which is presented in the following subsection.

2.3.1 Governing Equations

This subsection refers to the governing equations which constitute the numerical problem behind the executed simulations of this thesis. The governing equations correspond to the RANS equations, which are a time-averaged solution to the Navier-Stokes equations. First of all, the assumption of incompressible flow is made, as the water phase is liquid and the velocity of the flow is much lower that the speed of sound. Moreover, Cartesian tensors are used in order the Navier-Stokes and continuity equations to be more compact. That means that vector components are represented by one index and tensor components by two. Also, the equations are made more compact due to the Einstein's summation, which indicates that if an index is repeated in a term, summation from 1 to 3 shall be made according to this index. Therefore, the continuity equation (Equation 2.20) [[Larsson, L. et al. (2010)], Eq. (9.39)] and the Reynolds-averaged Navier-Stokes equation for an icompressible Newtonian fluid takes the following form of the Equation 2.21 [[Larsson, L. et al. (2010)], Eq. (9.38)].

$$\frac{\partial u_i}{\partial x_i} = 0 \tag{2.20}$$

$$\frac{\partial u_i}{\partial t} + u_j \frac{\partial u_i}{\partial x_j} = -\frac{1}{\rho}\frac{\partial p}{\partial x_i} + F_i + v\frac{\partial^2 u_i}{\partial x_j \partial x_j} \tag{2.21}$$

where u_i represents the velocity components, x_i is the three coordinate components.

To derive the final expression for the viscous term in the derivation of the Navier-Stokes equations, the proportionality between the viscous stresses σ_{ij} and the rate of strain tensor S_{ij} is taken into account (Equation 2.22) [[Larsson, L. et al. (2010)], Eq. (9.40)],

$$\sigma_{ij} = \mu S_{ij} \tag{2.22}$$

where μ is the dynamic viscosity and $S_{ij} = \frac{u_i}{x_j} + \frac{u_j}{x_i}$ [[Larsson, L. et al. (2010)], Eq. (9.41)].

Generally, it is known that four independent equations with ten unknown variables are extracted from the RANS equations in three spatial dimensions and a mass continuity equation. The problem is considered practically impossible to be solved, since imbalance between equations and unknown variables exist, which is called the closure problem of turbulence, while the Reynolds stresses ($\rho\overline{u_j' u_i'}$) give a higher level of difficulty to the problem. Consequently, the Reynolds stresses are modelled using a linear eddy viscosity model, which is presented in Equation 2.23 [[Mikkelsen H.,L. et al. (2019)], Eq. (2.16)].

$$-\rho\overline{u_j' u_i'} = 2\mu_t S_{ij} - \frac{2}{3}\rho k_e \delta_{ij} \tag{2.23}$$

where μ_t is the turbulent or eddy viscosity, k_e is the the turbulent kinetic energy and δ_{ij} is the Kronecker's delta. A two-equation model must be used in order the turbulent viscosity to be predicted. The two-equation models applied for the execution of the simulations in this thesis are introduced in Section 2.3.2.

2.3.2 Two-Equation Models

In the present thesis, two two-equation models are applied for the inclusion of turbulence in the simulations. These models are the realizable $k-\epsilon$ and the shear stress transport (SST) $k-\omega$ model.

Firstly, the realizable $k-\epsilon$ model is a two-equations model, one of which corresponds to the turbulence kinetic energy k and the dissipation rate ϵ. This model is closely related to the mechanisms [Versteeg H. K. et al. (2007)], which have impact to the turbulent kinetic energy. According to this turbulent model, the k and ϵ are used to estimate the velocity scale θ and the length scale l, which represent the large-scale turbulence in Equation 2.24.

$$\theta = k_e^{1/2} \qquad\qquad l = \frac{k_e^{1/2}}{\epsilon} \tag{2.24}$$

The reason why the small eddy variable ϵ is used to determine the large eddy scale l is because the rate of of energy transmission across the energy spectrum to eddies of small magnitude tends to be equal to the rate at which large eddies produce energy for the mean flow at high Re numbers [Versteeg H. K. et al. (2007)]. Via dimensional analysis, the eddy viscosity is given by Equation 2.25.

$$\mu_t = C\rho\theta l = \rho C_\mu \frac{k_e^2}{\epsilon} \tag{2.25}$$

where C_μ is a non-dimensional constant.

Due to the fact that the dissipation rate of turbulence kinetic energy is not the only length scale variable, numerous other two-equation models have been developed, such as the $k-\omega$ model. A revised version of $k-\omega$ model is the $k-\omega$ SST model, which combines the $k-\epsilon$ and $k-\omega$ model and it is also applied in the set-up of simulations of this thesis. In the case of $k-\omega$ model, the specific turbulence dissipation rate or also known as turbulence frequency ω and the length scale is expressed by $l = \sqrt{k_e}/\omega$ and the eddy viscosity is calculated by the Equation 2.26 [[Versteeg H. K. et al. (2007)], Eq. (3.71)].

$$\mu_t = \rho k_e/\omega \tag{2.26}$$

More details on both turbulent models can be found in [[Versteeg H. K. et al. (2007)], Sec. 3.7].

2.3.3 Double-Body Flow RANS computations

It is known that the development of a numerical method, which is accurate and efficient to compute the forces and moments around the hull, is considered the most crucial part in the domain of ship hydrodynamics. Moreover, the numerical method through the solution of RANS equations is the most widely used the last decades for the aforementioned computations. Nevertheless, the application of a RANS tool constitutes an extremely low-efficiency way, especially for applications when the ship motions in six degrees of freedom and the water free surface are taken into consideration. Therefore, it is essential to introduce specific assumptions in order the computational cost and time to be adequately reduced.

One of the mentioned assumptions, which is applied in the setup of the simulations in this thesis, is the *Double-Body Flow* (DB) assumption. According to that, the free-surface effects are considered negligible, because the wave-making resistance does not contribute as a component to the total resistance in case of CFD-based form factor calculations, since the ship speed is quite low and,

consequently, does not stimulate dynamic fluid-body interaction. Practically, the DB assumption is applied by mirroring the hull geometry on top for avoiding including the free surface during the CFD computations, but introducing only the underwater effect in the calculations, as the Figure 2.5 depicts. Recent research work [Yao J. X. et al. (2021)] verifies that the suitability and efficiency of the DB assumption in CFD simulations is due to the low range of values of the Fn number ($Fn < 0.142$), as well as the final predicted results approximate sufficiently the experimental data. From the point of view of the average computational cost, the DB assumption is obviously much less than alternative approaches, such as the water-air flow assumption.

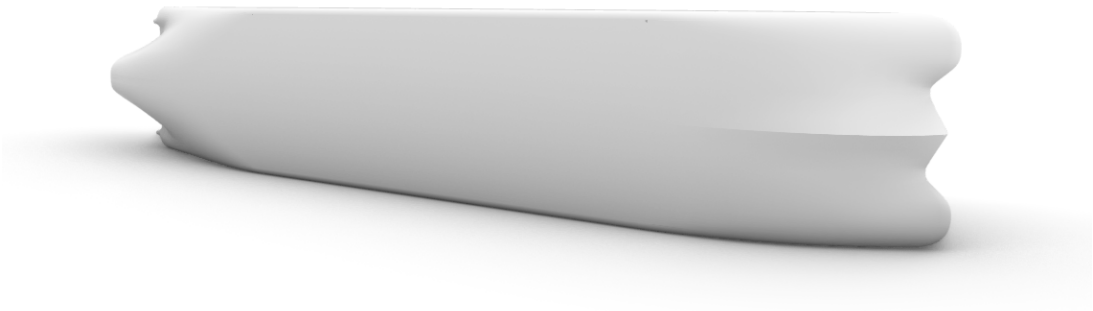

Figure 2.5: Visualization of Double-Body Flow assumption.

From a mathematical perspective, DB assumption is based on the potential flow theory and constitutes a method to linearize the steady potential flow. Specifically, the flow tends to be steady along the hull geometry. Thus, the coupling effects of steady flow are presented by the spatial derivatives of DB potential [Lee J. et al. (2020)]. The main advantage of the DB linearization is that the second-order derivatives are neglected in the body boundary condition (BC). The mathematical expression of the basic DB assumption is given by Equation 2.27 [[Lee J. et al. (2020)], Eq. 5],

$$\phi(\overrightarrow{x}, t) = \Phi + \phi_I + \phi_d \quad (\Phi \gg \phi_I, \phi_d) \tag{2.27}$$

where Φ indicates the steady potential, while the subscripts I and d denote the incident and disturbed waves, respectively. In the context of this thesis, where the CFD-based form factor is investigated, the potential components of incident and disturbed waves are neglected, since there are no wave-induced effects in the numerical computations. Even though the incident and disturbed waves are negligible the Φ term (steady potential) does not contribute to the total resistance, according to the potential flow theory.

2.3.4 Free-Surface Model - Dynamic Fluid Body Interaction (DFBI)

The free surface is designated as the still water surface between the water and the air. The free surface computations are of a crucial importance, since the generated waves are contributors in the total resistance of ship, mainly for high Fn numbers. In the context of this thesis, free surface simulations are applied in order for the flow in the wake of the submerged transom to be studied and how much impact the wetted transom could have in the estimation of form factor. Thus, generated waves are not expected, as long as the Fn number has been chosen equal to 0.1 in both full and model scale, which is considered rather low value.

The Volume of Fluid (VoF) method constitutes the tool for the modelling of the free surface. It is a numerical method of free surface approximation. According to this method, the fraction of water and air is computed in the cells in which both fluids exist. Therefore, based on the volume fraction, a weighted average of their density and viscosity is applied. The interface located in cells with volume fractions of air and water larger than 50% represents the free surface. A continuous fractional function C is applied, which is defined as an integral of fluid functions. Its formula is given in Equation 2.28

$$\frac{\partial C}{\partial t} + v \cdot \nabla C + \nabla \cdot [C(1-C)U_r] = 0 \tag{2.28}$$

where v is the fluid velocity, U_r represents an "imaginary" force which "compresses" the studied region. C takes values between the range $0 < C < 1$ and if the cell is empty without fluid, $C = 0$, while in case of being full, $C = 1$.

The fluid-ship interaction is considered as decisive factor for the assessment of resistance. Through the aforementioned interaction, heave and pitch are generated and they are the two fundamental Degrees of Freedom (DoF) of a vessel in still water. It is known that the ship speed has impact on pitch and heave motions, as well as the vessel performs a certain pitch and heave in a specific speed via equilibrium between static and hydrodynamic forces acting on ship. Thus, the equilibrium pitch and heave represent the dynamic pitch and heave.

As far as the dynamic fluid-body interaction (DFBI) method is concerned, it is used to simulate the fluid-body interaction in STAR-CCM+ [STAR-CCM+ (2023)] software. The forces and moments on the vessel are estimated for specific intervals, as well as the ship is induced on a certain number of translations and rotations until its equilibrium to occur.

2.3.5 Spatial Discretization

The computational domain is considered as the spatial field where the CFD simulations take place. The domain is descritized in a specific number of cells, while each cell is composed of a certain number of faces and nodes depending on the type of mesh (structured or unstructured). The part of the domain apart from the region of boundary layer is called volume mesh. The surface of the investigated geometries, which are the benchmark hulls (Section 3.1.1) in this thesis, are also descritized via segmentation into quadrilateral cells. The group of the triangular surfaces is called surface mesh.

Given that the frictional resistance in the form factor simulations is the main contributor of the total resistance, the modelling of the boundary layer has crucial importance. As it is already mentioned above, in both experimental and computational estimation of form factor the Fn number is kept in a low value in order for the highest percentage of total resistance to be dedicated to skin friction. The non-dimensional quantity that is important when the boundary layer is taken into account is the the wall y^+ value. The y^+ expresses the distance of the center of the first cell to the wall and is given by Equation 2.29.

$$y^+ = \frac{u_* y}{\nu} \qquad\qquad u_* = \sqrt{\frac{\tau_w}{\rho}} \tag{2.29}$$

where u_* is the frictional velocity, y is the distance to the wall and τ_w is the wall shear stress. Depending on which part of boundary layer is studied the y^+ takes a certain range of values (viscous sub-layer $\Rightarrow y^+ < 5$, buffer layer $\Rightarrow 5 < y^+ < 30$ and log-law layer $\Rightarrow 30 < y^+ < 200 - 300$)

[Versteeg H. K. et al. (2007)].

In Figure 2.6, the configuration of the computational grid near to the wall of a surface is illustrated. A boundary layer mesh is used for the discretization of the boundary layer region. Moreover, the boundary layer mesh is composed of multiple layers of thin quadrilateral cells, which are also known as prism layers. The size transition of one layer to a neighboring one must be as much smooth as possible and especially in the region where the boundary layer mesh is connected with the volume mesh.

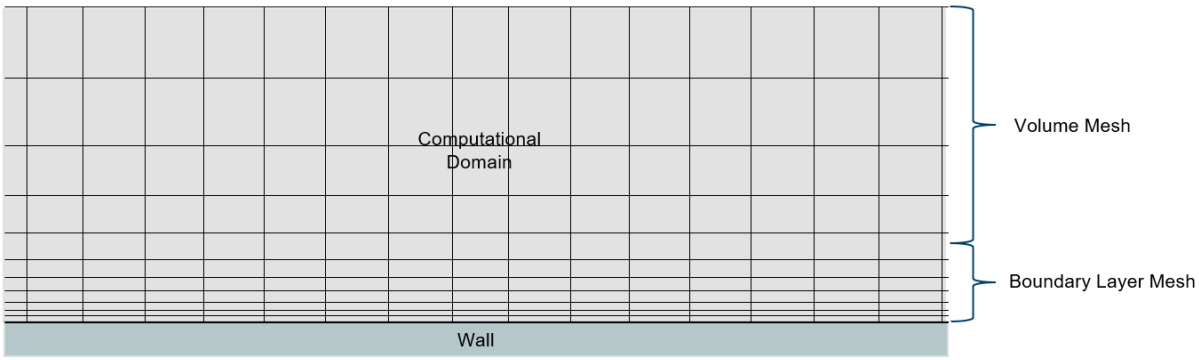

Figure 2.6: Boundary layer and volume mesh.

The flow inside the boundary layer can be modelled with two main approaches. The first approach is about the full resolution of the flow inside the boundary layer with an appropriate number of cells. To be achieved, the y^+ value must be kept below 1 and so the boundary layer flow can be captured all the way down to the viscous sub-layer. However, that means the computational cost of the simulation rises due to the increased number of cells. According to the second approach, wall functions are used for the approximation of the wall shear stress. In that case, the centroid of the first cell next to the wall is positioned in the logarithmic layer ($y^+ > 30$) and therefore there is no cell in the viscous sub-layer. For the set-up of the simulations of this thesis, the wall function "*All-y+ wall treatment*" is used. This wall function integrates the high y^+ values for coarse grids and the low y^+ values for fine grids.

3
Method

This chapter present the methods used in this thesis. The work of the thesis focuses on the CFD-based form factor estimation of three benchmark hulls, implementing in parallel a sensitivity analysis of two different turbulence models and several levels of grid refinement. To obtain a better insight and assessment of the extracted results, data from existing vessels are included in the present study.

First of all, the test cases of both the benchmark hulls and the data from existing vessels are introduced in Section 3.1. Secondly, in Section 3.2 the idea behind two form factor (2-k) method is presented. The concept of the double body RANS computations, which is used in the setup process of the simulations, is described in Section 2.3.3. Afterwards, thorough presentation of the setup of the CFD simulations is extensively presented in Section 3.3. Finally, the verification and validation methods used for the evaluation of the results are expounded in Section 3.4.

3.1 Test Cases

This section presents the ship hulls investigated in this thesis. Five benchmark hulls (JBC, KCS, KVLCC2, DTMB5415 and ONRT) are used for the execution of the systematic analysis of form factor. To have a more holistic study and obtain insight about the present investigation, data from existing vessels are included and also presented in this section.

3.1.1 Benchmark Hulls

The investigated benchmark hulls are provided as 3D geometries by the *Tokyo 2015 Workshop on CFD in Ship Hydrodynamics* and the *Gothenburg 2010 Workshop on Numerical Ship Hydrodynamics*, while their geometries are available as open source material [JBC, Tokyo (2015), KCS, Tokyo (2015), KVLCC2, Tokyo (2015), DTMB 5415, Gothenburg (2010), ONRT, Tokyo (2015)]. The geometries of the aforementioned benchmark hulls are depicted in Figure 3.1 in side view. Moreover, their main particulars in full scale are presented in Tables 3.1, 3.2 and 3.3, while a brief description for each benchmark hull is presented in the next paragraphs.

Specifically, Japan Bulk Carrier (JBC) is a cape-size bulk carrier. The aim of its design was the validation of the results of ship with Energy Saving Device (ESD) from CFD analysis. An ESD is an added device attached onto the hull or propeller of the vessel, such as duct, pre-swirl fins, fin on hull or other modifications in order to increase the efficiency. The reason for the selection of a bulk carrier was the extensive number of this type of vessel in the shipping sector, while a blunt ship is suitable for investigation of the impact of ESDs. The hull of JBC was designed in the context of a cooperative research project organized by shipyards and academic institution in Japan [Hino T. et al. (2020)].

Table 3.1: Main particulars of JBC (Full Scale - Full Load Condition).

Main Particulars	Symbol	Value	Unit
Length Between Perpendiculars	L_{PP}	280	m
Length of Waterline	L_{WL}	285	m
Depth	D	45	m
Maximum Beam of Waterline	B_{WL}	25	m
Draft (Ballast)	T	16.5	m
Block Coefficient	C_B	0.858	-
Scale Factor	λ	40	-

The second studied benchmark hull is KCS. The KCS hull was also used in Tokyo 2015 Workshop and it represents a 3600 TEU (i.e. Twenty-foot equivalent unit) containership, which was also designed for validation purposes of CFD estimations. The mentioned hull was used in Gothenburg 2010 Workshop on CFD in ship hydrodynamics [Larsson L. et al. (2013)]. The model scaling factor for KCS is 1/37.89, while the C_B has low value [Hino T. et al. (2020)].

Table 3.2: Main particulars of KCS (Full Scale).

Main Particulars	Symbol	Value	Unit
Length Between Perpendiculars	L_{PP}	230	m
Length of Waterline	L_{WL}	232.5	m
Depth	D	19	m
Maximum Beam of Waterline	B_{WL}	32.2	m
Draft	T	10.8	m
Block Coefficient	C_B	0.6505	-
Scale Factor	λ	37.89	-

Furthermore, the KVLCC2 model hull was designed in the Korea Research Institute for Ships and Ocean Engineering in 1997. Again, the reason for the design of KVLCC2 was the inclusion of one more test case for validation of CFD estimations. It is mentioned that the KVLCC2 hull used in this thesis is the prototype one, since its stern contour was modified at the CFD Tokyo Workshop in 2005 and this modification is explained in [Hino T. et al. (2020)].

Table 3.3: Main particulars of KVLCC2 (Full Scale).

Main Particulars	Symbol	Value	Unit
Length Between Perpendiculars	L_{PP}	320	m
Length of Waterline	L_{WL}	325.5	m
Depth	D	30.0	m
Maximum Beam of Waterline	B_{WL}	58	m
Draft	T	20.8	m
Block Coefficient	C_B	0.8098	-
Scale Factor	λ	45.714	-

Moreover, the US Navy Combatant (DTMB 5415) was introduced as a preliminary design for a Navy surface combatant in 1980. The hull is composed of both a sonar dome and transom stern.

Also, this benchmark hull includes twin open-water propellers driven by shafts supported by struts [DTMB 5415, Gothenburg (2010)].

Table 3.4: Main particulars of DTMB 5415 (Full Scale).

Main Particulars	Symbol	Value	Unit
Length Between Perpendiculars	L_{PP}	142	m
Length of Waterline	L_{WL}	142.18	m
Maximum Beam of Waterline	B_{WL}	19.06	m
Draft	T	6.15	m
Block Coefficient	C_B	0.507	-
Scale Factor	λ	24.83	-

Finally, the ONR Tumblehome Ship model 5613 constitutes a preliminary design of a state-of-the-art surface combatant. It is published and accessible for implementation of research. The model version of this benchmark hull is appended with bilge keels and skeg, which have been removed for the estimation of form factor, since the bare hull forms are only included in this thesis. Moreover, the hull a hull design which can be considered as wave piercing (i.e. hull with a very fine bow and reduced buoyancy in the fore part), as well as 10^o tumblehome sides and transom stern. Last but not least, the available model includes also rudders, propellers, shafts and superstructure [ONRT, Tokyo (2015)].

Table 3.5: Main particulars of ONRT (Full Scale).

Main Particulars	Symbol	Value	Unit
Length Between Perpendiculars	L_{PP}	154	m
Length of Waterline	L_{WL}	154	m
Maximum Beam of Waterline	B_{WL}	18.78	m
Depth	D	14.5	m
Draft	T	5.494	m
Block Coefficient	C_B	0.535	-
Scale Factor	λ	48.94	-

3.1.2 Other Vessels - Main Parameters

In order to derive more insight about the impact of scale effects and grid refinement in the estimation of form factor, two more hulls are investigated. These referred hulls correspond to two existing vessels for which the 3D CAD geometry, as well as data from sea trials are provided from the database of FORCE Technology. These two hulls represent two bulk carriers of 180K and 82K DWT, respectively. The main particulars in full scale and the used scale factor for each of them in order to be scaled down in model scale are presented in Table 3.6 and Table 3.7.

(a) JBC

(b) KCS

(c) KVLCC2

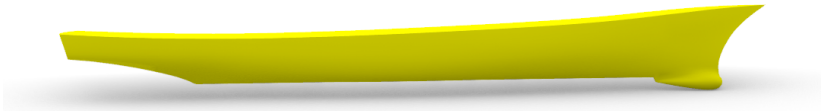

(c) DTMB 5415

(c) ONRT

Figure 3.1: Benchmark hulls (side view).

Table 3.6: Main particulars of 180K Bulk Carrier (Full Scale).

Main Particulars	Symbol	Value	Unit
Length Between Perpendiculars	L_{PP}	283.5	m
Length of Waterline	L_{WL}	288	m
Maximum Beam of Waterline	B_{WL}	45	m
Depth	D	24	m
Draft	T	17	m
Block Coefficient	C_B	0.92	-
Scale Factor	λ	36.818	-

Table 3.7: Main particulars of 82K Bulk Carrier (Full Scale).

Main Particulars	Symbol	Value	Unit
Length Between Perpendiculars	L_{PP}	223	m
Length of Waterline	L_{WL}	227.015	m
Maximum Beam of Waterline	B_{WL}	32.25	m
Depth	D	20.1	m
Draft	T	12.2	m
Block Coefficient	C_B	0.87	-
Scale Factor	λ	29.625	-

3.2 Two Form Factor Method

As it is already discussed in Section 2.2.3, the issue of which is the best practise for the estimation of form factor concerns the field of ship hydrodynamics and towing tanks almost one century. The belief of some researchers that a 2D flow line is not adequate for the extrapolation problem, as it is presented in ITTC (1957) [ITTC (1957)], introduced an alternative approach of a separate extrapolator for each hull form, such as the one proposed by Hughes (1954) [Hughes G. (1954)]. The main problem with Hughes method is the difficulty to stimulate turbulent flow around the hull, since the execution of resistance test must be in very low Re and Fn numbers for the form factor estimation. Also, the measurements can be considered vulnerable to inaccuracy due to forces of low values. For the aforementioned reasons Prohaska (1966) [Prohaska C. W. (1966)] recommended a simplified process to extract the form factor from resistance testing, making specific assumptions (Section 2.2.3). If the assumptions are not satisfied, Prohaska approach tends to fail.

Recirculation of flow in the wake of transom, which is one of the problematic issues of Prohaska method, is constant for all Re numbers from model to full scale. This creates an under-prediction of the R_{VS}. To overcome this problem, decomposition of viscous resistance coefficient in model scale (C_{PVM}), or also known as form resistance, is applied Equation 3.20 [[Korkmaz K.B. et al. (2022)], Eq. (4)].

$$C_{PVM} = C'_{PVM} + C_{trM} \tag{3.1}$$

where C'_{PVM} represents the proportional part to the C_F and C_{trM} indicates the part of resistance produced due to the flow separation in the wake of transom and it is not proportional to C_F. According to *Korkmaz et al.* [Korkmaz K.B. et al. (2022)] C_{trM} does not change from model to full

scale Re number. In Figure 3.2 it is observable that both C'_{PVM} and C_{trM} scale down proportional to the illustrated C_F line given that the same form factor in model and full scale is used. As a conclusion, CFD form factor prediction must be used for its correction or prompt estimation for hulls with a wetted transom.

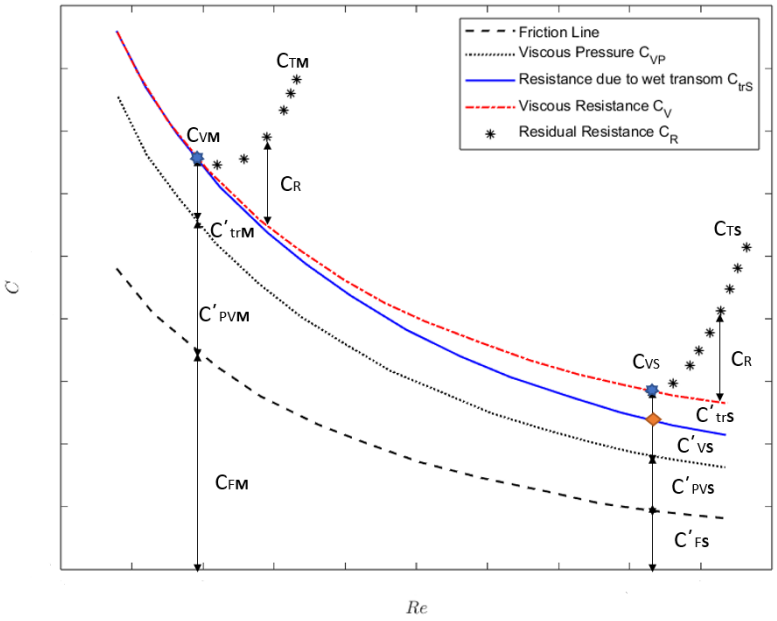

Figure 3.2: Concept of 2-k method. Extracted by [Korkmaz K.B. et al. (2022)]

The aforementioned methodology is called two form factor (2-k) method and certain steps are needed for its application. Firstly, the towing tank testing provide the C_{TM}. Afterwards, using either Prohaska method [Prohaska C. W. (1966)] or CFD simulation [Korkmaz K.B. et al. (2021)], the form factor in model scale k_M is calculated. Then, the residual resistance coefficient is computed by the Equation 3.20. On the other hand, the full scale form factor is estimated by CFD-based form factor method and, finally, the total resistance in full scale is computed by Equation 2.3.

$$C_R = C_{TM} - (1 + k_M)C_{FM} \tag{3.2}$$

The C_R is derived by use of model scale form factor, while C_V is extracted by using the full scale form factor [Korkmaz K.B. et al. (2022)]. In Figure 3.3, the aforementioned process of the 2-k method is presented in the form of a flow chart in order to be more straightforward. It is obvious that the case of a submerged transom is included in the workflow, based on the study of [Korkmaz K.B. et al. (2022)].

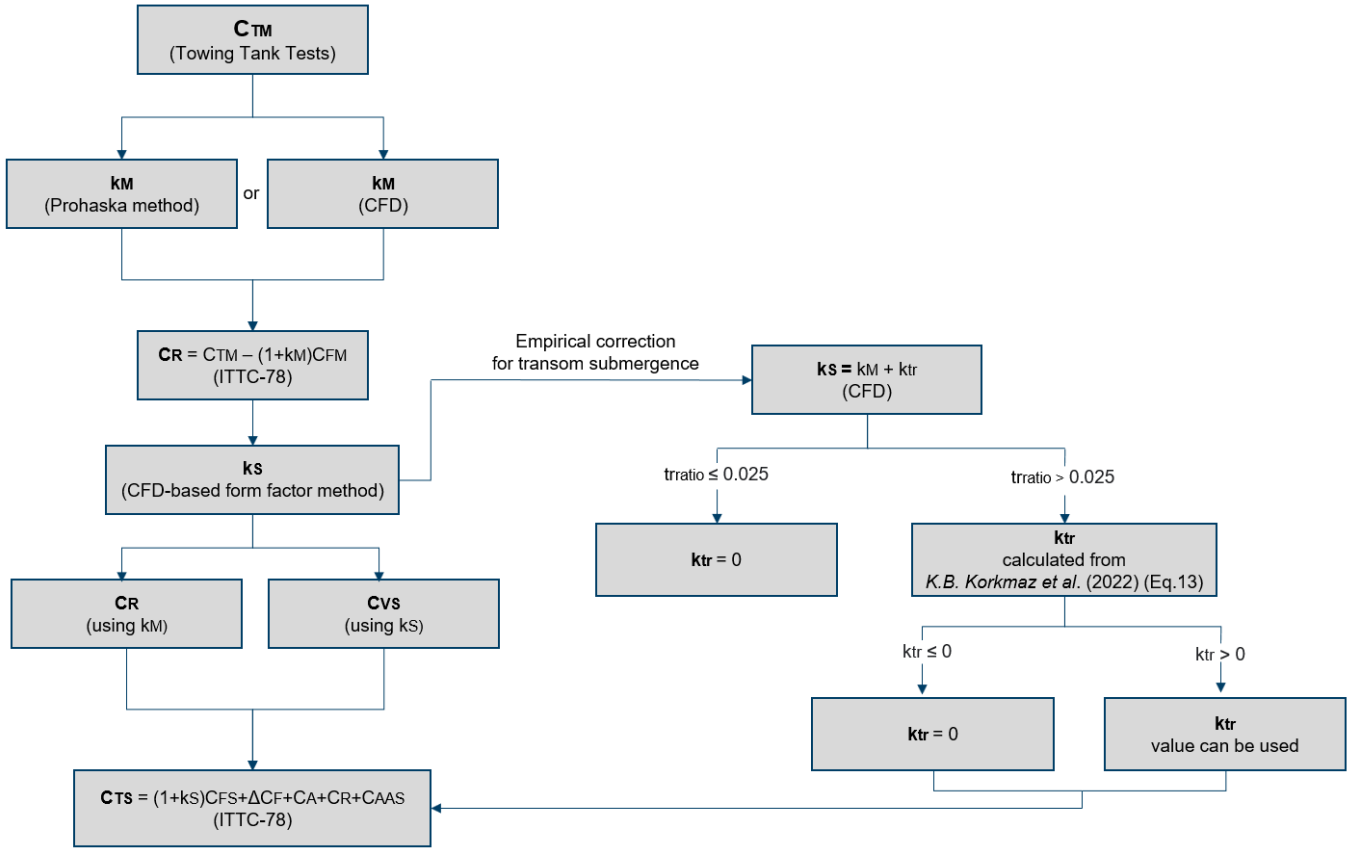

Figure 3.3: Flow chart of 2-k method.

As far as the empirical correction for transom submergence is concerned, the existing recommended processes for the form factor estimation in both model and full scale can be considered as deficient, since flow separation behind the transom is developed. The *2-k* method is used to overcome these kind of issues (i.e. recirculating flow). On the other hand, the *2-k* method has as requirement the application of double-body RANS computations, as well as a Best Practice Guideline (BPG), the BPG's quality assessment and verification of its quality are necessary. Consequently, an empirical correction formula (Equation 3.3) has been established [Korkmaz K.B. et al. (2022)], Eq. 13] via a regression analysis.

$$k_{tr} = [-0.025 + tr_{ratio}(1.5 - 2.3tr_{ratio} - 0.07LCB)] \times [-5.45 + \log_{10}(\bar{Re}_M) \\ (1.415 + 4.32tr_{ratio}) - (\log_{10}(\bar{Re}_M))^2(0.081 + 0.55tr_{ratio})] \tag{3.3}$$

According to regression analysis, it is related to the prediction of k_{tr} from the $k-\omega$ SST model and the numerical friction line. Moreover, the scaling effects included by the friction line are introduced for the extraction the k_{tr} values [Korkmaz K.B. et al. (2022)]. By comparing the the k_{tr} values from CFD and the empirical correction formula, Equation 3.3, the two methods do not present high level of discrepancies, as the results from simulations present in Chapter 4.

To apply the submerged transom correction, three main variables must be determined, the transom Froude number Fr_{tr}, the transom ratio tr_{ratio} and the transom fullness $tr_{fullness}$, which are defined from Equations (3.4a) to (3.4c).

$$Fr_{tr} = \frac{V}{\sqrt{gT_{tr}}} \tag{3.4a}$$

$$tr_{ratio} = \frac{A_{tr}}{A_{max}} \tag{3.4b}$$

$$tr_{fullness} = \frac{A_{tr}}{2y_{tr}T_{tr}} \tag{3.4c}$$

where T_{tr} is the draught of transom, g is the gravitational acceleration, V the flow speed, A_{tr} is the area of the submerged transom, A_{max} is the maximum cross-section area for a given draft and y_{tr} is the transverse dimension of the wetted transom. For a better understanding of these three geometrical variables, one can see the paper [[Korkmaz K.B. et al. (2022)], Fig. 3]. A lower limit in tr_{ratio} is set ($tr_{ratio} \leqslant 0.025$), as long as lower values can lead in partially wetted-transom or dry-transom flow.

3.3 CFD Simulations Setup

At this point the CFD setup of the form factor simulations is described both in model scale and full scale. All CFD simulations are executed in the commercial CFD-code STAR-CCM+ v.17.06.007 from Siemens [STAR-CCM+ (2023)]. The use of the aforementioned software is broad in maritime industry and it is widely known for its capabilities when is applied in the marine sector.

3.3.1 Computational Domain and Boundary Conditions

In the present section, the characteristics of the computational domain are presented. Specifically, the domain is a rectangular parallelepiped with the aim of representing the arrangement of a towing tank. The dimensions of the computational field are selected depending the scale factor of the hull in each case. Its dimensions are depicted in Table 3.8 as a percentage of L_{PP}. In Figure 3.4 the visualization of the computational field is illustrated, as well as the nomenclature of the seven boundaries.

Table 3.8: Domain size of the CFD setup in model and full scale.

Dimension	**Percentage of L_{PP}**
Longitudinal Upstream Length	$2L_{PP}$
Longitudinal Downstream Length	$5L_{PP}$
Vertical Length	$2L_{PP}$
Transverse Length	$3L_{PP}$

The boundary conditions of the domain are presented in Table 3.9. A symmetry plane is used, because the flow is symmetrical in starboard and portside and thus the computational cost of the simulations is reduced to half. Moreover, a refinement zone of grid is applied for capturing the abrupt changes of the flow, such as flow speed and pressure, to be sufficiently captured. The refinement direction in the region near to the geometry is the same for all the three dimensions (longitudinal, transverse, vertical). There is no need for more refinement zones to be added, since the double-body assumption, does not include the interaction of the free-surface with the studied geometry and therefore the wave generation is negligible.

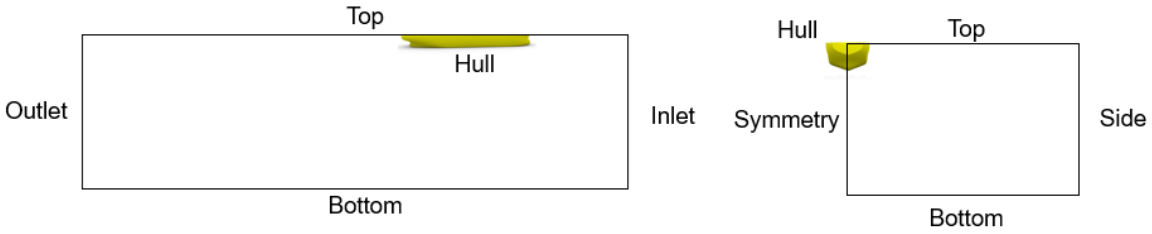

Figure 3.4: Qualitative representation of the arrangement of domain in model and full scale with boundary nomenclature for DB approach. (Left) Starboard side and (Right) Front side

Table 3.9: Boundaries and boundary conditions of the CFD setup in model and full scale.

Boundary	Boundary Condition
Inlet	Velocity inlet, prescribed with V_m
Outlet	Pressure outlet
Top	Symmetry plane
Bottom	No-slip wall
Symmetry	Symmetry plane
Side	No-slip wall
Hull	No-slip wall

On the other hand, the arrangement of the refinement zones is different when the free surface is taken into account for the application of Prohaska method. As it is illustrated in Figure 3.6, four refinement zones are applied. The selection of the location of refinement zones is decided depending on which regions of the domain are crucial and it is possible that they have impact on the final results.

Table 3.10: Refinement zones of the FS case.

Refinement Zone	Refinement Direction
Bow RZ	All
Transom RZ	All
Free-Surface RZ	Vertical
Wake Kelvin RZ	Longitudinal and Transverse

The purpose of the bow RZ is to resolve Kelvin waves, which are expected to be negligible. The transom RZ plays an important role, since there is tendency for flow separation when the transom is submerged. Furthermore, the bow RZ is needed due to the development of high values of pressure, as well as the stagnation point. Finally, the free-surface RZ tries to capture the surface elevation due to the the presence of the geometry. In Table 3.10, the refinement direction of the refinement zones is depicted.

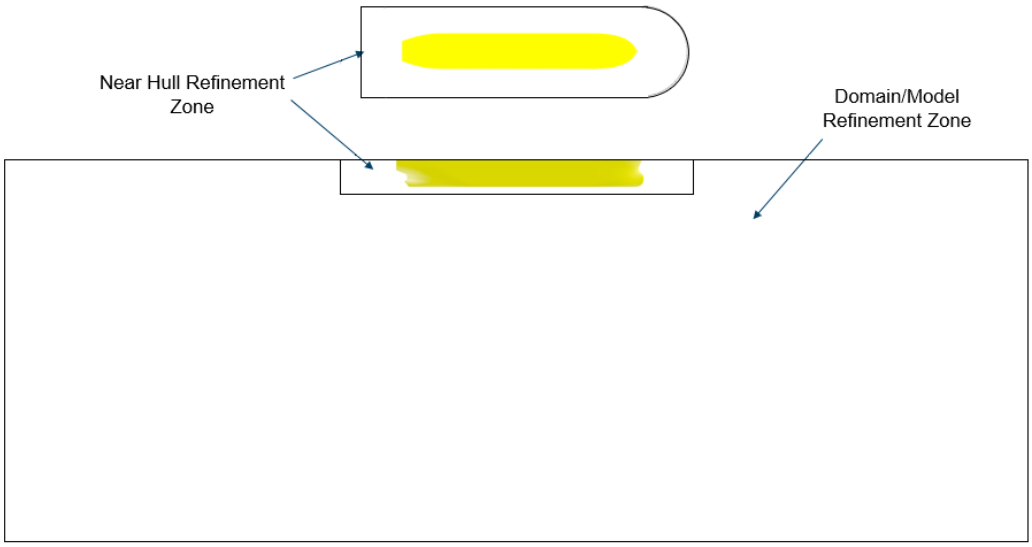

Figure 3.5: Refinement zones in model and full scale for DB approach. Top view (top) and side view (bottom).

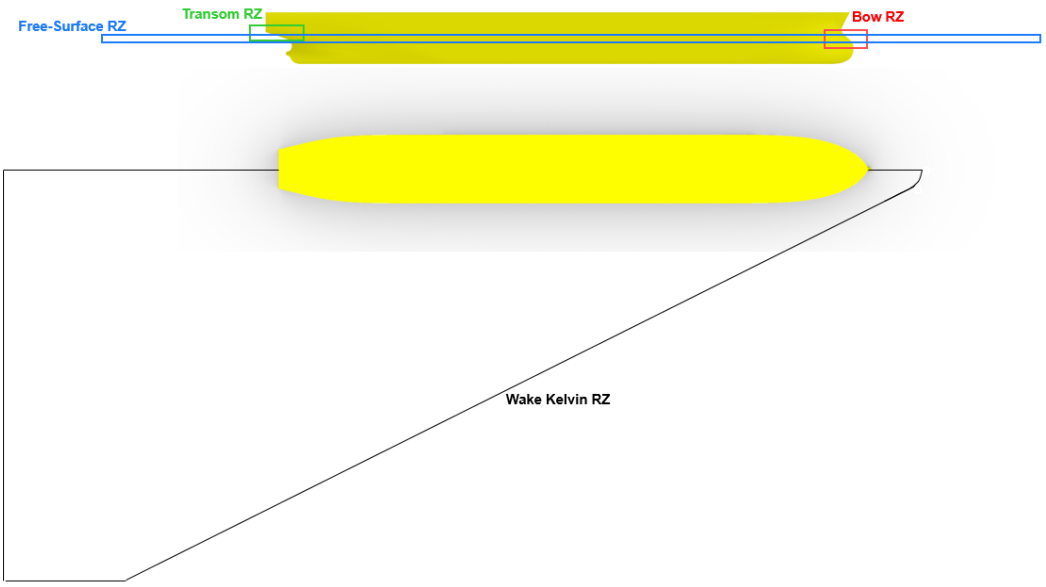

Figure 3.6: Refinement zones in model and full scale for F-S model. Side view (top) and top view (bottom).

3.3.2 Grid Generation

As the most crucial part during the set-up of the simulations, the grid generation is implemented by taking into account some peculiarities of the flow field. These peculiarities are relevant to the viscous and turbulence effects of the flow and the frictional contribution to the total resistance of the studied hulls, since they are the decisive factors in the analysis and scope of this thesis.

In order for both the frictional and turbulent effects to be captured, the creation of prism layering, which represents the boundary layer near to the wall of the hulls, is necessary. As far as the scaling

of the simulation is concerned, i.e. model or full scale and the several scale factors used for the scaling sensitivity study, as it is presented in Appendix A, the characteristics of prism layering, such as number of layers, Equation 3.5, near wall distance etc., change in a way to be as much effectively adaptive in the boundary layer as possible.

Both the prism layering thickness and the near wall distance are Re-dependent, since the flow speed closely affects if it is laminar or turbulent. Moreover, the number of the prism layers, Equation 3.5, and the stretching factor are related to the total thickness of the layering and in what extent it contains the turbulence inside the boundary layer. The stretching factor λ_s is defined as the thickness of each cell layer as a ration of the previous layer. The referred characteristics are presented in the Tables A.1 and A.2. The estimation of the boundary layer thickness and the near wall distance are given from the empirical formulas in Equations 3.6 and 3.7, respectively.

$$N = \frac{ln(1-(1-\lambda_s)\frac{\delta}{X})}{ln(\lambda_s)} \tag{3.5}$$

where X is the first cell thickness.

$$\frac{\delta}{x} \cong \frac{0.38}{(Re)^{1/5}} \tag{3.6}$$

where x corresponds to the characteristic length of the studied geometry, i.e. L_{PP}, and δ is the thickness of the boundary layer. The dimension of the first cell normal to the wall is computed by using the Equation 3.7 [[Huang et al. (2023)], Eq. 10].

$$y^+ = \frac{t_0}{L_{PP}} \times Re\sqrt{0.00375/(log(Re)-2)^2} \tag{3.7}$$

where t_0 is the wall distance of the first cell near to wall.

Due to the fact that there is need of capturing the boundary layer in full scale in such a way in order the turbulent phenomena into it to be included, a high value of y^+ must be applied. In opposite case, following the model-scale standard regarding the value of y^+ to set-up full scale simulations can be considered as waste of computational resources [Huang et al. (2023)]. In Figure 3.7, an indicative representation of the refinement of mesh in the vicinity of wall is presented, in which the stretching rate is visible. Moreover, the configuration of the generated mesh for the numerical simulations for both DB and F-S methods is illustrated in Figure 3.8. The depiction of the mesh in stern and bow presents the refinement zones, as well as the inclusion of the prism layering.

$$T_H = \sum c_i = \frac{\lambda_s^N - 1}{\lambda_s - 1} \cdot t_0 \tag{3.8}$$

where T_H is the total thickness of boundary layer in m, λ_s is the stretching factor and N is the number of layers.

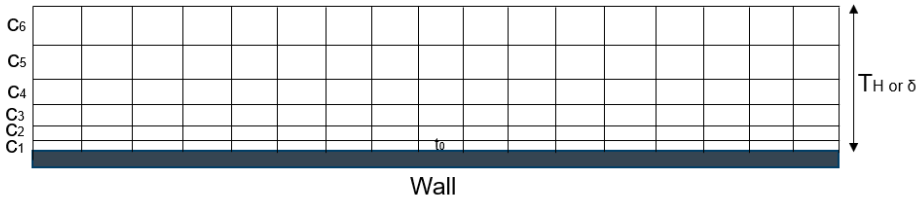

Figure 3.7: Graphical representation of the parameters of boundary layer.

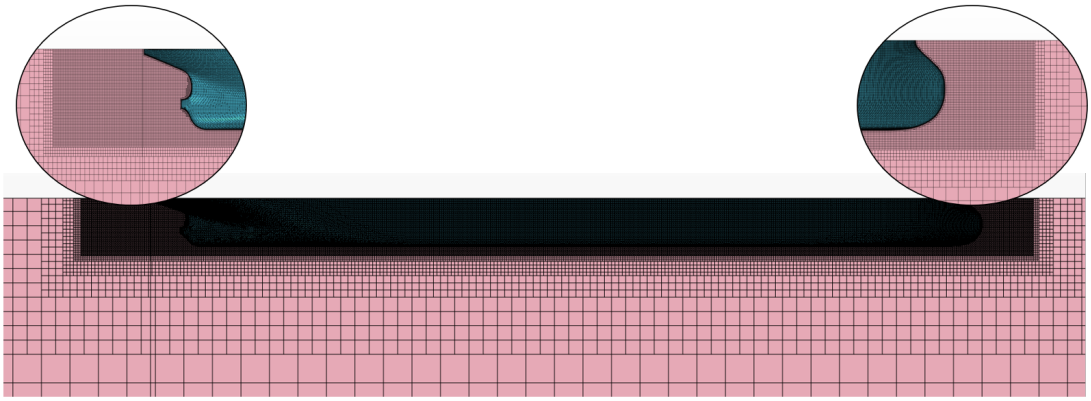

(a) DB model

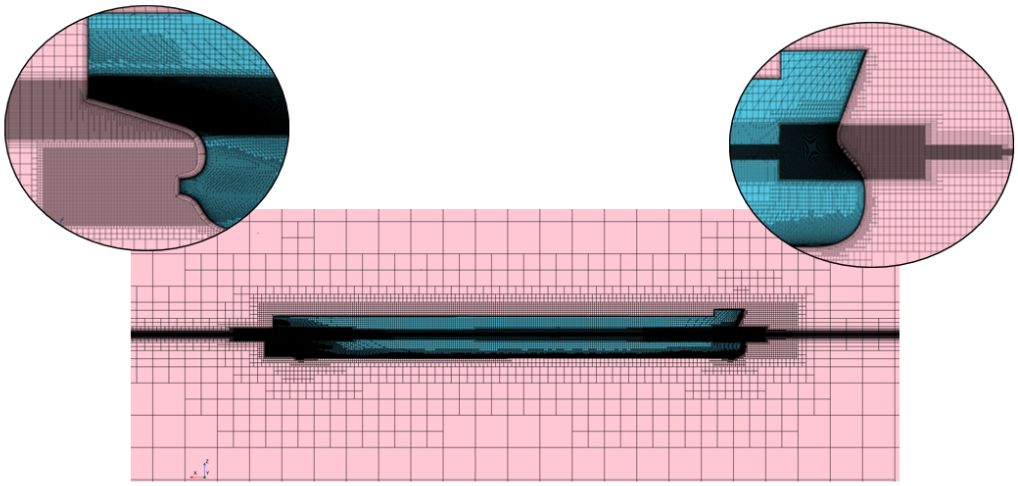

(b) F-S model

Figure 3.8: Representation of generated mesh with details at the bow and stern for both DB and F-S numerical computations (side view - JBC).

Finally, in Figure 3.9, the y^+ distribution is depicted for both MS and FS. The values of y^+ are kept in an accepted range [Mikkelsen, H. et al. (2020)] in order the turbulence phenomena in the aft part of the hulls to be captured, especially for FS simulations, which they are expected more intensive. One can observe that discrepancy in y^+ distribution is observed in the aft and fore part of the three test cases, because the geometry changes abruptly in these parts of the hulls.

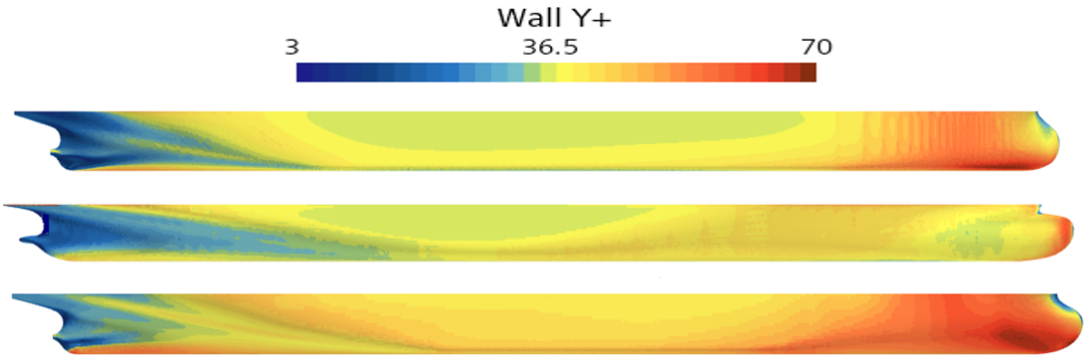

(a) MS

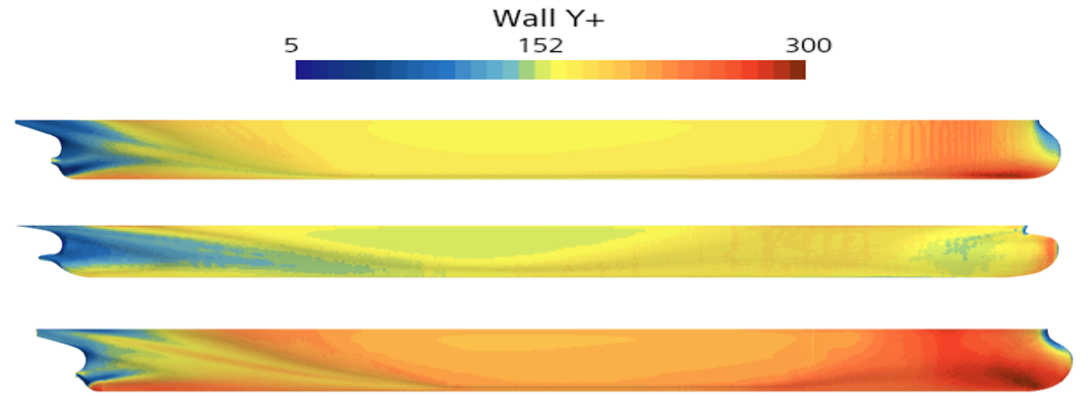

(b) FS

Figure 3.9: Distribution of y^+ for the benchmark hulls JBC (top), KCS (middle) and KVLCC2 (bottom) (side view).

3.3.3 Hull Roughness Modelling

Two separated approaches are used for estimation of hull roughness in full scale. The first approach is referred to the estimation of roughness resistance using empirical formulas by applying it as a point force in the centre of gravity of hull. The most recent published empirical formula is the one of [Towsin & Mosaad (1985)], Equation 3.9, which takes into account only the roughness effect.

$$\Delta C_f = 0.0044[(\frac{AHR}{L_{WL}})^{\frac{1}{3}} - 10 \times Re^{-\frac{1}{3}}] + 0.000125 \tag{3.9}$$

where AHR represents the Average Hull Roughness. The recommended roughness height from ITTC [ITTC (Revision 2008) (1978)] for full scale CFD simulations is given equal to 150 μm, which is used in the present thesis, when the sensitivity of form factor in roughness is investigated and represents the AHR.

Modelling of roughness effects via application of a roughness function and modification of the wall function constitutes a different approach, as it is firstly introduced by [Cebeci and Bradshaw (1977)]. According to this approach, the elements of roughness onto the surface tend to increase the turbulence in the boundary layer. Therefore, an additional function in the formula which describes the mean velocity profile for a smooth surface is needed, as it is presented in Equation 3.10.

$$U^+ = \frac{1}{\kappa} ln y^+ + B - \Delta U^+ \tag{3.10}$$

where ΔU^+ represents the roughness function, U^+ is the normalized velocity in the boundary layer, κ is the von Karman constant equal to 0.42, y^+ is the normalised normal distance to the wall and B is smooth wall log-law intercept. It is mentioned that the roughness function is defined through experiments for a given flow over a rough surface. Furthermore, another way for roughness function to be expressed is as Re-dependent, Equation 3.11

$$R_s^+ = \frac{R_s U_\tau}{\nu} \tag{3.11}$$

where R_s is the equivalent sand-grain roughness height and $U_\tau = \sqrt{\tau_w/\rho}$ is the friction velocity.

As far as the simulations of this thesis are concerned, four different roughness heights for the test cases of JBC, KCS and KVLCC2 have been studied. In that way, a systematic analysis regarding the change of roughness of the hull surfaces can give insights about how much it can affect the estimation of form factor.

3.4 Verification and Validation

It is well known that the numerical modelling extract errors and uncertainties and it is practically impossible for the real problem to be directly solved. Consequently, the credibility of the results, as well as the degree of accuracy must be studied especially in cases of computations of complex turbulent flows. Based on the numerous studies being implemented in the CFD domain, the evaluation of accuracy through comparison of EFD and CFD results cannot be considered reliable. Verification and validation (V&V) methods are applied for the estimation of the numerical and modelling errors. Numerical uncertainty and achieved order of accuracy are assessed via the Least Squares Root (LSR) approach. Finally, the basis of the LSR method is based on the Richardson Extrapolation (RE) and Grid Convergence Index (GCI), which are presented in detail below.

3.4.1 Verification Method

The verification procedure is the assessment of numerical uncertainty in a numerical computation and it is composed of the solution and code verification. The code verification is disregarded, because the code is considered to be properly developed. Thus, the solution verification is the point of interest.

As far as governing equations of ship hydrodynamics are concerned, they present non-linear behavior and high level of complexity. Therefore, the only way of solving them is via iterative procedures. However, existence of errors is unavoidable, especially when the studied geometry is complex, such as a hull shape, and the flow cannot be well attached onto it (i.e. flow separation). Furthermore, the discretization of the domain can produce errors without round-off error included. Equation 3.12 gives the numerical uncertainty, taking into account both the discretization and iterative uncertainty.

$$U_{SN} = \sqrt{U_I^2 + U_G^2} \tag{3.12}$$

where U_G is the discretization uncertainty and U_I is the iterative uncertainty, because of difficulty in the convergence of solution. Depending on which uncertainty is the biggest contributor of the numerical uncertainty, the other one can be eliminated.

3.4.1.1 Grid Convergence Index (GCI)

According to the discretization uncertainty, the most common approach is considered the GCI method. Through RE, grid convergence is achieved by a series of systematically similar grids [Korkmaz K.B. et al. (2021)]. The grid refinement ratios are calculated by the Equation 3.13, while in Table 3.11 data of the number of refinements, total number of cells and the grid refinement ratios are presented for the testing case of JBC in model and full scale.

$$h_1/h_i = \sqrt[3]{N_{grid1}/N_{gridi}} \tag{3.13}$$

Table 3.11: Total number of cells and grid refinement ratios.

	Model Scale		Full Scale	
Grid	Number of cells	h_1/h_i	Number of cells	h_1/h_i
g_1	2.01×10^7	1.00	9.93×10^6	1.00
g_2	1.24×10^7	1.18	6.11×10^6	1.18
g_3	7.39×10^6	1.39	3.65×10^6	1.39
g_4	4.52×10^6	1.65	2.24×10^6	1.65
g_5	2.75×10^6	1.94	1.36×10^6	1.94

The GCI procedure starts by calculating the apparent order (p) by Equation 3.14.
[Mikkelsen, H. et al. (2020)]

$$p = \frac{1}{ln(r_{21})}|ln|\epsilon_{32}/\epsilon_{21}| + q(p)| \tag{3.14}$$

where $q(p) = \frac{r_{21}^2 - s}{r_{32}^p - s}$, where q(p)=0 if r = constant, r are the refinement ratios, $\epsilon_{32} = \phi_3 - \phi_2$, $\epsilon_{21} = \phi_2 - \phi_1$ and ϕ_i represents the solution of the i-th grid. In Equation 3.15, the extrapolated asymptotic value is presented.

$$\phi_{ext}^{21} = \frac{r_{21}^p \phi_1 - \phi_2}{r_{21}^p - 1} \tag{3.15}$$

The approximate and extrapolated relative error are given by Equation 3.16 and 3.17, respectively.

$$e_a^{21} = \frac{\phi_1 - \phi_2}{\phi_1} \tag{3.16}$$

$$e_{ext}^{21} = \frac{\phi_{ext}^{12} - \phi_1}{\phi_{ext}^1 2} \tag{3.17}$$

Finally, the GCI is estimated using the formulas of Equation 3.18 and 3.19 for the case of fine and medium mesh.

$$GCI_{fine}^{21} = \frac{1.25 e_a^{21}}{r_{21}^p - 1} \tag{3.18}$$

$$GCI_{medium}^{32} = \frac{1.25 e_a^{21} r_{21}^p}{r_{21}^p - 1} \tag{3.19}$$

3.4.1.2 LSR Approach

The scatter of numerical solutions with a minimum number of grid densities of four ($n_g \geqslant 4$) is taken into account in the context of LSR method. The discretization error ϵ_{RE} in LSR is related to the RE [Korkmaz K.B. et al. (2021)].

$$\epsilon_{RE} = \delta_{RE} = S_i - S_0 = ah_i^p \tag{3.20}$$

S_i represents any integral or other functional of a local flow quantity, S_0 is the exact solution, a is a constant to be defined and h_i is the cell size. To define the unknown parameters (S_0, a, p) at least three solutions are needed. If the grid densities are more, the unknown parameters can be estimated by the LSR method, finding the minimum of the function below (Equation 3.21).

$$f(S_0, a, p) = \sqrt{\sum_{i=1}^{n_g}(S_i - (S_0 + ah_i^p))^2} \tag{3.21}$$

According to the proposed methodology by Eça and Hockstra [Eça L. et al. (2002)], the uncertainty of a solution is closely related to the value of the computed order of accuracy. Equal mesh refinement ratios among medium/finest and coarsest/medium meshes can provide estimation of the grid convergence behavior based on the discrimination ratio R (Equation 3.22). The discrimination ratio R is dependent to the observed order of grid convergence p and the grid refinement ratios h_2/h_1 and h_3/h_2 [Eça L. et al. (2014)].

$$R = (\frac{h_1}{h_2})(\frac{(\frac{h_2}{h_1})^p - 1}{(\frac{h_3}{h_2})^p - 1}) \tag{3.22}$$

The rate of convergence is defined as [Korkmaz K.B. et al. (2021)]:

- Monotonic convergence: $p > 0$
- Not-observable monotonic convergence: $p < 0$
- Oscillatory convergence: $n_{ch} \geqslant INT(N_G/3)$, where n_{ch} indicates the number of triplets with $(S_{i+1} - S_i)(S_i - S_{i-1})$
- Differently, anomalous

Furthermore, based on the order of accuracy, which is relevant to the scatter, three different approaches can express the error, as they are introduced in Equation 3.23, 3.24 and 3.25.

$$\delta_{RE}^{02} = S_i - S_0 = a_{02}h^2 \tag{3.23}$$

$$\delta_{RE}^{12} = S_i - S_0 = a_{11}h + a_{12}h^2 \tag{3.24}$$

$$\delta_{\Delta M} = \frac{\Delta_M}{(h_{ng}/h_1) - 1} \tag{3.25}$$

where Δ_M represents the data range and h_{ng} is the step size of the n_g^{th} grid.

Based on the value of R, the type of convergence or divergence of the solutions can be designated with the following four categories:

- Monotonic convergence when $0 > R > 1$
- Monotonic divergence when $R > 1$
- Oscillatory convergence when $R < 0$ and $|R| < 1$
- Oscillatory divergence when $R < 0$ and $|R| > 1$

3.4.2 Validation Process

The evaluation of uncertainties and errors of a numerical computation is implemented via the validation procedure. The validation method constitutes the assessment of simulation modelling uncertainty (USM) by using benchmark experimental data and estimation of sign and magnitude of the modelling error δ_{SM}. In the validation process, two parameters are included, which are the validation comparison error (Equation 3.26) and the validation uncertainty (Equation 3.27).

$$E = D - S = \delta_D - (\delta_{SM} + \delta_{SN}) \tag{3.26}$$

where E is the comparison error, S is the solution from simulation, D is the solution from experiment, δ_D is the difference between an experimental data and the truth.

$$U_V^2 = U_{SN}^2 + U_D^2 \tag{3.27}$$

where U_D is the data uncertainty from experiments, U_V validation uncertainty.

Finally, after the determination of validation comparison error and the validation uncertainty, the validation result can be defined with two different ways:

- For $|E| > U_{val}$, all the errors in both D and S are greater than U_V and so validation is not achieved for this validation uncertainty level. The magnitude of the validation uncertainty gives the level of confidence in the CFD model.
- For $|E| < U_{val}$, all the errors in both D and S are smaller than U_V and so validation is achieved at the U_V interval [Korkmaz K.B. et al. (2021)]. When $|E| \ll U_{val}$, the δ_{SM} indicates that the simulation needs improvements.

4
Results

This chapter presents the results extracted from the CFD simulations. Specifically, all the sensitivity analyses implemented in the context of the present project are mentioned and commented, as well as the V&V procedure is presented for the JBC and KCS test cases, respectively. Tabular representation and additional visual material of the results are given in the section of Appendices with the aim of more insights.

4.1 Pressure Distribution and Wave Pattern

As it has been mentioned in the previous chapters the investigated test cases are the five benchmark hulls and two commercial ones, referred in subsection 3.1.1 and 3.1.2, respectively. The two computational models which have been tested are the Double-body and Free-Surface models, which are presented in subsection 2.3.3 and 2.3.4. The study of the Free-Surface model is required, since the impact of free fluid surface is critical for the investigation of the recirculation generated behind the transom. On the other hand, the Double-Body model is the computationally most "cheapest" solution for executing simulations like the ones implemented for form factor predictions. This can be considered the main reason why the majority of the implementing simulations use the aforementioned model.

This section presents the hull surface pressure coefficient C_P of the three benchmark hulls of JBC, KCS and KVLCC2. The no-dimensionalisation of the pressure is chosen in order for the comparison of the two computational models to be more apparent. Its normalisation is made through division of the static pressure by the dynamic one, as the Equation 4.1 presents.

$$C_P = \frac{p - p_\infty}{\frac{1}{2} \cdot \rho_\infty \cdot V_\infty^2} \tag{4.1}$$

where p indicates the pressure at a specific point where the C_P is estimated, p_∞ represents the pressure in the freestream, ρ_∞ is the fluid density in the freestream and V_∞ is the freestream fluid velocity.

In Figure 4.1, the pressure distribution onto the surface of the three benchmark hulls is illustrated. One can observe that the depicted contours present differences between the two models in local level. This means that the pressure distribution is similar in both cases, but in some specific parts of the hulls the pressure distribution has visible discrepancies. This can be explained as the two computational models use different mathematical models to estimate the pressure value in each node of the generated computational grid and especially due to the fact that they represent completely different approaches. Generally, the over-pressure and under-pressure regions have been developed in a reliable way and presented compatible formation in both models.

A brief study of the pressure results can be considered necessary, because it helps to the evaluation and comprehension of the field results and the conclusion of whether they are reasonable or not and consequently the form factor estimation can be taken into account as trustworthy or not. Based on the depicted results of Figure 4.1, the level of pressure in each certain part of the hulls is the expected one.

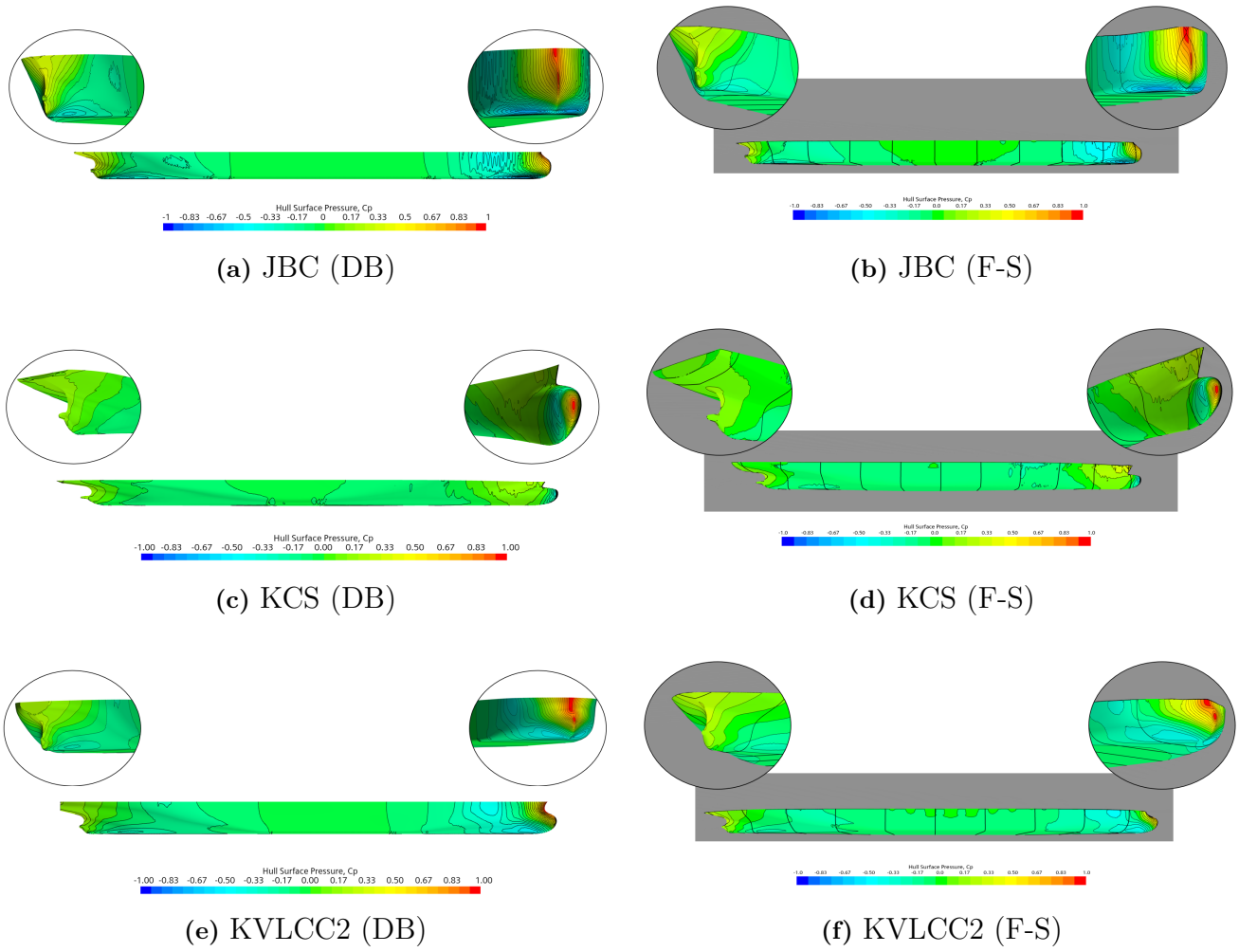

(a) JBC (DB) **(b)** JBC (F-S)

(c) KCS (DB) **(d)** KCS (F-S)

(e) KVLCC2 (DB) **(f)** KVLCC2 (F-S)

Figure 4.1: Pressure distribution around the hull surface of the three benchmark hulls in FS (side view).

In Figure 4.2 the formation of wave pattern for the three benchmark hulls for the case of the scantling draft (the maximum draft at which the ship can withstand all the loads safely) and $Fn = 0.1$ is presented. As it was expected, the free surface elevation is resulted quite low, since the speed of the hulls has low value. As a result, the main contributor of the ship resistance is the frictional one. From the point of view of energy losses, the generated waves are not the decisive factor for attributing the increase of total losses to them. However, the hull shape of the benchmark vessels plays the most essential role in the resistance and losses. As far as the formation of the surface elevation in the wake of the transom has differences, as long as it is strictly dependent on the shape of each transom, as well as in the level of its submergence.

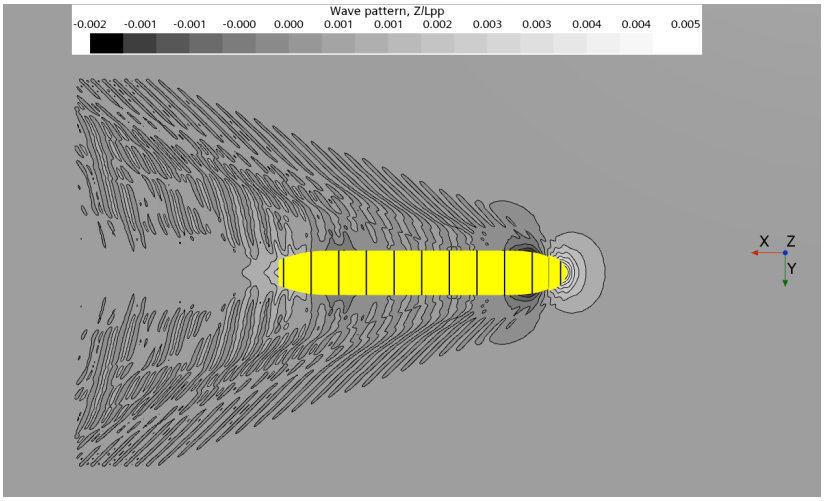

(a) JBC

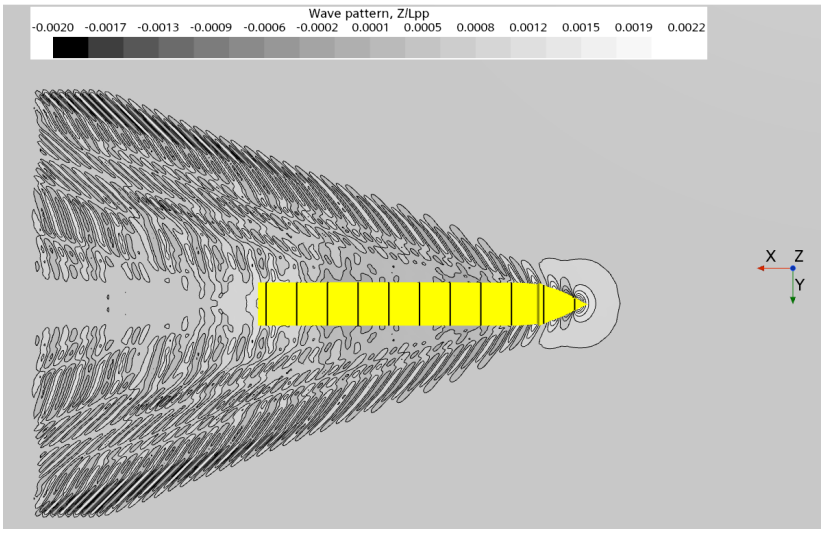

(b) KCS

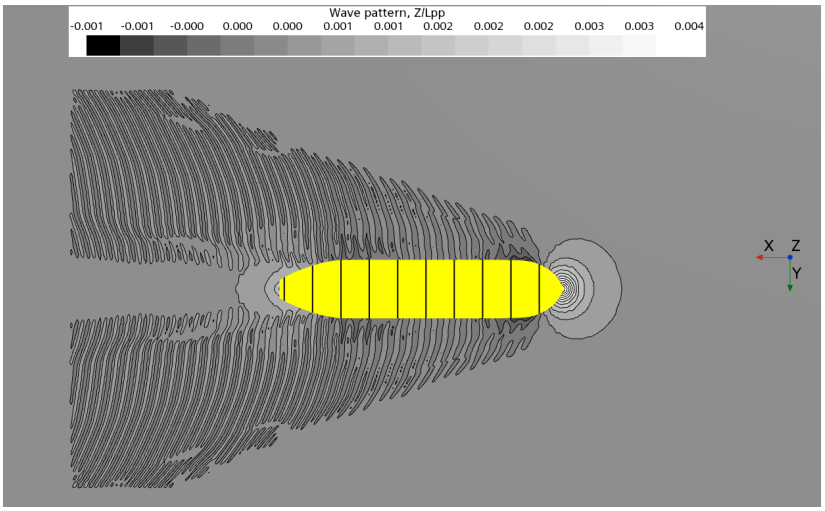

(c) KVLCC2

Figure 4.2: Wave pattern for the JBC, KCS and KVLCC2 test cases in T_s and $Fn = 0.1$ (top view).

4.2 Verification and Validation Analysis

The most crucial part before the sensitivity analysis begins is the V&V analysis of the extracted results in order to ensure that the outcome from the simulations is trustworthy. First of all, sensitivity analysis regarding the grid refinement of the CFD-based form factor prediction of JBC test case, as it has been presented in section 4.5 where the variation of transom submergence has been investigated. Specifically, the variation of the CFD results of k as the grid is finer and finer keeping a constant refinement ratio is presented in Figure 4.3. This specific study tries to investigate the suitability of both turbulence models in MS and FS by comparing the CFD results with the experimental data from Tokyo Workshop 2010. Moreover, a polynomial fit curve of second order which corresponds to the CFD results is added. This fitted curve of the extracted data can provide valuable information about the asymptotic value of form factor when the number of grid cells tend to infinity, i.e. $h_i/h_1 \to 0$. The selected refinement range is $1 < h_i/h_1 < 2$. The refinement ratio of $h_i/h_1 = 1$ in FS indicates that the base cell size is equal to the scale factor ($\lambda = 40$), while the $h_i/h_1 = 2$ represents that it is double increased. In the case of MS the whole domain has been scaled down 40 times, so the $h_i/h_1 = 1$ represents the corresponding coarse grid.

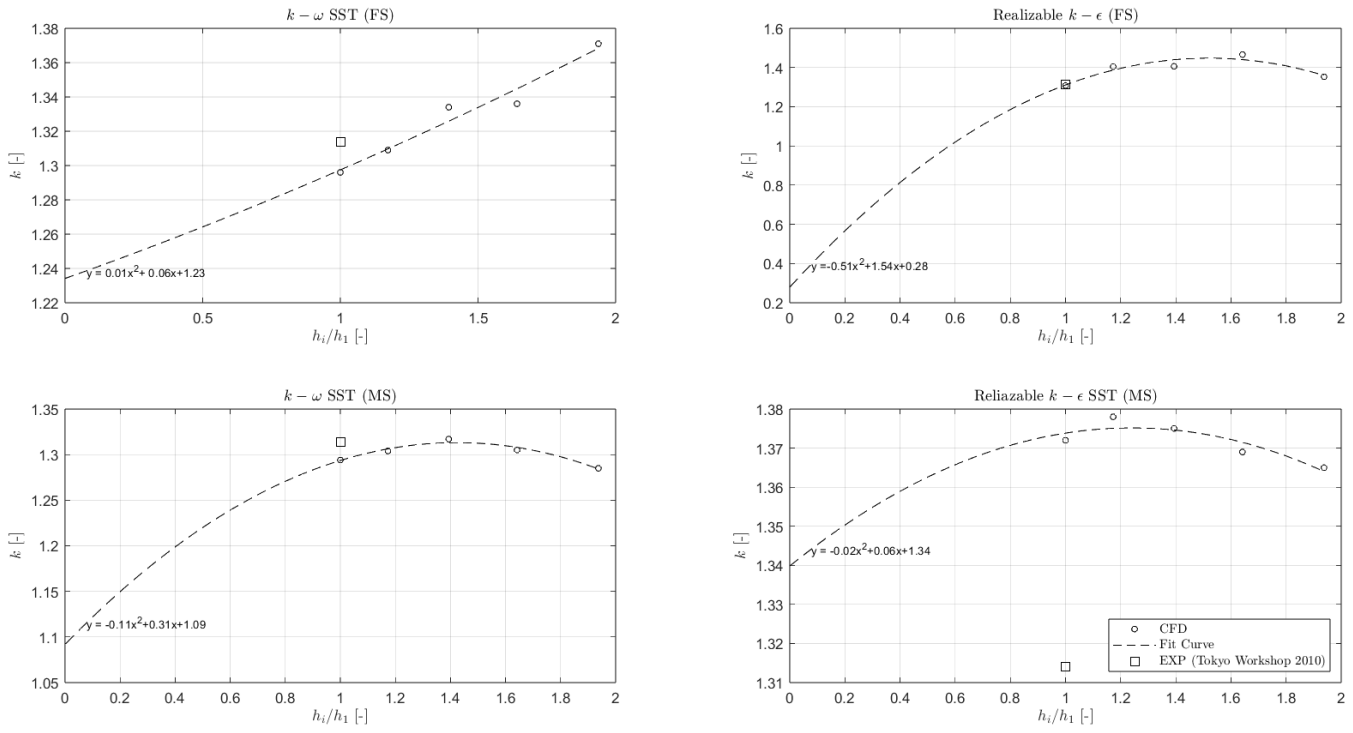

Figure 4.3: Sensitivity analysis of form factor of JBC test case through grid refinement for k - ω SST and realizable k - ϵ models for both MS and FS.

Based on the results illustrated in Figure 4.3, from a turbulence model point of view the k - ω SST model is considered as the most appropriate for the executed simulations in both MS and FS. This can be explained, as the k ω SST model is more compatible and approaches better the flow inside the BL, which is the focus of interest in the present study due to the main contribution of frictional resistance in the total one. In general, the two turbulence models give completely different results, which is also proved in the depicted CFD data of the Figure 4.3 in comparison with the experimental ones. By comparing the CFD with the EFD data between the two studied turbulence models, the

k ω SST is resulted efficient in a great extent giving -1.5 % and -2.1 % discrepancy in FS and MS, respectively. On the other hand, according to the realizable k - ϵ model, the CFD result completely matches with the experimental one in FS, while it gives a discrepancy of 4.3 % in MS. Therefore, the realizable k - ϵ also gives a good approximation of form factor in both scales. In Appendix B, thorough tabular presentation of the results of all resistance coefficient components and form factor is given in Table B.1.

In addition to the grid refinement sensitivity analysis, the discretization error has been investigated for both MS and FS, as well as both turbulence models. The goal is an holistic study of grid uncertainty, since the systematic variation of its refinement is the only factor which can affect the extracted results and include a level of error in the solution of all investigated cases, i.e. turbulence models and scaling. For executing the aforementioned uncertainty analysis, the verification tool from MARIN [MARIN Tool (2022)] has been used. According to the results of this analysis presented in Figure 4.4 for MS all the estimated uncertainties present a consistent behavior, which means that the errors between the different refinement levels have similar magnitude and it is also verified from the low values of uncertainty error. However, the estimated uncertainty of C_V for the case of realizable k - ϵ model indicates weakness to establish the observed order of accuracy p. Moreover, the fact that different uncertainty errors are the result of the same grid refinement ratios shows the impact of each turbulence model on the solution. The inability of realizable k-ϵ model to provide reliable outcome is proved once again, since the error bars for each resistance component cover a broad range of values, especially in the case of C_V. It is mentioned that the uncertainty error depicted in the legend of each graph corresponds to the uncertainty error for $h_i/h_1 = 1$.

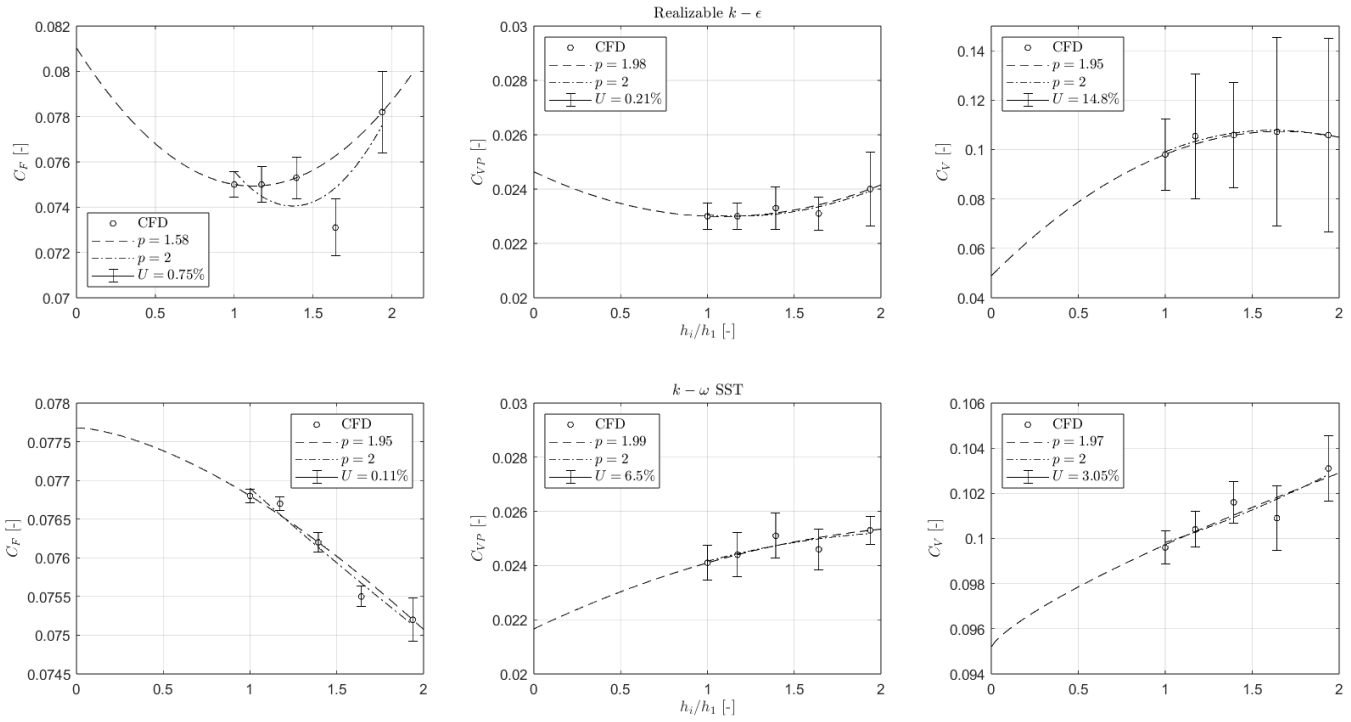

Figure 4.4: Convergence of C_F, C_{VP} and C_V with the grid refinement ratio. Fits obtained from the data with $1 \leqslant h_i/h_1 \leqslant 2$ for k - ω SST and realizable k - ϵ models in MS.

In both Figure 4.4 and 4.5 to orders of accuracy p are depicted. The order of accuracy $p = 2$ is presented in order the asymptotic value for each resistance component to be estimated, which are

illustrated in Table 4.1. As it has been mentioned previously, the asymptotic value can give an prediction of the magnitude of a variable when the number of cells $n \to \infty$. As far as the convergence study of resistance components in FS is concerned, the extracted errors indicate the consistency and convergence of the results for both turbulence models. Therefore, it is proved that the convergence of the three resistance coefficients are independent of the selected turbulent model and give the same rate of uncertainty.

Taking all the above into consideration and having a general conclusion for both convergence studies in MS and FS,based on the chosen grid density and refinement ratios, all the data for k - ω SST model are inside the asymptotic range, which verifies the compatibility of the model in the executed simulations. Furthermore, the convergence of the three studied coefficient do not show similar trends, which is expected since the kinetic energy and the specific dissipation rate of flow in turbulence model are approximated by different differential equations resulting in different results and uncertainties, despite the dependency of resistance components among them.

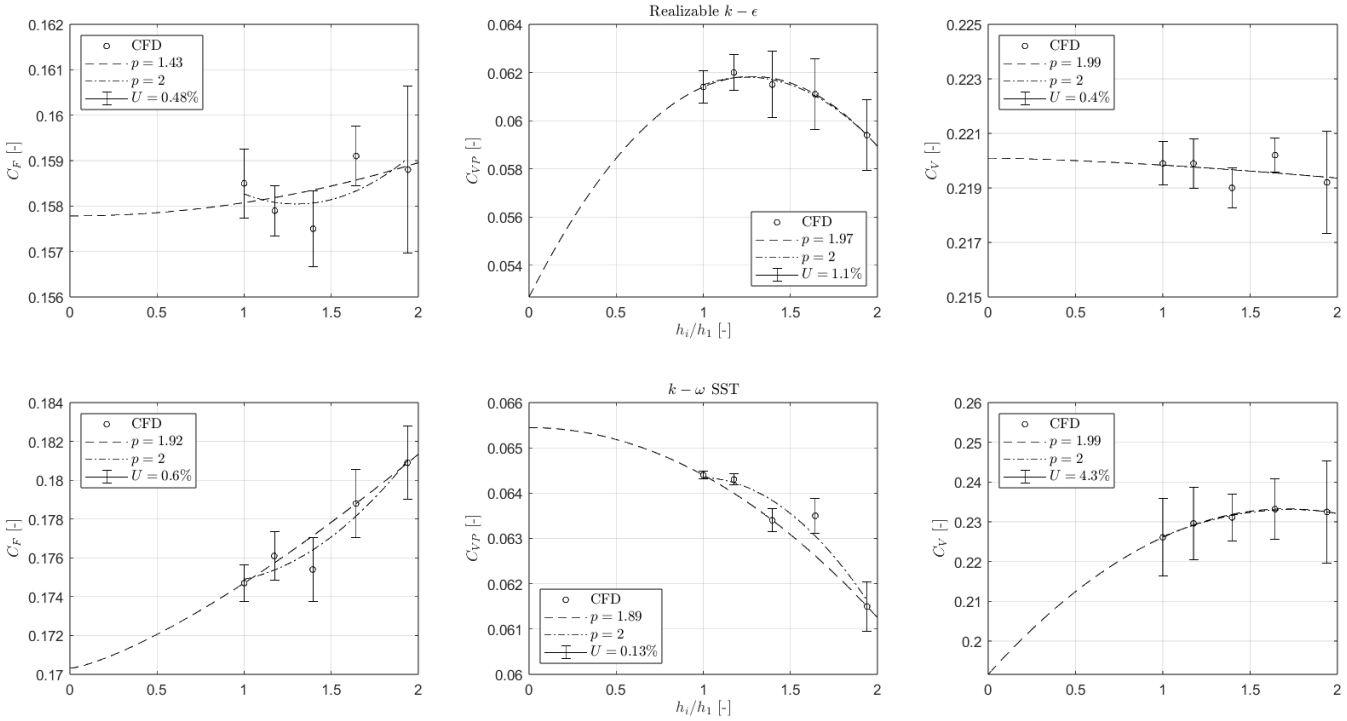

Figure 4.5: Convergence of C_F, C_{VP} and C_V with the grid refinement ratio. Fits obtained from the data with $1 \leqslant h_i/h_1 \leqslant 2$ for k - ω SST and realizable k - ϵ models in FS.

Table 4.1: Asymptotic values of C_F, C_{VP}, C_V and k for JBC.

Scale	Turbulence Model	C_F [-]	C_{VP}[-]	C_V[-]	k [-]
FS	k-ω SST	0.07768	0.02166	0.00951	1.231
	Realizable k-ϵ	0.08103	0.02464	0.04887	0.282
MS	k-ω SST	0.17031	0.06545	0.19163	1.092
	Realizable k-ϵ	0.15778	0.05269	0.22009	1.342

In addition to the aforementioned analyses, a study about the iterative error has been implemented via the open-source MARIN Validation Tool [MARIN Tool (2022)]. This study is executed for both

turbulence models and both scales by using the DB model. In general, the iterative errors are related to different characteristics of the solution process, such as corrections in spatial discretisation, linearization of the convective terms etc. [Eca L. et al. (2019)]. The mentioned characteristics have similarities in steady and unsteady flows. Nevertheless, iterative errors are more difficult to be determined in unsteady simulations due to its propagation from a given time-step to the next one.

Taking into consideration this characteristic the iterative errors are studied only for the DB approach, in which steady-state simulation is applied. The iterative error is predicted through the difference between a ϕ_{it} computed with a convergence criterion ϵ_{it} and a solution derived via reduction of the error to machine accuracy ϕ_m. Thus, the iterative errors are estimated by the Equation 4.2.

$$\epsilon_{it}(\phi_{it}) = \phi_{it} - \phi_m \tag{4.2}$$

In the following Figure 4.6 and 4.7 the iterative error of C_F is presented in MS and FS, respectively. The selection of C_F for the study of iterative error is made, because it constitutes the main factor for the form factor estimation, as it has been mentioned above. In case of MS, 2000 iterations has been selected, whereas 10000 iterations are applied for the FS simulations. Observing the Figure 4.6, the simulations are completed before they reach the whole 2000th iterations, which means that the results are converged relatively rapidly. Moreover, the first 1400 (MS) and 2000 (FS) iterations have been removed from the graphical depiction, because the intensive oscillations in the beginning of simulation are not of a high interest for the prediction of iterative error. Therefore, the illustrated fir curves have a linear trend and represent the average value of the error.

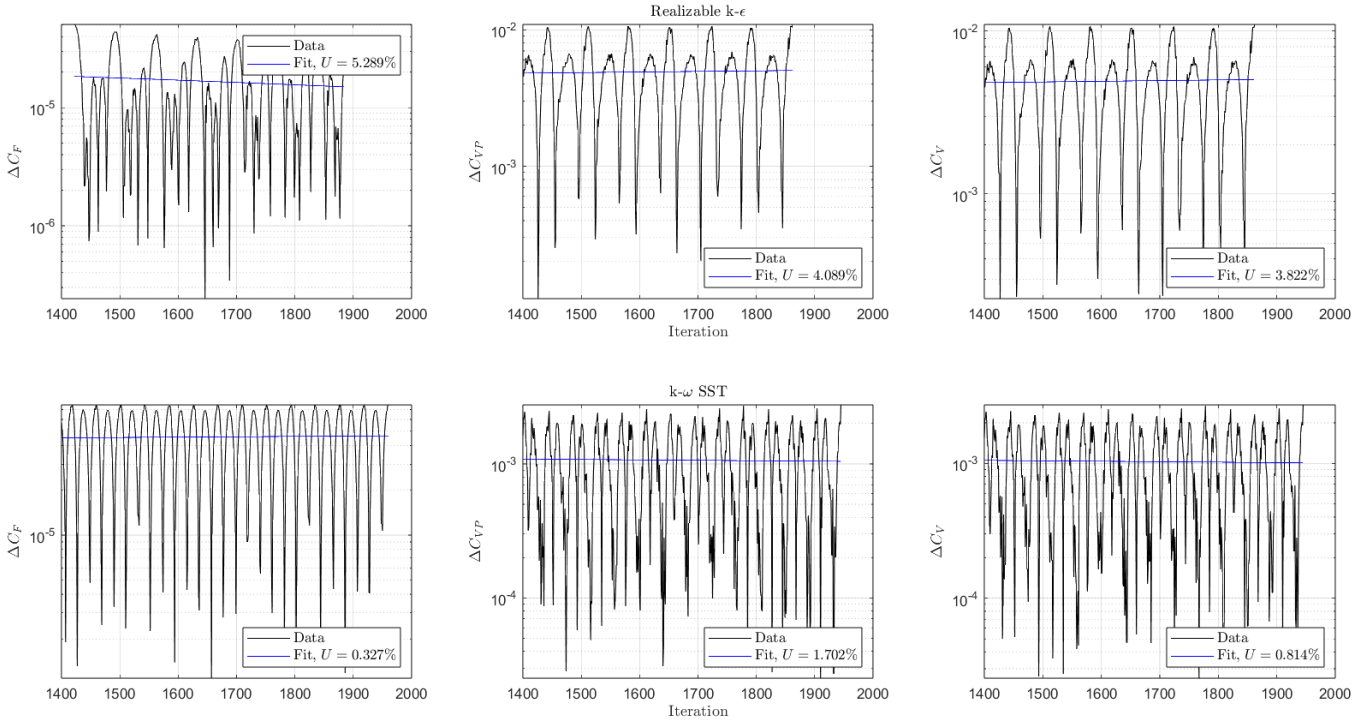

Figure 4.6: Iterative error of C_F for k - ω SST and realizable k - ϵ models in MS using the DB approach.

In the Table 4.2, 4.3 and 4.4, the results of the GCI estimation is introduced for each of the three benchmark test cases. The sequence of calculations for the GCI prediction is based on relations been presented in the subsubsection 3.4.1.1. In particular, the GCI can give valuable insights into the grid

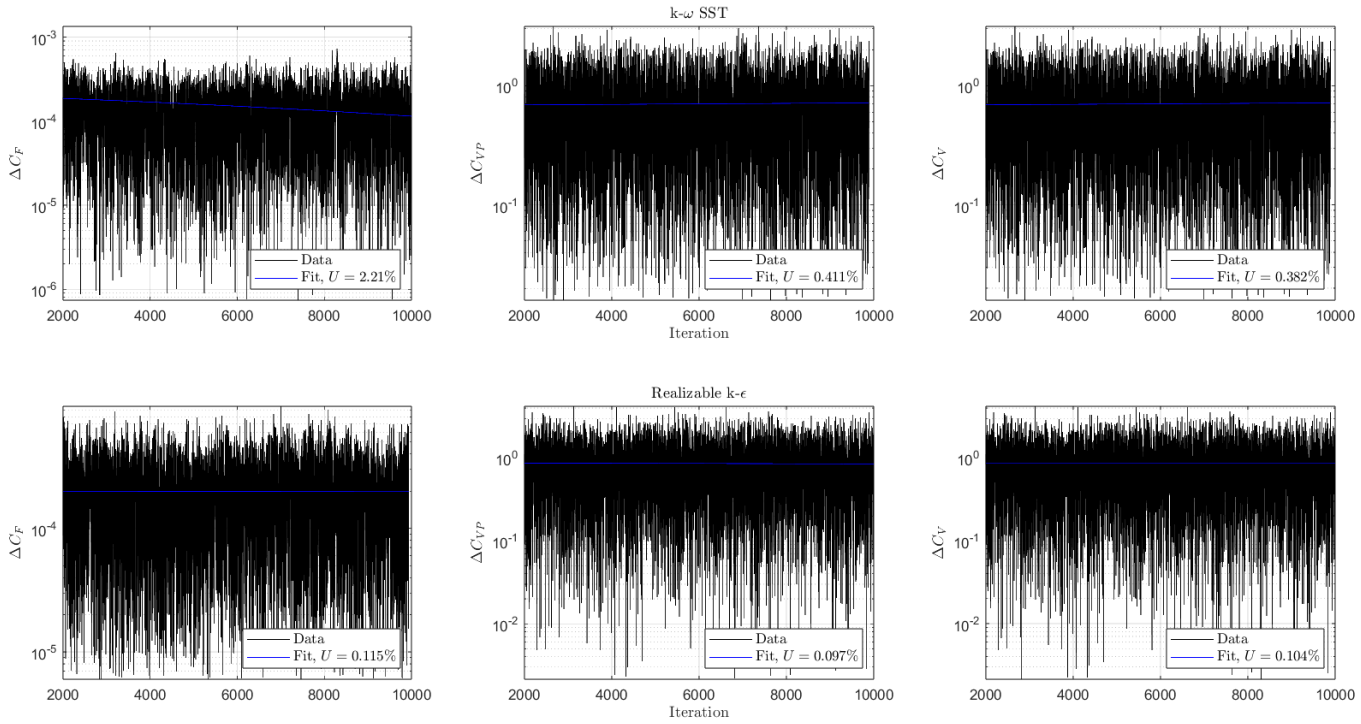

Figure 4.7: Iterative error of C_F for k - ω SST and realizable k - ϵ models in FS using the DB approach.

convergence of the solution providing an error band. Two levels of grid refinement has been used, a medium and a fine one. Therefore, test of whether the solution is within the asymptotic range of convergence or not is applied. Being a measure of the percentage of how much discrepancy has the computed from the asymptotic numerical value, the GCI indicates the rate of change with a further refinement of grid.

According to the depicted results in the following tables, the indices 1, 2 and 3 correspond the finest grid refinement ratios of Table 3.11. This analysis has been executed for MS and FS, as well as the k -ω SST model, because this is considered the most compatible model for the C_F estimation and by extension for the form factor prediction. The GCI_{medium} gives a broader error band than the GCI_{fine} in the C_F computation for all the test cases and both scales. This can verify that the grid convergence is effective giving reliable results and the computation of C_F is within the asymptotic range. As far as the C_{VP} computation is concerned, its error band is resulted higher for the finer grid than the coarser. An explanation for this outcome is the potential existence of discontinuities in the flow field and turbulence phenomena which cannot be captured. Finally, the GCI estimation for the k give a more qualitative picture of the grid convergence, since the form factor constitutes a derivative of C_F and C_T and it is closely dependent on them.

Table 4.2: Estimation of spatial discretization error for model and full scale using the $k-\omega$ SST model (JBC).

	MS				FS			
	C_F [-]	C_{VP} [-]	C_V [-]	k [-]	C_F [-]	C_{VP}[−]	C_V [-]	k [-]
r_{21}	1.180	1.180	1.180	1.180	1.180	1.180	1.180	1.180
r_{32}	1.178	1.178	1.178	1.178	1.178	1.178	1.178	1.178
ϕ_1	0.1332	0.0499	0.1831	0.1332	0.0086	0.0027	0.0113	1.316
ϕ_2	0.1288	0.0495	0.1783	0.1288	0.0085	0.0027	0.0113	1.318
ϕ_3	0.1326	0.0491	0.1817	0.1326	0.0085	0.0028	0.0112	1.324
p	-14.41	0.74	-2.05	2.06	0.74	-2.05	2.06	2.06
ϕ_{ext}^{21}	0.158	0.052	0.209	1.319	211163	61652	275552	1.305
e_a^{21}	3.31%	0.72%	2.61%	0.73%	0.72%	2.61%	0.73%	0.73%
e_{ext}^{21}	0.82%	6.78%	0.05%	2.29%	3.86%	12.66%	4.23%	6.45%
GCI_{fine}^{21}	1.03%	7.94%	0.06%	1.09%	5.02%	18.11%	5.07%	5.07%
GCI_{medium}^{32}	4.72%	7.56%	1.75%	2.99%	5.77%	13.39%	7.15%	7.15%

Table 4.3: Estimation of spatial discretization error for model and full scale using the $k-\omega$ SST model (KCS).

	MS				FS			
	C_F [-]	C_{VP} [-]	C_V [-]	k [-]	C_F [-]	C_{VP}[−]	C_V [-]	k [-]
r_{21}	1.180	1.180	1.180	1.180	1.180	1.180	1.180	1.180
r_{32}	1.178	1.178	1.178	1.178	1.178	1.178	1.178	1.178
ϕ_1	0.0984	0.0103	0.1087	1.104	0.0767	0.0100	0.0867	1.131
ϕ_2	0.0977	0.0108	0.1084	1.110	0.0767	0.0100	0.0867	1.131
ϕ_3	0.0972	0.0115	0.1087	1.119	0.0766	0.0101	0.0867	1.131
p	-2.45	2.45	0.00	2.03	-0.54	1.40	-8.38	1.12
ϕ_{ext}^{21}	4.007	0.289	4.295	1.07	81850	10541	92391	1.128
e_a^{21}	0.78%	5.00%	0.24%	0.55%	0.04%	0.22%	0.01%	0.03%
e_{ext}^{21}	4.16%	38.46%	1.29%	3.92%	0.24 %	1.21 %	0.07%	0.17%
GCI_{fine}^{21}	5.43%	34.72%	1.64%	3.82%	0.30 %	1.50%	0.09%	0.21%
GCI_{medium}^{32}	3.69%	50.17%	1.66%	5.38%	0.28%	1.91%	0.02%	0.25 %

Table 4.4: Estimation of spatial discretization error for model and full scale using the $k-\omega$ SST model (KVLCC2).

	MS				FS			
	C_F [-]	C_{VP} [-]	C_V [-]	k [-]	C_F [-]	C_{VP}[−]	C_V [-]	k [-]
r_{21}	1.180	1.180	1.180	1.180	1.180	1.180	1.180	1.180
r_{32}	1.178	1.178	1.178	1.178	1.178	1.178	1.178	1.178
ϕ_1	0.0927	0.0290	0.1218	1.313	0.0233	0.0066	0.0332	1.247
ϕ_2	0.0924	0.0295	0.1219	1.319	0.0266	0.0066	0.0332	1.247
ϕ_3	0.0917	0.0302	0.1219	1.329	0.0266	0.0066	0.0332	1.247
p	4.19	3.38	0.00	3.61	-37.48	3.38	-0.68	6.91
ϕ_{ext}^{21}	8.407	2.358	10.764	1.279	98966	24367	123334	1.246
e_a^{21}	0.36%	1.55%	0.09%	0.46%	0.05%	0.10%	0.06%	0.01%
e_{ext}^{21}	1.98%	9.43%	0.52%	4.41%	0.29%	0.55%	0.34%	0.15%
GCI_{fine}^{21}	2.53%	10.77%	0.64%	3.18%	0.36%	0.68%	0.42%	0.06%
GCI_{medium}^{32}	5.13%	18.77%	0.65%	3.18%	0.18%	1.20%	0.38%	0.20%

The final analysis executed in the context of report of the implemented simulations and the extracted results is the validation analysis which has been introduced in subsection 3.4.2. As it has been mentioned previously, the validation assessment verifies if the executed simulation is in agreement with the physics and compares the CFD data with the experimental ones. The mentioned comparison is made between the absolute value of comparison error and the validation uncertainty, Equation 3.26 and 3.27. The experimental uncertainty in calm water has been obtained from the database of FORCE Technology, where the KCS model has been tested in the towing tank. Due to the fact that there is no available data of the U_V for JBC and the two commercial hulls, the one of KCS, $U_D = 0.95\%$, is used as a verified value for their validation assessment. Experimental uncertainty for the rest of benchmark hulls of KVLCC2 and DTMB 5415 is derived from the available data of Gothenburg Workshop. Therefore, based on the illustrated results of Table 4.5, all the executed simulations are considered validated since the criterion of $|E| < U_V$ is satisfied. Validation evaluation is not applied for the test case of ONRT, because there is lack of available experimental data, but it can be proposed as recommendation for future research work.

Table 4.5: Validation analysis for all the test cases.

Test Case	$C_T \times 10^{-4}$ [-] (CFD)	$C_T \times 10^{-3}$ [-] (EFD)	E [%]	U_D [%]	U_{SN} [%]	U_V [%]	Comparison
JBC	3.54	4.29	0.397	0.95	3.05	3.19	$\|E\| < U_V$
KCS	3.54	3.80	0.344	0.95	5.17	5.26	$\|E\| < U_V$
KVLCC2	2.17	4.11	0.389	0.424	4.23	4.28	$\|E\| < U_V$
DTMB 5415	0.16	0.39	0.373	0.514	7.93	7.95	$\|E\| < U_V$
ONRT	0.60	-	-	-	9.25	-	-
180K BC	2.47	4.48	0.201	0.95	4.94	5.03	$\|E\| < U_V$
82K BC	3.63	4.15	0.378	0.95	5.22	5.30	$\|E\| < U_V$

4.3 Scaling Sensitivity Analysis

A systematic analysis of different scaling factors is implemented. Specifically, an investigation of changing the scale factor of the three benchmark hulls of JBC, KCS and KVLCC2 is executed in order its impact on the C_F, C_{VP} and C_V to be studied. Apart from the cases of model and full scale, six additional scale factors ($\lambda_i = \lambda/16, \lambda/8, \lambda/4, \lambda/3, \lambda/2$) have been tested. The main goal of this specific analysis is the effect of the variation of scale factor on the components of resistance and the level of their reliability. The change of the scale factor is executed by modifying the scaling of each hull geometry based on each test case.

In Figure 4.8, the representation of the CFD results and their comparison among the three test cases is made by the corresponding values of Re number according to each scale factor. Therefore, the $Re = 5.225 \times 10^6$ corresponds to the model scale, while the $Re = 1.322 \times 10^9$ indicates the full scale case. It is obvious from the depicted results that the extracted values of all the three test cases and all the resistance coefficients tend to a constant value when the scale factor decreases or Re number increases, in other words. In particular, essential variation on the results is observed for scale factors higher than $\lambda_i = 1/3\lambda$, or $Re > 5.842 \times 10^7$, where the C_F is more intensively affected since it is the main contributor of the total resistance, because the inflow speed has been set to be in a low Fn value. This can be explained as changing the scale factor of the studied geometry also affects promptly the grid configuration of the computational domain, such as the number of cells, height of the first cell near to the wall of geometry and boundary layer thickness. Consequently, based on the illustrated results of Figure 4.8 , as well as the grid characteristics of each executed simulation which

corresponds to different scale factors, change of λ has an upper limit over which it no longer has an impact to the aforementioned resistance coefficients.

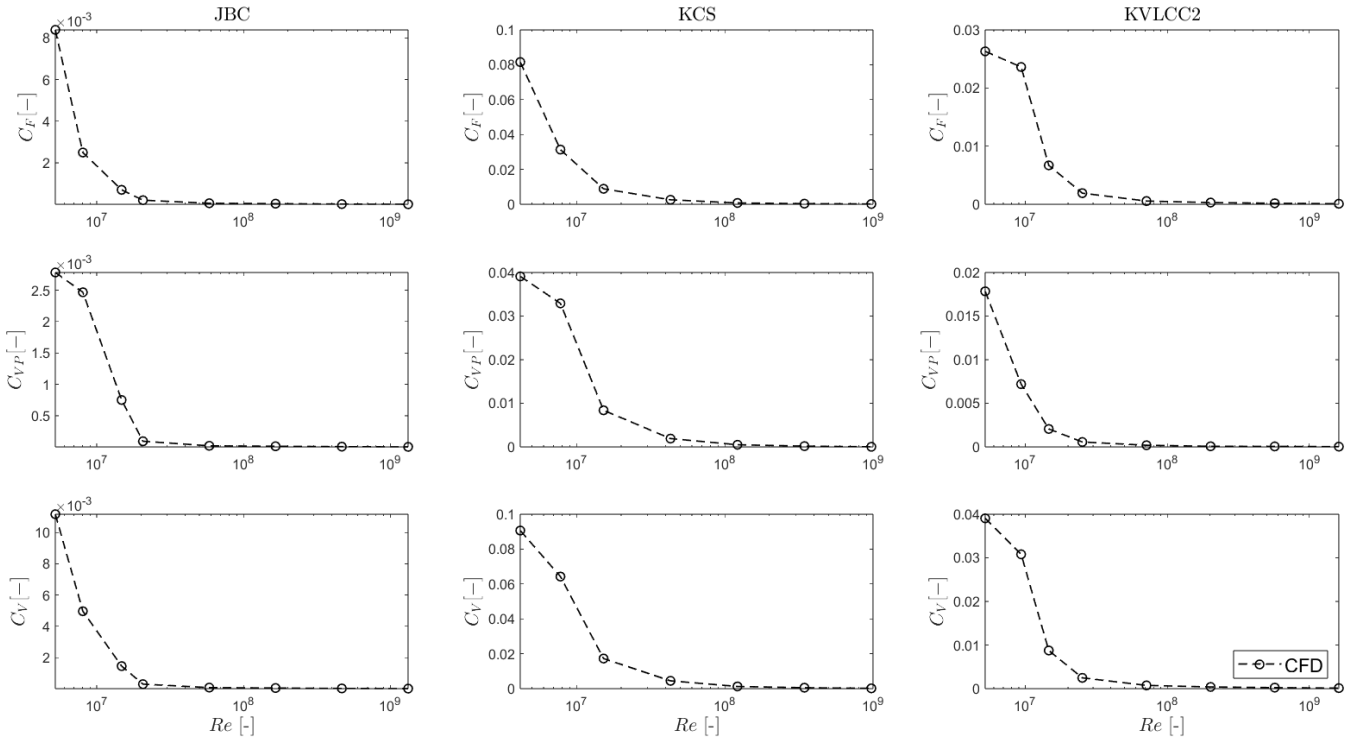

Figure 4.8: Systematic analysis of C_F, C_{VP} and C_V by changing scale factor of JBC (left), KCS (middle) and KVLCC2 (right).

In Figure 4.9, the variation on the form factor by changing the scale factor is presented by comparing it with the EFD results from Tokyo and Gothenburg Workshops. The extracted values of form factor result implicitly from the Equation 2.19, which indicates the effect between C_F and C_V. According to the form factor results, the discrepancy between CFD and EFD results varies in the broad range from 0.5 % to 35 %. The highest discrepancies are observed for the test cases of JBC and KCS and $1/4\lambda$ and $1/8\lambda$, respectively. In these cases, the generated grid does not adapt onto the wall in a way to satisfy the BL characteristics so as the abrupt flow variations to be captured in this region of the domain. This grid weakness is due to its lack of adaptation with these certain scaling factors. For both JBC and KCS cases the results of k present a decreasing trend from MS to FS, which can be considered as a positive aspect, because the CFD results in FS can be assumed as reliable. Based on the depicted results, the form factor estimation between the MS and FS is not considered as reliable. On the other hand, the CFD-based results of k for KVLCC2 perform arbitrary fluctuations with a lower discrepancy of 14 % in comparison with EFD one. This occurs because KVLCC2 is a bulky hull with high C_B and the fluid flux cannot remain attached onto the hull surface. As a result, a fast flow separation is created in the fore part of the hull and this leads to development of turbulence, which affects the C_T, C_{VP}, and C_F. In Table C.1, C.2 and C.3 of Appendix C, the extracted results are presented thoroughly.

4.4 Roughness Sensitivity Analysis

The second executed systematic analysis is related to the roughness height of the hull surface in FS. The mentioned analysis is also implemented for the test cases of JBC, KCS and KVLCC2 using the

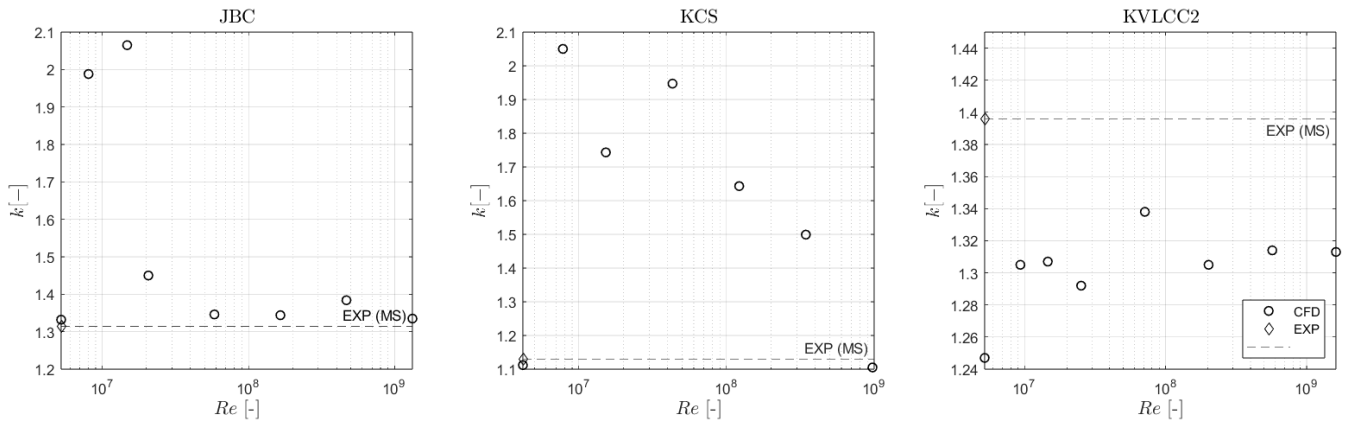

Figure 4.9: Sensitivity of form factor by changing scale factor.

first approach mentioned in subsection 3.3.3, that is applying a point force in the center of gravity of hull. As it is referred in subsection 3.3.3, the AHR is set equally distributed as a constant value in the whole hull surface for all the test cases. That means there is no variation of roughness height along the hulls. According to the depicted results of Figure 4.10, increase of all resistance components is noted for a roughness range of $150 < AHR < 250\ \mu m$. This occurs due to the fact that the first cell height of the generated grid near to the wall does not include the roughness heights, which exceed the critical value of 250 μm. It is apparent that effort for improving this issue by increasing the thickness of the first cell can lead to difficulties in capturing the fast flow fluctuations inside the BL, as well as keeping the y^+ value into the recommended range. Taking into account the range of roughness heights where the C_F and C_{VP} perform an increased trend, it can be noticed that inclusion of roughness as a constant value leads to an approximate 9 % increase of C_F and a 7.5 % increase of C_{VP} for the three test cases inside the aforementioned AHR range. The C_V is a result of the other two resistance components and it shows an 8.5 % increase.

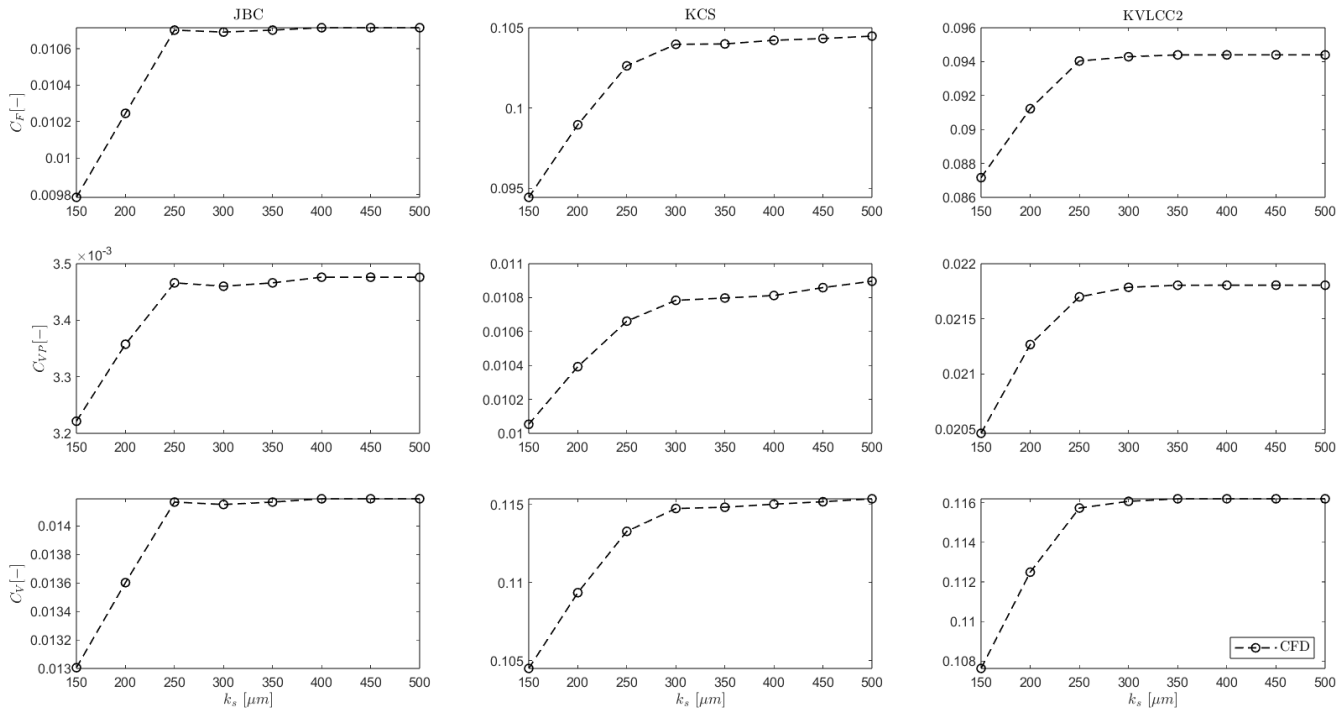

Figure 4.10: Systematic analysis of C_F, C_{VP} and C_V by changing roughness height onto the surface of JBC (left), KCS (middle) and KVLCC2 (right).

In Figure 4.11 below, the sensitivity of form factor through increase of roughness height is presented. It is visible that a constant trend is resulted for all the three test cases. In other words, the ratio between the C_F and C_V does not change substantially and it seems that the k is not closely dependent on the surface roughness. The relation between the first cell height and the roughness height, which was discussed above, is the decisive factor for the lack of any significant trend in the extracted results of k. In Table D.1 of Appendix D, the extracted results are illustrated in detail.

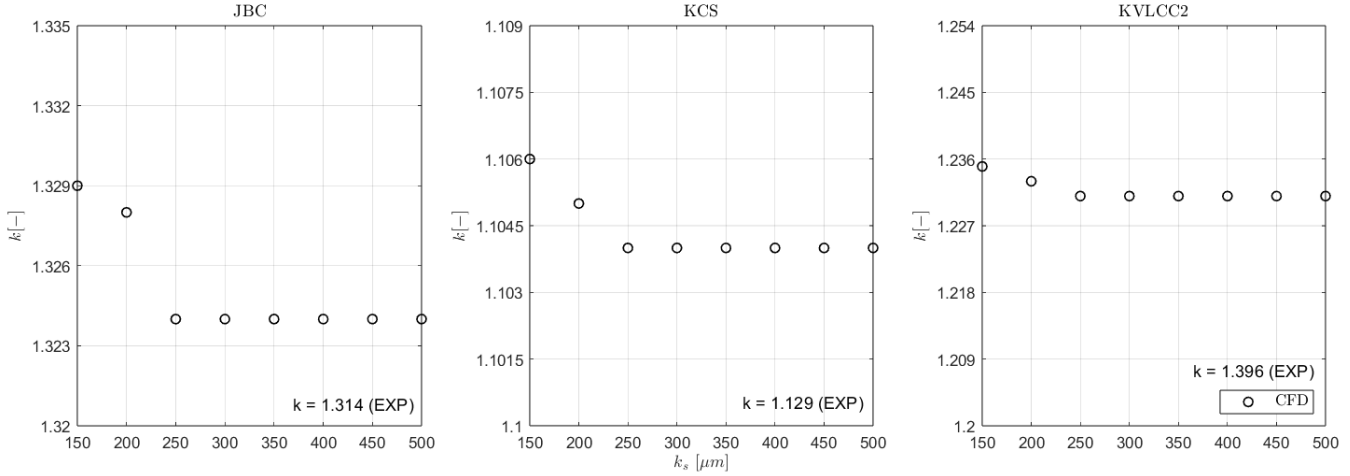

Figure 4.11: Sensitivity of form factor by changing roughness height.

The local flow behind the transom of the three aforementioned test cases has been studied for both MS and FS in scantling draft, excluding roughness height (smooth surface). In Figure 4.12, comparison of the results between MS and FS is presented by using the F-S model. The F-S model is chosen in order for any potential impact of the free surface to be detected. Presenting the u/U isocurves at

the wake of transom, that is $x/L_{PP} = -0.05$, where $x/L_{PP} = 0$ corresponds to the aft perpendicular.

Although the Re number is significantly increased from MS to FS, the results indicate that no significant change is observed between the two scales. Furthermore, a slight difference of the isocurves of wake is detected in two main regions for all the test cases, which are in the skeg vortex and close to the free surface. These local flow discrepancies are expected in these certain areas since intensive phenomena of vorticity can be noticed, which can affect drastically the general picture of the wake from MS to FS. In other words, the wake behind the transom is developed alternatively when one compares two different scales. Moreover, one can verify that the flow separation behind the three hulls in MS is wider than in FS. As a total observation, the wake behind the hulls of the three test cases becomes smaller from MS to FS, which can verify the proposal made by [Korkmaz K.B. et al. (2022)] about the division of the C_{VP}, through which the $2-k$ method is introduced.

In the following Figure 4.13, 4.14 and 4.15, visualization of the normalized axial velocity in the wake by using the DB model and increasing gradually the ARH in FS is illustrated. According to the depicted results, there is no significant change in the wake of the hulls through the increase of ARH. The only observable change for all the test cases in in the skeg vortex, which is more and more spread as the ARH increases. This spreading is negligible in the rest of the wake field, because the biggest percentage of the illustrated wake is related to the bilge vortex, in which such a gradual increase of ARH does not have any visible impact to the wake behind the transom that is quite downstream. Finally, the reason why the DB model is used to implement this analysis of roughness is the lower computational cost and saving of time for the execution of CFD simulations.

4.5 Systematic Variation of Transom Submergence

Investigation of several drafts is implemented in order to evaluate the effect of transom submergence on the local flow behind the transom, since it constitutes an inextricable part of $2-k$ method. The benchmark hull of JBC and the two commercial hulls (180K BC, 82K BC) have been chosen for this systematic analysis. The two commercial hulls are selected since model test EFD results are available on the database of FORCE Technology. In this way, it is possible the validation of the executed CFD simulations to be tested.

The analysis is executed in MS and FS, as well as for smooth and rough ($AHR = 150\ \mu m$) hull cases using the F-S model. Furthermore, the Prohaska method is applied for the estimation of the ratios C_{Tm}/C_{Fm} and C_{Ts}/C_{Fs} in MS and FS, respectively. Specifically, according to the Prohaska method (section 2.2), the k estimation is made by obtaining the asymptotic values of each trendline of the CFD results. As one can see from Figure 4.16, the trend of the CFD results for each draft is consistent and no significant variation is observed. This is visible even for the case of the two commercial hulls, whose the geometry is custom-made and it could present discontinuities in their surface curvature and affect drastically the final CFD results.

Based on the extracted results of JBC test case, the plotted trendlines are parallel to each other and they give higher and higher values of k as the draft increases. This is considered reasonable, because the draft increases as the transom is immersed, which creates intense recirculation in its wake and this has impact on k prediction. It is apparent that the trendlines of the two higher drafts and for $Fn^4/C_{Fm} > 0.016$ cross each other, which is due to the uncertainty of the results created by the high level of vorticity. According to the results of the 180K and 82K hulls, which are more distinct in Figure 4.17, four more CFD simulations has been executed for each of the studied drafts so that

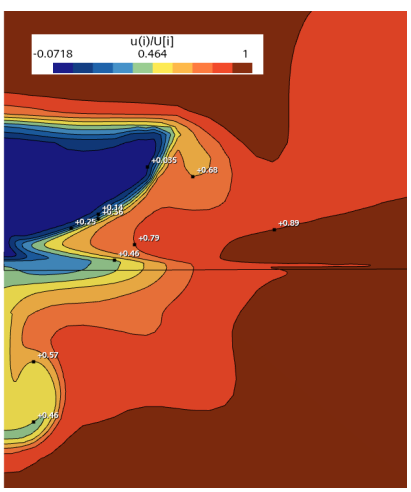

(a) JBC (MS)

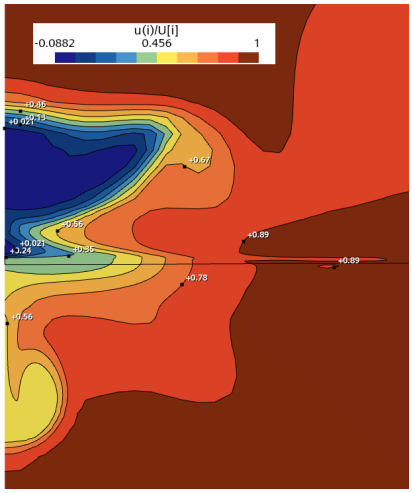

(b) JBC (FS)

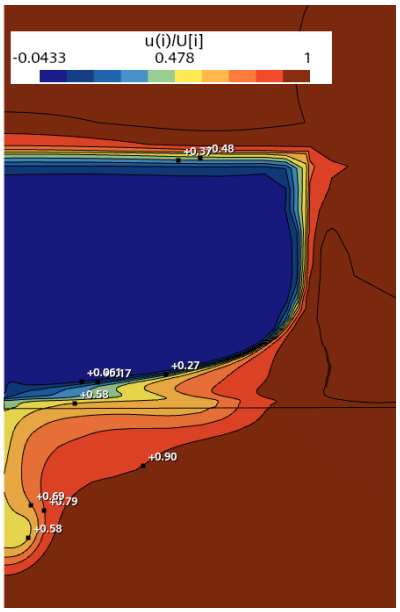

(c) KCS (MS)

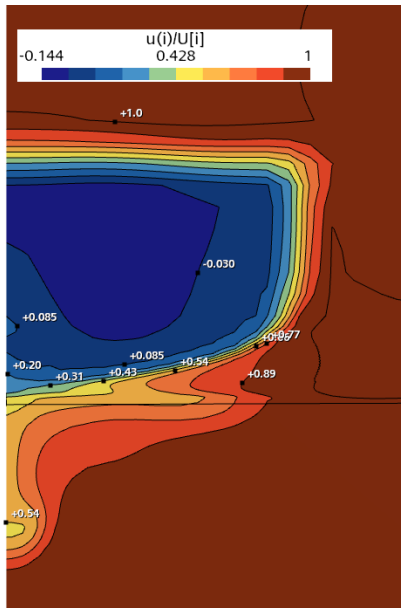

(d) KCS (FS)

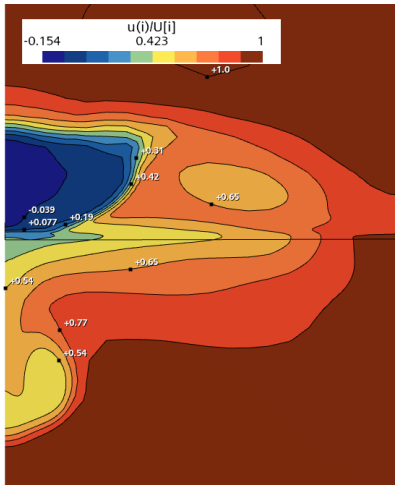

(e) KVLCC2 (MS)

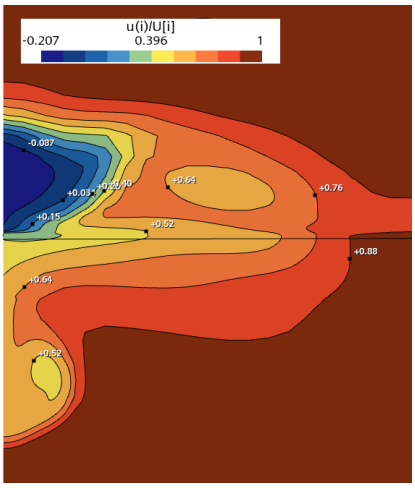

(f) KVLCC2 (FS)

Figure 4.12: Normalized axial velocity of the wake at $x/L_{PP} = -0.05$ for T_s and $Fn = 0.1$ in both MS and FS (F-S, $k - \omega$ model, ARH = 0).

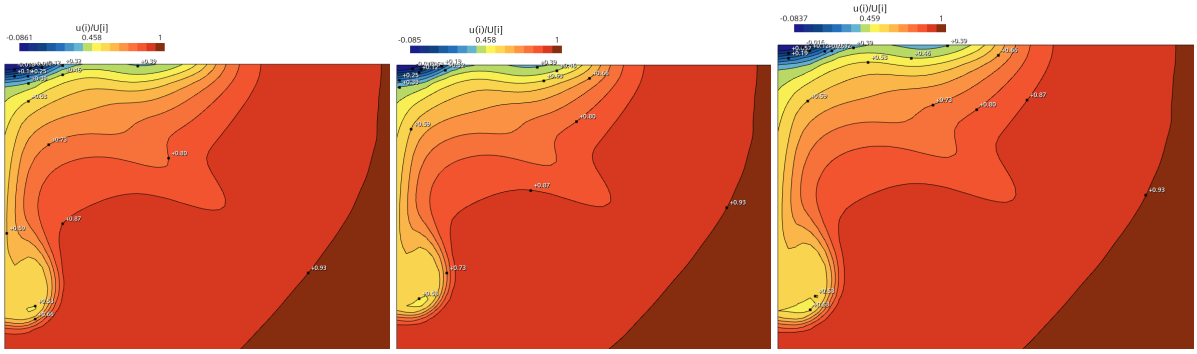

(a) ARH = 150 μm (b) ARH = 200 μm (c) ARH = 250 μm

Figure 4.13: Normalized velocity of the wake for the test case of JBC for T_s and $Fn = 0.1$ in FS for different ARH values (DB, $k - \omega$ model).

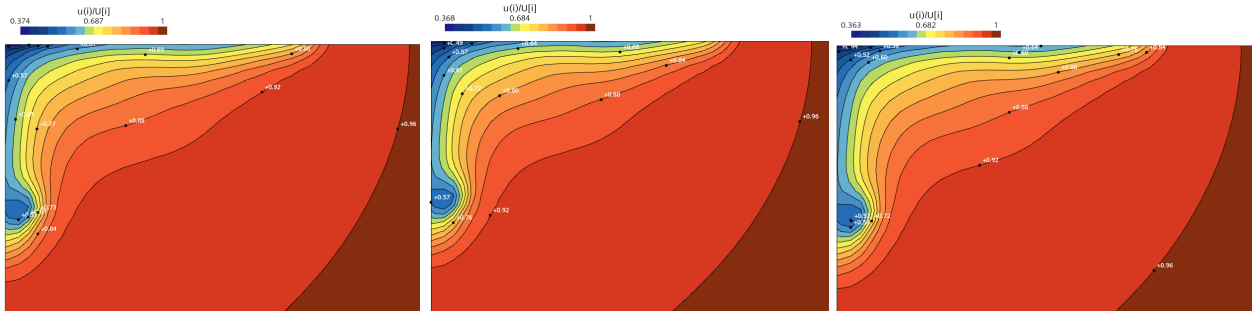

(a) ARH = 150 μm (b) ARH = 200 μm (c) ARH = 250 μm

Figure 4.14: Normalized velocity of the wake for the test case of KCS for T_s and $Fn = 0.1$ in FS for different ARH values (DB, $k - \omega$ model).

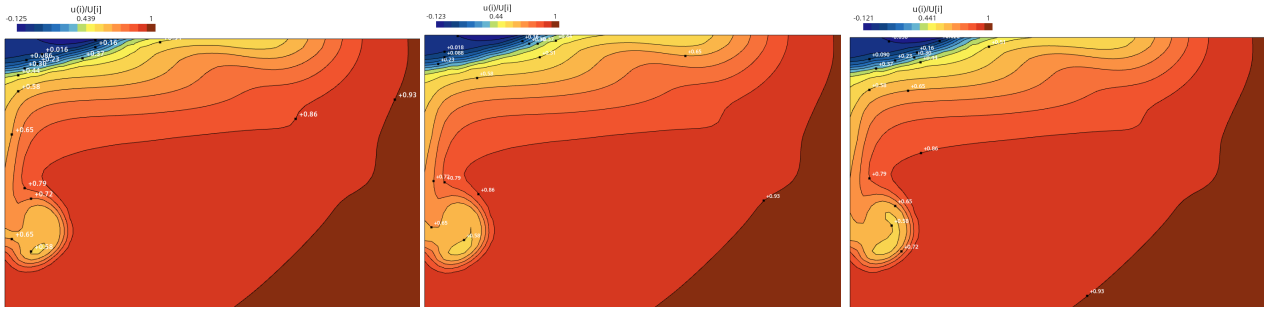

(a) ARH = 150 μm (b) ARH = 200 μm (c) ARH = 250 μm

Figure 4.15: Normalized velocity of the wake for the test case of KVLCC2 for T_s and $Fn = 0.1$ in FS for different ARH values (DB, $k - \omega$ model).

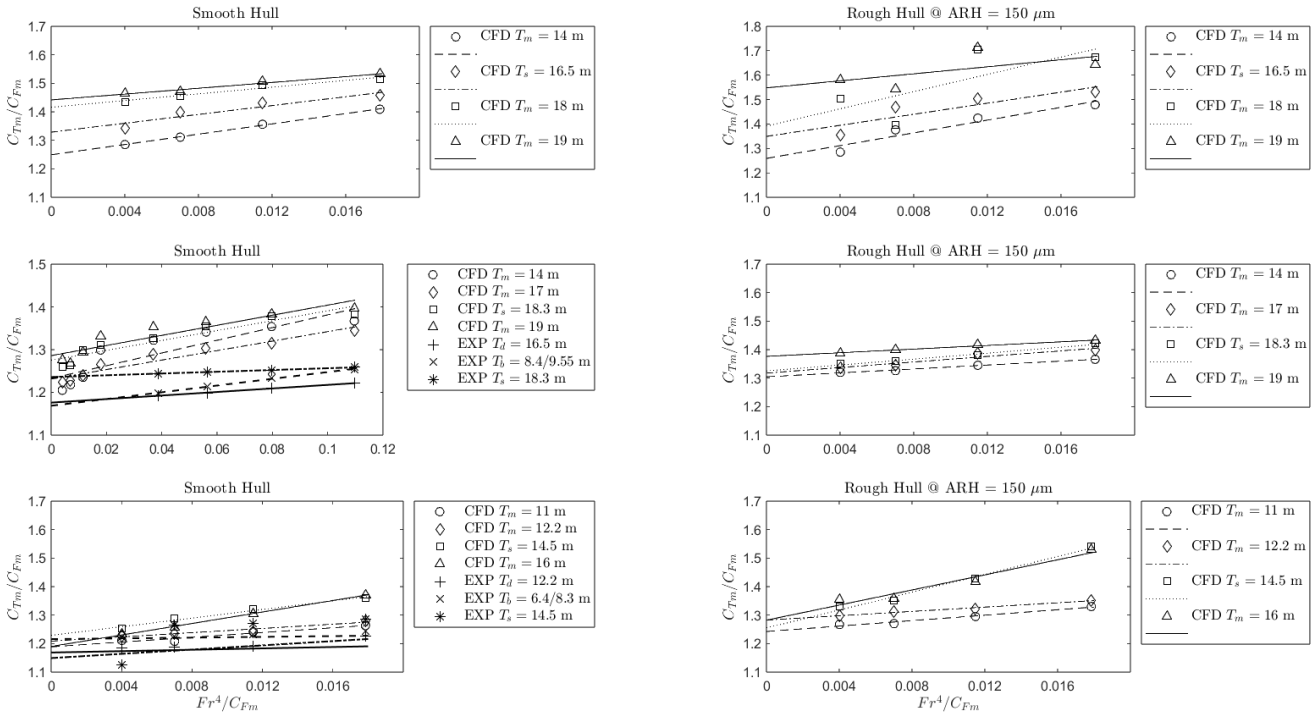

Figure 4.16: Sensitivity of C_{Tm}/C_{Fm} with variation of draft as function of normalized Fn number for the test cases of JBC, 180K BC and 82K BC (smooth + rough) in MS by using the Prohaska method and F-S model.
JBC (top), 180K BC (middle), 82K BC (bottom)

the CFD results correspond to the EFD ones.

Taking into account the asymptotic value of the ratio C_{Tm}/C_{Fm} in scantling draft resulted from the Prohaska method, comparing it with the corresponding EFD results, there is a discrepancy less than 2 % and 4.5 % for 180K and 82K, respectively. Even though the EFD results present different inclination of their trendline in both test cases and the EFD results of 82K BC scatter, one can observe low values of discrepancy. Therefore, the implementation of the CFD model scale simulations can be considered reliable. On the other hand, the CFD results performs intensive scattering for the 180K BC test case in the range of $0.005 < Fn^4/C_{Fm} < 0.02$, which is expected because the frictional and viscous pressure resistances do not tend to converge for such a low level of speed, even after a high number of iterations when the F-S is used. Consequently, the solution for overcoming this weakness is the increase of inner iterations in the stage of pre-process.

Regarding the systematic variation of transom submergence in FS, the results presents a consistent behavior, not resulting in a broad range of C_{Ts}/C_{Fs} asymptotic values, especially for the JBC test case, as one can see in Figure 4.18. This can verify that when the Prohaska method is applied for CFD-based form factor predictions in FS is proved trustworthy even for speed-power predictions. Once again, the trendlines of the CFD results present intersections to each other for $Fn^4/C_{Fs} > 0.03$, which means different gradient among them. In FS simulations, when the free surface elevation is taken into account and transom submergence is studied, the ratio C_{Ts}/C_{Fs} is sensitive due to the fact that the wave generation starts to be a contributor to the total resistance. Even if the wave elevation is not significant because of the low Fn numbers, it still affects in some extent the ratio of total over frictional resistance.

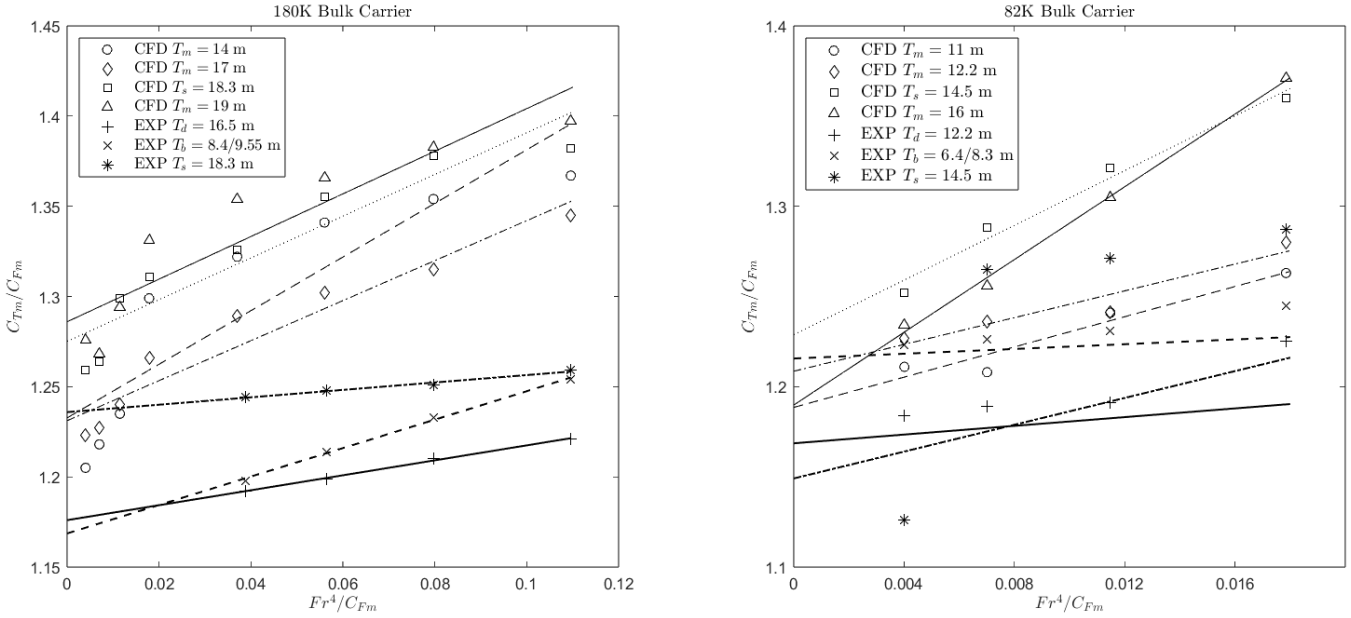

Figure 4.17: Detailed plots of the results for the 180K BC and 82K BC smooth hull case.

In Figure 4.19 and 4.20 the local flow behind the transom of JBC , KCS and KVLCC2 in scantling draft is depicted, including the generated recirculation in its wake. As it is clear from the two figures, stronger vorticity is observed in the case of KCS, because the wetted area of its transom is bigger for T_s. The remarkable increase of recirculation is verified from the absolute value of vorticity, which presents 80 % and 78 % increase of the maximum absolute vorticity for JBC and KVLCC2, respectively.

In Appendix E, analytical representation of the results is presented in Table E.1. Moreover, the analysis of transom submergence has been implemented also for the test cases of JBC, KCS and KVLCC2 in order to obtain visual insights of the flow onto the surface of these benchmark hulls (Figure E.1), in the disc of the propeller (Figure E.2) and in the wake of transom. The visualisation of streamlines onto the hull surface and the propeller's disc, as well as the wake distribution in its disc is presented for verification that the simulations are consistent with the physics and expected fluid behavior. As far as the streamlines on the surface are concerned, separation of the flow is observed in the two sides of the skeg of JBC and KVLCC2, which is also verified in the illustration of streamlines in the propeller's disc, since they enter the disc with turbulent behavior. On the contrary, there is no intense separation of the inflow of the propeller resulting in a laminar behavior of the streamlines. The existence of flow separation can be mainly attributed to the combination of low flow speed, which attacks the geometry of these certain skegs. Visual results of velocity and vorticity regarding two additional drafts are also depicted in Figure E.3, E.4, E.5 and E.6. Finally, it is clarified that the $k-\omega$ SST model has been used for the execution of simulations related to the systematic variation of transom submergence, as long as it is considered the most suitable turbulence model for F-S computations in FS.

Additional data about DTMB 5415 and ONRT test cases are given in Table F.1 of Appendix F. In particular, results regarding C_T, C_F and k are introduced and illustration of their discrepancy with the experimental data is made. In case of ONRT test case, no experimental data is found available.

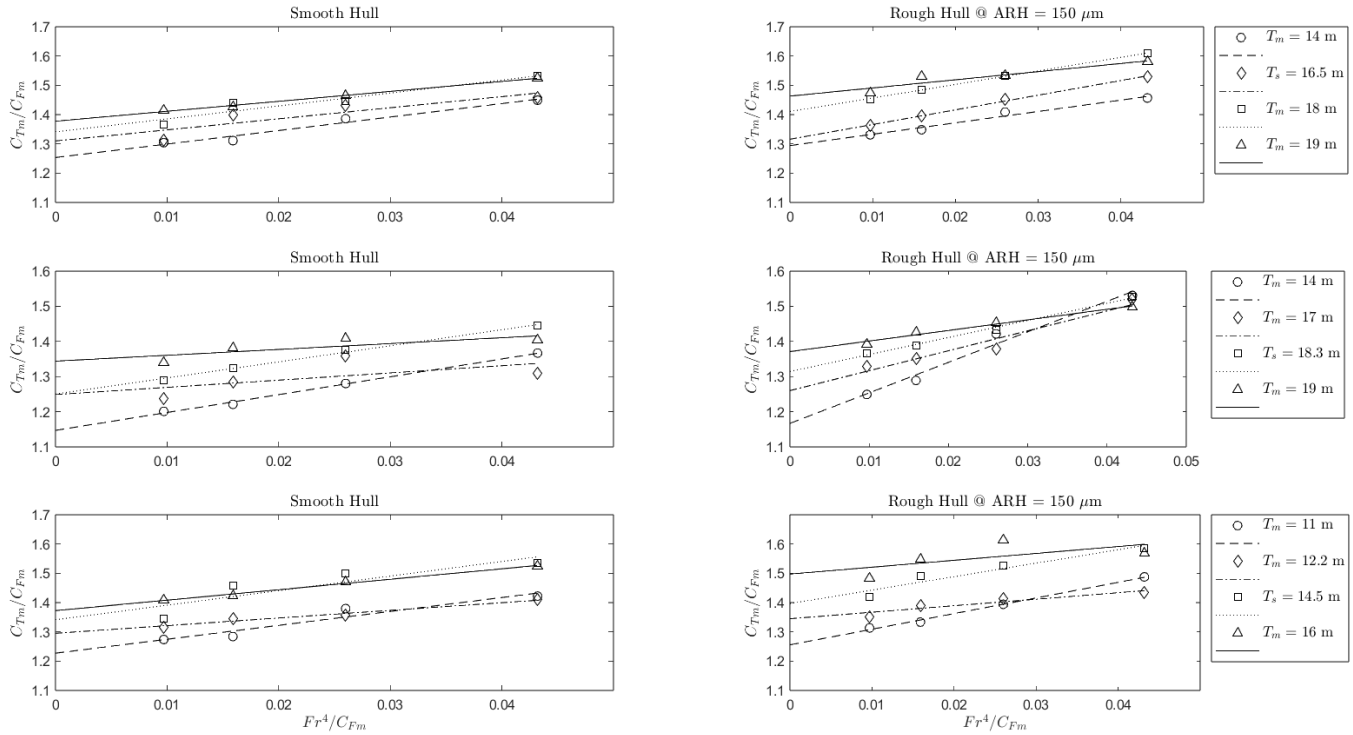

Figure 4.18: Sensitivity of C_{Tm}/C_{Fm} with variation of draft for the test cases of JBC, 180K BC and 82K BC (smooth + rough) in FS by using the Prohaska method and F-S model.
JBC (top), 180K BC (middle), 82K BC (bottom)

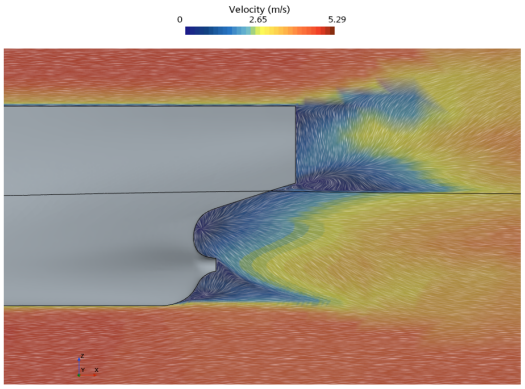

(a) $T_s = 16.5$ m (velocity)

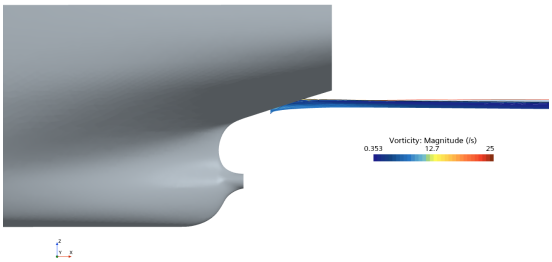

(b) $T_s = 16.5$ m (vorticity)

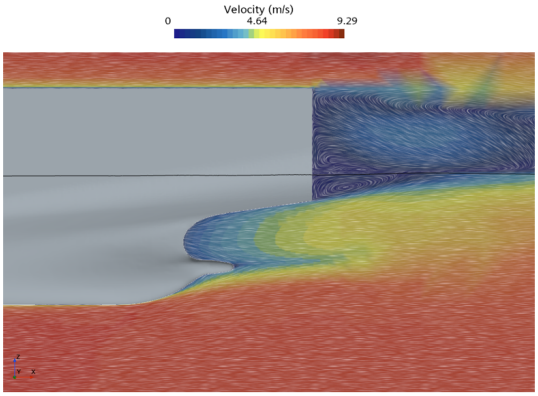

(c) $T_s = 10.5$ m (velocity)

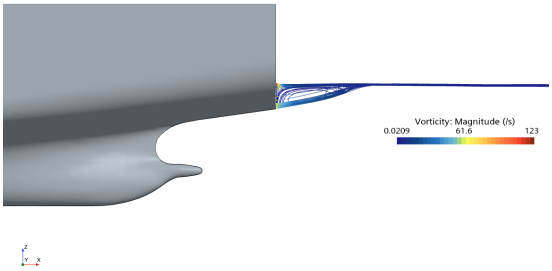

(d) $T_s = 10.5$ m (vorticity)

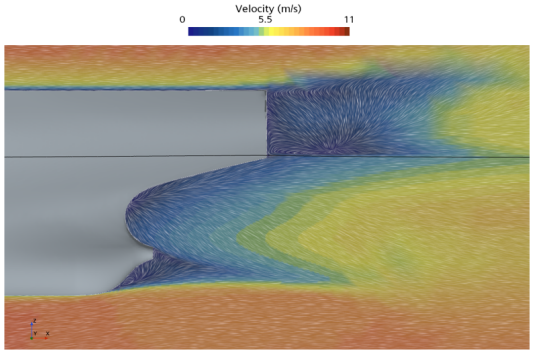

(e) $T_s = 20.8$ m (velocity)

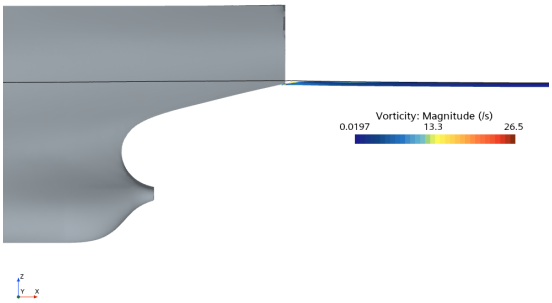

(f) $T_s = 20.8$ m (vorticity)

Figure 4.19: Local flow behind the transom of the JBC (a, b), KCS (c ,d) and KVLCC2 (e, f) test cases for T_s and $Fn = 0.1$ in FS (F-S, $k - \omega$ model).

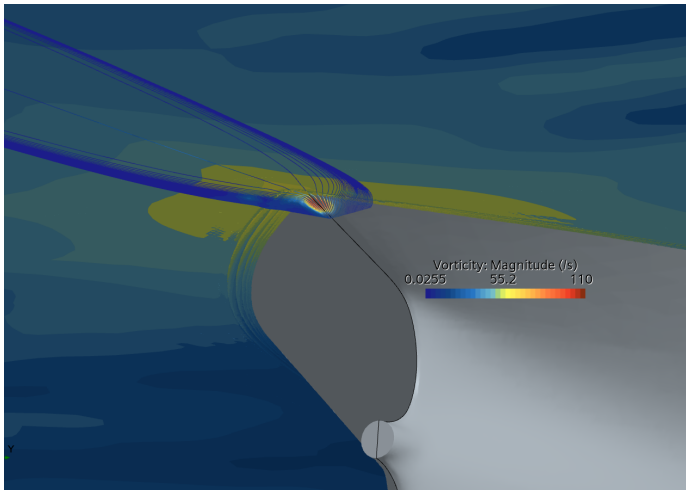

(a) JBC

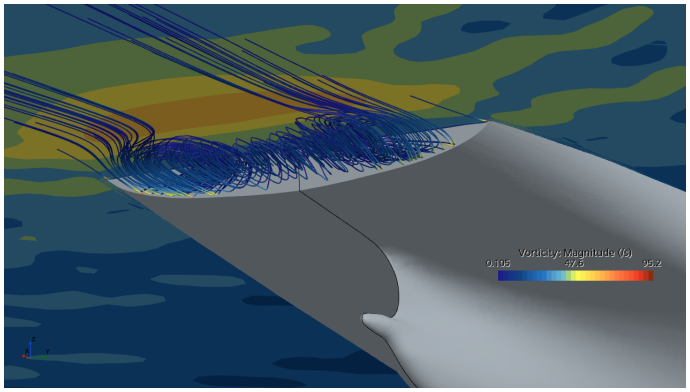

(b) KCS

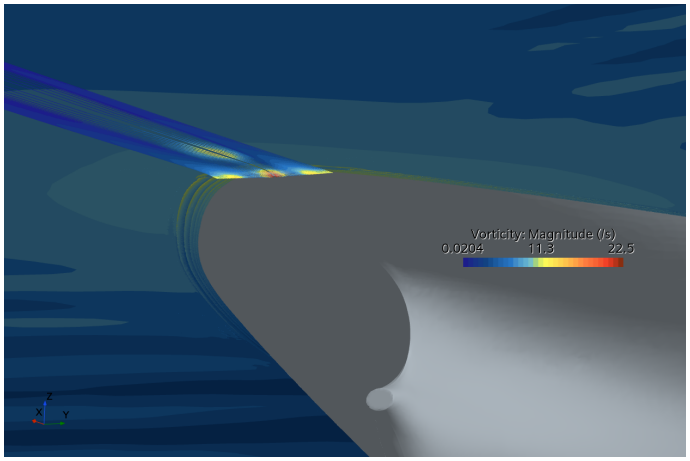

(c) KVLCC2

Figure 4.20: Recirculation of flow in the wake of transom of the JBC, KCS and KVLCC2 test cases for T_s and $Fn = 0.1$ in FS (F-S, $k - \omega$ model).

5

Conclusion and Future Work

This final chapter of the present project includes some concluding remarks according to the extracted results of the simulations, comparing them with the literature. Moreover, a final answer to the research question is given which represents and the total scope of this master thesis. Finally, recommendations for future research work regarding this topic and the field of ship hydrodynamics in general are presented.

5.1 Conclusion

The overall goal of this master's thesis has been to set up a series of CFD simulations in both model and full scale, testing one steady-state and one unsteady solver, as well as two turbulence models. Furthermore, an investigation of the effect of the form factor by changing the scaling of the five benchmark hulls and two commercial ones with intermediate levels of scaling, the roughness height of the surface of the aforementioned hulls in full scale, and the change of their draft in order to analyze the transom submergence have been conducted.

First of all, the V&V analysis executed for each implemented simulation of this thesis ensures that the level of uncertainty and error are acceptable, thus credibility of the CFD computations is established. As far as the verification study is concerned, the computational implementation of the executed simulations in both MS and FS is proved correct, since the uncertainty of grid convergence is in the acceptable limits resulting in low percentages of U_D. Also, the study of iterative errors for both turbulence models and scales show that there are not fluctuations and the resolution has a normal periodic behavior which leads to convergence of the results. Finally, based on the availability of EFD data, the simulations implemented for all the seven test cases are validated, satisfying the criterion of subsection 3.4.2.

Furthermore, as far as the pressure distribution and wave pattern are concerned, consistence of the results is verified. In particular, extraction of these two kind of results has been made in order for the reliability of the systematic analyses to be ensured. This can be considered as an alternative way for verification of the results which is necessary to be implemented. Based on the aforementioned results regarding pressure distribution, the comparison between the two used models, DB and F-S, has indicated a difference of the pressure contours. This can validate the different way of approaching the pressure variations around the hull surface of the three benchmark hulls due to the approximated way of field computation in the first case and the impact of free surface on the field variables in in the second case. Regarding the extracted data for the wave pattern, consistency of its formation is observed with a slight variation of wave length and wave elevation because of the different hull form among the three investigated benchmark vessels.

According to the systematic variation analyses implemented in the context of the present thesis,

the scaling sensitivity analysis shows a continuous reduction of resistance coefficients until a critical Re value. Further increase of scale until the full scale is reached results in negligible variation of the coefficients. This means that the extracted results have an asymptotic behavior and there is no effect of further increase of scaling on the final results of resistance components. In other words, independence of scale effects on resistance components over a critical Re number prevails. On the other hand, the sensitivity of form factor by changing scale factor shows an arbitrary trend for the intermediate values of scaling. This can be considered expected, because the form factor is not directly computed from the CFD simulations, but it is a derivative of the ratio between the C_F and C_T. Based on that, intense discrepancy between the CFD and experimental results is observed for all the test cases and scale factor apart from the MS and FS.

Furthermore, the roughness sensitivity analysis indicates the dependency of C_F, C_{VP} and C_V on the variation of Averaged Roughness Height. In this investigation a critical value of k_s over which the resistance coefficients do not present any oscillation exists. The fact that the roughness height exceeds the height of the first cell next to the wall creates this lack of resistance increase, which is not expected. As it is already mentioned in section 4.4, increase of first cell height and thus y^+ can lead to unreliability of the results. Constant behavior of k via change of k_s is also detected for $k_s > 250\ \mu m$. Moreover, regarding the systematic variation of draft and by extension the sensitivity study of transom submergence, the comparison of CFD and EFD data for the test cases of 180K BC and 82K BC indicates low discrepancy of k, especially for the T_s. In general, CFD-based form factor estimation in both MS and FS approximates to a high extent the EFD data and also verifies the applicability of Prohaska method. The higher discrepancy between the CFD and EFD results is due to the increased wetted area of transom, which leads to creation of vortices and intense turbulence flow, which promptly affect the resulted ratio C_T/C_F.

Taking into consideration all the aforementioned conclusions, the strengths, shortcomings and uncertainties regarding the executed CFD computations and the EFD data have been presented and discussed. This thesis has shown that the form factor can be derived from CFD simulations in model and full scale ensuring reliability of its estimation in relation to the available EFD data. Even though weaknesses still exist due to the approximating level of the k CFD-based estimation, the systematic analysis applied in this project indicate and verify the dependency of form factor on scale effects, hull roughness and draft variations, establishing the $2-k$ approach as an holistic and trustworthy method.

5.2 Future Work

Further studies and additional research work are needed so as to determine the impact of the change in scaling, roughness and transom submergence on CFD-based form factor prediction.

Future investigations of similar kind are suggested in order for the availability in experimental data regrading the several resistance components and form factor of the five used benchmark hulls to be increased, especially for the test case of ONRT. This can lead to a more comprehensive future research work and consequently more reliable results. Furthermore, it could set the CFD-based form factor estimations as the main technique replacing the model scale form factor extrapolation, which has a high level of uncertainty as an approximation method.

As far as the roughness analysis is concerned, more extended study is recommended including roughness functions to represent the surface roughness instead of using an equal distributed value along the

hull. Through this, a more realistic modelling method can be developed and the impact of different roughness heights in different regions of a hull, such as bulbous bow, transom or skeg, can be better predicted. Using a roughness function in specific regions of the hull, such as the transom, turbulent phenomena could obviously be captured and approximated, which are known to lead to the increase of friction resistance and as a result the increase of form factor.

Finally, regarding the sensitivity analysis of transom submergence applied in this thesis, a more detailed investigation of the produced recirculated flow in the wake of the transom would be considered beneficial, since it affects the total formation of the flow around the hull and the ratio between the total and frictional resistance. Specifically, more draft cases (i.e. loading conditions) worth to be studied with a deeper investigation in the vorticity phenomena, which can also create tremendous energy losses during the operation of the vessel.

Bibliography

[Hughes G. (1954)] Hughes, G. (1954). Friction and Form Resistance in Turbulent Flow, and a Proposed Formulation for Use in Model and Ship Correlation. R. I. N. A. 96.

[Prohaska C. W. (1966)] Prohaska, C., W. (1966). A Simple Method for the Evaluation of the Form Factor and Low Speed Wave Resistance. Proceeding of 11th ITTC.

[Korkmaz K.B. et al. (2020)] Korkmaz, K.B., Werner, S., Sakamoto, N., Queutey, P., Deng, G., Yuling, G., Guoxiang, D., Maki, K., Ye, H., Akinturk, A., Sayeed, T., Hino, T., Zhao, F., Tezdogan, T., Demirel, Y.K., Bensow, R., (2020). CFD-based form factor determination method, Elsevier, Ocean Engineering 220 (2021) 108451.
https://doi.org/10.1016/j.oceaneng.2020.108451

[Korkmaz K.B. et al. (2022)] Korkmaz, K.B., Werner, S., Bensow, R., (2022). Scaling of wetted-transom resistance for improved full-scale ship performance predictions, Elsevier, Ocean Engineering 266 (2022) 112590.
https://doi.org/10.1016/j.oceaneng.2022.112590

[Korkmaz K.B. et al. (2021)] Korkmaz, K.B., Werner, S., Bensow, R., (2021). Verification and Validation of CFD based Form Factors as a Combined CFD/EFD Method, Journal of Marine Science and Engineering 2021, 9, 75.
https://doi.org/10.3390/jmse9010075

[Mikkelsen H.,L. et al. (2019)] Mikkelsen, H., L. Steffensen, M., Ciortan, C., Walther, J. H. (2019). Ship scale validation of CFD model of selfpropelled ship. In R. Bensow, J. Ringsberg (Eds.), MARINE 2019 Computational Methods in Marine Engineering VIII (pp. 718-729). International Center for Numerical Methods in Engineering.

[Terziev M. et al. (2021)] Terziev, M., Tezdogan, T., Demirel, Y., K., Villa, D. , Mizzi, S., Incecik, A. (2021). Exploring the effects of speed and scale on a ship's form factor using CFD, Science Direct, International Journal of Naval Architecture and Ocean Engineering, 2092-6782/© 2021 Society of Naval Architects of Korea.
https://doi.org/10.1016/j.ijnaoe.2020.12.002

[Mikkelsen, H. et al. (2020)] Mikkelsen, H., Walther, J. H. (2020). Effect of roughness in full-scale validation of a CFD model of self-propelled ships, Elsevier, Applied Ocean Research 99 (2020) 102162.
https://doi.org/10.1016/j.apor.2020.102162

[Korkmaz K.B. (2022)] Korkmaz, K.B., Improved Power Predictions of Ships Using Combined CFD/EFD Methods for the Form Factor, (2022). Thesis for the degree of Licentiate of Engineering in Shipping and Marine Technology.
https://research.chalmers.se/publication/521155/file/521155_Fulltext.pdf

[Yao J. X. et al. (2021)] Yao, J., X., Liu, Z., Song, X., Su, Y., (2021). Ship maneuvering prediction with hydrodynamic derivatives from RANS: Development and application. Ocean. Eng. 2021, 231, 109036.
https://doi.org/10.1016/j.oceaneng.2021.109036

[Lee J. et al. (2020)] Lee, J., Kim, Y., (2020). Study on steady flow approximation in turning simulation of ship in waves, Ocean Engineering, Volume 195, 2020, 106645, ISSN 0029-8018. https://doi.org/10.1016/j.oceaneng.2019.106645

[JBC, Tokyo (2015)] JAPAN Bulk Carrier (JBC), (2015). Tokyo 2015: a Workshop on CFD in Ship Hydrodynamics, December 2-4, Tokyo. https://www.t2015.nmri.go.jp/jbc_gc.html

[KCS, Tokyo (2015)] KRISO Container Ship, (2015). Tokyo 2015: a Workshop on CFD in Ship Hydrodynamics, December 2-4, Tokyo. https://www.t2015.nmri.go.jp/kcs_gc.html

[KVLCC2, Tokyo (2015)] MOERI Tanker KVLCC2, (2015). Tokyo 2015: a Workshop on CFD in Ship Hydrodynamics, December 2-4, Tokyo. http://www.simman2008.dk/KVLCC/KVLCC2/kvlcc2_link.htm

[DTMB 5415, Gothenburg (2010)] US Navy Combatant DTMB5415, (1980). Gothenburg 2010: a Workshop on Numerical Ship Hydrodynamics. http://www.simman2008.dk/5415/5415_geometry.htm

[ONRT, Tokyo (2015)] ONR Tumblehome Ship, (2013). Tokyo 2015: a Workshop on CFD in Ship Hydrodynamics, December 2-4, Tokyo. https://www.t2015.nmri.go.jp/onrt_gc.html

[ITTC (2017)] ITTC, (2017). Recommended Procedures and Guidelines, 1978 ITTC Performance Prediction Method, 7.5–02-03–01.4 https://www.ittc.info/media/8017/75-02-03-014.pdf

[Carlton J. S. (2019)] Carlton, J., S. (2019). Marine Propellers and Propulsion, 4th ed. Elsevier, ISBN:978-0-08-100366-4 https://www.elsevier.com/books/marine-propellers-and-propulsion/carlton/978-0-08-100366-4

[ITTC (1957)] ITTC, (1957). Subjects 2 and 4 Skin Friction and Turbulence Stimulation. International Towing Tank Conference: Madrid, Spain.

[ITTC (1969)] ITTC, (1969). Report of Performance Committee. https://ittc.info/media/3267/rpec.pdf

[ITTC (1978)] ITTC, (1978). Report of Performance Committee. https://ittc.info/media/2859/report-of-performance-committee.pdf

[ITTC (Revision 2017) (1978)] ITTC, (1978) ITTC Performance Prediction Method. Recommended Procedures and Guidelines 7.5-02-03-01.4 (Revision 04 2017). https://www.ittc.info/media/8017/75-02-03-014.pdf

[SSPA] SSPA: Your Maritime Solution Partner. Fiskargatan 8, SE- 116 20 Stockholm, Sweden. https://www.sspa.se/en

[Larsson, L. et al. (2010)] Larsson, L., Raven, C., H. Ship and Resistance Flow, Principles of Naval Architecture Series (2010). SNAME, USA, ISBN 978-0-939773-76-3

[Grigson C. W. B. (1993)] Grigson, C. W. B. (1993). A planar friction algorithm and its use in analysing hull resistance. Transactions of the Royal Institute of Naval Architects, 76–115.

[Katsui T. (2005)] Katsui, T., Asai, H., Himeno, Y., Tahara, Y. (2005). The proposal of a new friction line. Proceedings of the 5th Osaka Colloquium on Advanced CFD Applications to Ship Flow and Hull Form Design (pp. 76–83). Osaka, Japan.

[Hughes G. (1952)] Hughes, G. (1952). Frictional resistance of smooth plane surfaces in turbulent flow. Transactions of the Institute of Naval Architects, 94.

[Hughes G. (1954)] Hughes, G. (1954). Friction and form resistance in turbulent flow and a proposed formulation for use in model and ship correlation. Transactions of the Institute of Naval Architects, 96.

[Eca L. et al. (2008)]eca1Eca, L., & Hoekstra, M. (2008). The numerical friction line. Journal of Marine Science and Technology, 13-4, 328–345.
https://doi.org/10.1007/s00773-008-0018-1

[Watanabe K. (1973)] Watanabe, K. (1973). Note to the Performance Committee.
https://ittc.info/media/3267/rpec.pdf

[Toki N. (2008)] Toki, N. (2008). Investigation on Correlation Lines through the Analyses of Geosim Model Test Results. Journal of the Japan Society of Naval Architects and Ocean Engineers 8, 71-79.
https://www.jstage.jst.go.jp/article/jjasnaoe/8/0/8_0_71/_pdf/-char/ja

[Raven, H., C., A. et al. (2008)] Raven, H., C., A., Van der Ploeg A., Starke, R. and Eca, L. (2008). Towards a CFD-based prediction of ship performance - Progress in predicting full-scale resistance and scale effects. International Journal of Maritime Engineering Transactions of the Royal Institution of Naval Architects Part A.
https://www.academia.edu/65631100/Prediction_of_ship_resistance_with_the_use_of_Full_scale_CFD_simulations

[Versteeg H. K. et al. (2007)] Versteeg, H. K., & Malalasekera, W. (2007). An introduction to computational fluid dynamics: the finite volume method. Pearson education.
http://ftp.demec.ufpr.br/disciplinas/TM702/Versteeg_Malalasekera_2ed.pdf

[Wilcox D. C. (1994)] Wilcox, D.C. (1994). Turbulence modelling for CFD, DCW Industries, California, USA.

[Towsin & Mosaad (1985)] Townsin, R. L., Mosaad, M. A. (1985). The ITTC line-its genesis and correlation allowance.
https://trid.trb.org/view/427976

[Zou L. et al. (2012)] Zou L., Larsson, L. , Orych, M. (2012) Verification and validation of CFD predictions for a manoeuvring tanker. ScienceDirect, 9th International Conference on Hydrodynamics, October 11-15, 2010 Shanghai, China.
https://www.academia.edu/6674388/Verification_and_validation_of_CFD_predictions_for_a_manoeuvring_tanker

[Eça L. et al. (2002)] Eça L, Hoekstra M. (2002) An Evaluation of Verification Procedures for CFD Applications, 24th Symposium on Naval Hydrodynamics [C]. Fukuoka, Japan. https://nap.nationalacademies.org/read/10834/chapter/39

[STAR-CCM+ (2023)] Simcenter STAR-CCM+ | Siemens Software (2023).
https://plm.sw.siemens.com/en-US/simcenter/fluids-thermal-simulation/star-ccm/

[Hino T. et al. (2020)] Hino, T., Stern, F., Larsson, L., Visonneau, M., Hirata, N., Kim, J. (Eds.). (2020). Numerical ship hydrodynamics: an assessment of the Tokyo 2015 Workshop (Vol. 94). Springer Nature.

[Larsson L. et al. (2013)] Larsson, L., Stern, F., Visonneau, M. (2013). CFD in ship hydrodynamics—results of the Gothenburg 2010 workshop. In MARINE 2011, IV International Conference on Computational Methods in Marine Engineering: Selected Papers (pp. 237-259). Springer Netherlands.

[ITTC (Revision 2008) (1978)] ITTC, 1978 ITTC - Performance prediction method. ITTC - Recommended procedures and guidelines, Procedure 7.5-02-03-01.4, Revision 01, 2008.
https://ittc.info/media/1593/75-02-03-014.pdf

[Cebeci and Bradshaw (1977)] Cebeci, T., Bradshaw, P. (1977). Momentum transfer in boundary layers, Hemisphere Publishing Corporation/McGraw-Hill.
https://ui.adsabs.harvard.edu/abs/1977hemi.book.....C/abstract

[Huang et al. (2023)] Huang, L., Pena, B., Giles, T. (2023). Towards a full-scale CFD guideline for simulating a ship advancing in open water.

[Eça L. et al. (2014)] Eça, L., Hoeksra, M. (2014). A procedure for the estimation of the numerical uncertainty of CFD calculations based on grd refinement studies, Elsevier, Journal of Computational Physics 262 (2014) 104–130
http://dx.doi.org/10.1016/j.jcp.2014.01.006

[MARIN Tool (2022)] Verification Tools from MARIN (2022).
https://www.marin.nl/en/research/free-resources/verification-and-validation/verification-tools

[Eca L. et al. (2019)] L. Eca, G. Vaz, S.L. Toxopeus, M. Hoestra (2019). Numerical Errors in Unsteady Flow Simulations, Journal of Verification, Validation and Uncertainty Quantification, Vol. 4, ASME

A

Appendix: Characteristics of prism layering in model and full scale

Table A.1: Characteristics of prism layering for each studied hull in model scale for $y^+ = 50$.

Characteristics	**Test Cases**						
	JBC	KCS	KVLCC2	DTMB5415	ONRT	180K BC	82K BC
λ	40.00	37.89	45.71	24.83	48.94	36.82	29.63
T_H [m]	0.12	0.18	0.20	0.04	0.02	0.04	0.03
$10^{-5}y$ [m]	1.95	17.90	263.00	8.50	2.10	2.14	1.90
λ_s	1.20						
N	6						

Table A.2: Characteristics of prism layering for each studied hull in full scale for $y^+ = 200$.

Characteristics	**Test Cases**						
	JBC	KCS	KVLCC2	DTMB 5415	ONRT	180K BC	82K BC
T_H [m]	1.62	1.40	3.29	1.00	1.05	1.61	1.36
$10^{-4} \cdot y$ [m]	7.93	9.00	140.00	21.00	10.00	8.00	9.00
λ_s	1.10						
N	12						

B

Appendix: Verification analysis of grid refinement h_i/h_1

Table B.1: Verification analysis of grid refinement for JBC.

Scale	Turbulence Model	h_1/h_i	Base Size	Number of Cells	C_F	C_{VP}	C_V	k
FS	k-ω SST	1.00	18	2.01×10^4	0.0768	0.0241	0.101	1.316
		1.18	22	1.24×10^4	0.0767	0.0244	0.1011	1.318
		1.39	26	7.39×10^4	0.0762	0.0247	0.1009	1.324
		1.65	32	4.52×10^6	0.0766	0.0254	0.1020	1.331
		1.94	40	2.75×10^6	0.0752	0.0250	0.1002	1.332
	Realizable k-ϵ	1.00	18	2.01×10^4	0.0750	0.0230	0.0980	1.308
		1.18	22	1.24×10^7	0.0750	0.0230	0.0980	1.306
		1.39	26	7.39×10^4	0.0753	0.0233	0.098	1.309
		1.65	32	4.52×10^4	0.0731	0.0231	0.0962	1.316
		1.94	40	2.75×10^4	0.0782	0.0240	0.1021	1.307
MS	k-ω SST	1.00	18	9.93×10^6	0.1711	0.0641	0.2352	1.374
		1.18	22	6.11×10^6	0.1655	0.0636	0.2291	1.384
		1.39	26	3.65×10^6	0.1704	0.0631	0.2334	1.370
		1.65	32	2.24×10^6	0.1723	0.0637	0.2360	1.370
		1.94	40	1.36×10^6	0.1857	0.0669	0.2479	1.335
	Realizable k-ϵ	1.00	18	9.93×10^6	0.1625	0.0616	0.2241	1.379
		1.18	22	6.11×10^6	0.1579	0.0633	0.2213	1.401
		1.39	26	3.65×10^6	0.1568	0.0609	0.2177	1.389
		1.65	32	2.24×10^6	0.1600	0.0613	0.2213	1.383
		1.94	40	1.36×10^6	0.1572	0.0590	0.2162	1.375

C

Appendix: Sensitivity analysis of form factor for different scale factors

Table C.1: Sensitivity of form factor for different scale factors for JBC.

λ [-]	L_{WL} [m]	V $[m/s]$	Re [-]	C_{VP} [-]	C_T [-]	C_F [-]	k [-]
1	285.00	5.29	1.322×10^9	68.06×10^3	27.32×10^3	20.51×10^3	1.332
2	142.50	3.74	4.674×10^8	30.17×10^3	60.70×10^3	30.53×10^3	1.988
4	71.25	2.64	1.652×10^8	4.59×10^3	8.90×10^3	4.31×10^3	2.065
8	35.63	1.87	5.842×10^7	285.88	921.78	635.90	1.450
16	17.81	1.32	2.065×10^7	32.26	125.41	93.15	1.346
20	14.25	1.18	1.478×10^7	17.27	67.50	50.2	1.344
30	9.50	0.97	8.045×10^6	6.25	22.5	16.3	1.384
40	7.13	0.87	5.225×10^6	2.54	10.43	7.81	1.335

Table C.2: Sensitivity of form factor for different scale factors for KCS.

λ [-]	L_{WL} [m]	V $[m/s]$	Re [-]	C_{VP} [-]	C_T [-]	C_F [-]	k [-]
1	232.50	4.78	9.740×10^8	9.67×10^3	96.32×10^3	86.66×10^3	1.112
2	116.25	3.38	3.444×10^8	17.49×10^3	34.14×10^3	16.65×10^3	2.05
4	58.13	2.39	1.218×10^8	2.23×10^3	4.58×10^3	2.35×10^3	1.947
8	29.06	1.69	4.305×10^7	592.60	340.03	252.55	1.346
16	14.53	1.19	1.522×10^7	31.93	81.60	49.67	1.643
25	9.30	0.96	7.792×10^7	7.32	21.98	14.66	1.499
37.89	6.14	0.78	4.176×10^6	0.38	4.24	3.84	1.105

Table C.3: Sensitivity analysis of form factor for different scale factors for KVLCC2.

λ [-]	L_{WL} [m]	V $[m/s]$	Re [-]	C_{VP} [-]	C_T [-]	C_F [-]	k [-]
1	325.50	5.65	1.613×10^9	75.98×10^3	12.37×10^4	99.25×10^3	1.247
2	162.75	4.00	5.704×10^8	15.31×10^3	65.60×10^3	50.28×10^3	1.305
4	81.38	2.83	2.017×10^8	2.19×10^3	9.31×10^3	7.12×10^3	1.307
8	40.69	2.00	7.131×10^7	296.97	1.31×10^3	1.02×10^3	1.292
16	20.34	1.41	2.521×10^7	49.64	196.45	146.81	1.338
23	14.15	1.18	1.463×10^7	12.19	70.29	53.86	1.305
31	10.50	1.01	9.348×10^6	7.36	30.78	23.42	1.314
45.714	7.12	0.84	5.220×10^6	2.53	10.82	8.24	1.313

D

Appendix: Sensitivity analysis of roughness k_s

Table D.1: Sensitivity analysis of roughness.

	JBC				KCS				KVLCC2			
k_s $[\mu m]$	$10^4 R_T$	$10^4 R_{VP}$	$10^4 R_F$	k	$10^4 R_T$	$10^4 R_{VP}$	$10^4 R_F$	k	$10^4 R_T$	$10^4 R_{VP}$	$10^4 R_F$	k
150	31.83	7.88	23.95	1.329	11.12	1.07	10.05	1.106	45.82	8.71	37.11	1.235
200	33.30	8.21	25.08	1.328	11.64	1.10	10.53	1.105	47.89	9.05	38.84	1.233
250	34.68	8.48	26.19	1.324	12.06	1.13	10.92	1.104	49.28	9.23	40.04	1.231
300	34.64	8.47	26.17	1.324	12.21	1.14	11.06	1.104	49.42	9.27	40.14	1.231
350	34.68	8.48	26.19	1.324	12.22	1.14	11.07	1.104	49.47	9.28	40.19	1.231
400	34.74	8.50	26.23	1.324	12.24	1.15	11.09	1.104	49.47	9.28	40.19	1.231
450	34.74	8.50	26.23	1.324	12.26	1.15	11.10	1.104	49.47	9.28	40.19	1.231
500	34.74	8.50	26.23	1.324	12.28	1.16	11.12	1.100	49.47	9.28	40.19	1.231

E

Appendix: Systematic variation of transom submergence

Table E.1: Systematic variation of transom submergence for JBC and the two commercial hulls.

		Smooth Hull						Rough Hull @ ARH = 150 μm					
		MS			FS			MS			FS		
	T_m [m]	C_{Tm} [-]	C_{Fm} [-]	k [-]	C_{Ts} [-]	C_{Fs} [-]	k [-]	C_{Tm} [-]	C_{Fm} [-]	k [-]	C_{Ts} [-]	C_{Fs} [-]	k [-]
JBC	14.0	0.0876	0.0702	1.248	0.0297	0.0226	1.313	0.1029	0.0785	1.311	0.0368	0.0251	1.469
	16.5	0.1020	0.0768	1.329	0.0347	0.0248	1.399	0.1075	0.0797	1.349	0.0453	0.0279	1.622
	18.0	0.0985	0.0796	1.403	0.0413	0.2671	1.531	0.1138	0.0815	1.396	0.0447	0.0315	1.419
	19.0	0.1303	0.0824	1.581	0.0474	0.0285	1.663	0.1294	0.0839	1.542	0.0459	0.0333	1.380
180K BC	14.0	0.0867	0.0715	1.170	0.0315	0.0242	1.281	0.0913	0.0727	1.256	0.0368	0.0274	1.342
	17.0	0.0887	0.0736	1.205	0.0332	0.0256	1.298	0.0905	0.0736	1.230	0.0379	0.0281	1.350
	18.0	0.0947	0.0777	1.219	0.0369	0.0284	1.298	0.0977	0.0759	1.287	0.0413	0.0296	1.395
	19.0	0.0986	0.0806	1.223	0.0391	0.0296	1.320	0.1020	0.0785	1.299	0.0424	0.0307	1.380
82K BC	11.0	0.0747	0.0665	1.123	0.0254	0.0204	1.248	0.0792	0.0674	1.175	0.0300	0.0231	1.301
	12.2	0.0793	0.0678	1.170	0.0281	0.0223	1.258	0.0837	0.0682	1.227	0.0320	0.0244	1.313
	14.5	0.0869	0.0695	1.251	0.0337	0.0245	1.374	0.0893	0.0698	1.280	0.0353	0.0252	1.399
	16.0	0.0930	0.0724	1.285	0.0355	0.0258	1.375	0.0993	0.0752	1.321	0.0378	0.0267	1.415

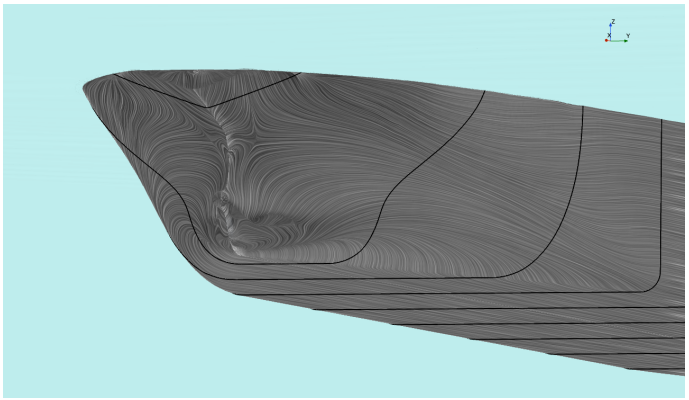

(a) JBC

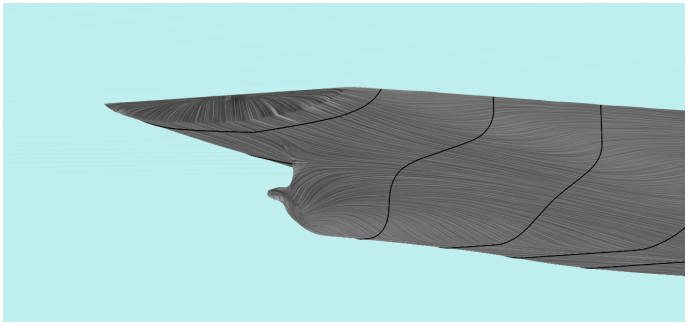

(b) KCS

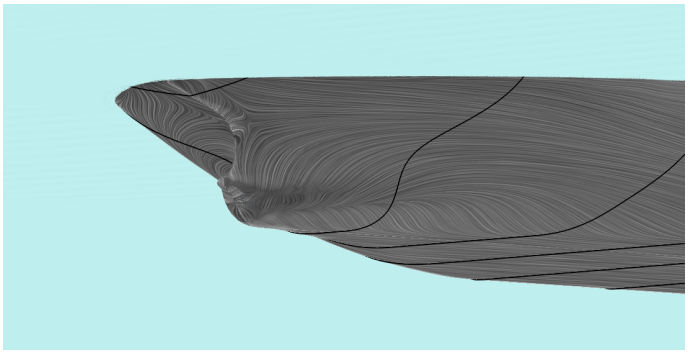

(c) KVLCC2

Figure E.1: Streamlines onto the surface of the JBC, KCS and KVLCC2 test cases for T_s and $Fn = 0.1$ in FS (F-S, $k - \omega$ model).

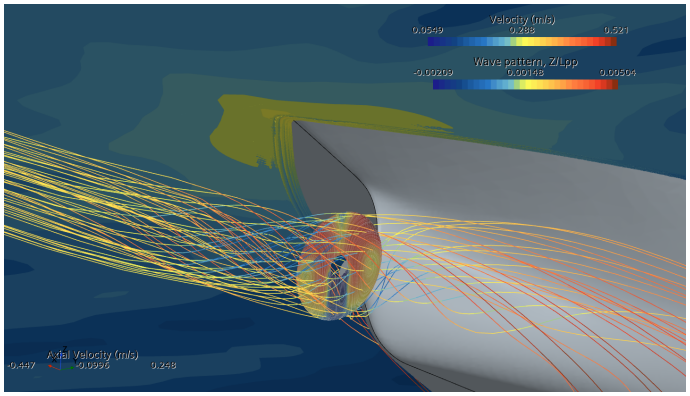

(a) JBC

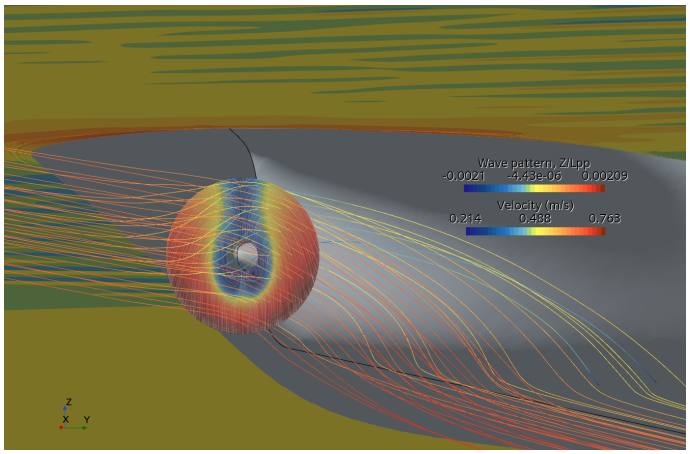

(b) KCS

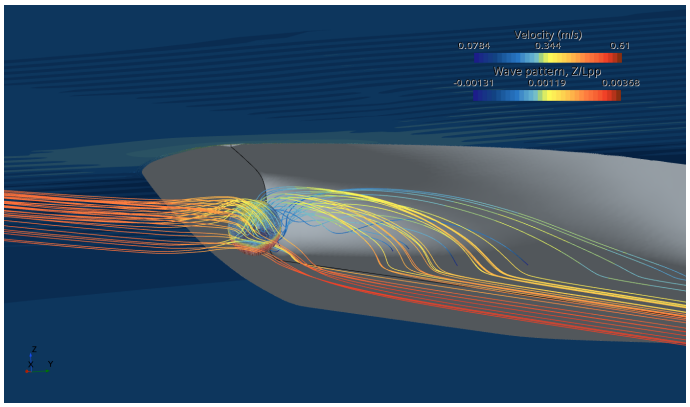

(c) KVLCC2

Figure E.2: Streamlines and wake distribution in the disc of propeller of the JBC, KCS and KVLCC2 test cases for T_s and $Fn = 0.1$ in FS (F-S, $k - \omega$ model).

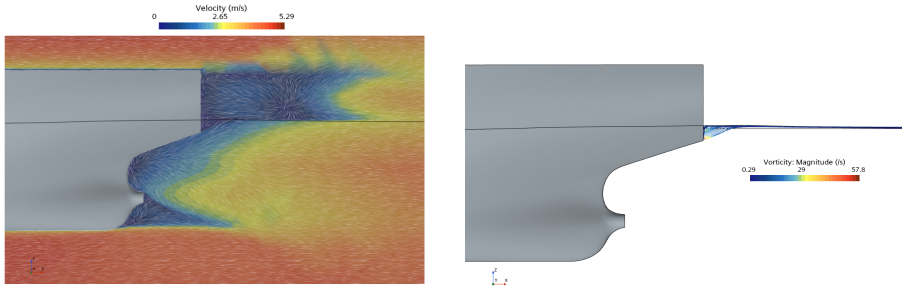

(a) T = T_s + 1 m (velocity) **(b)** T_s + 1 m (vorticity)

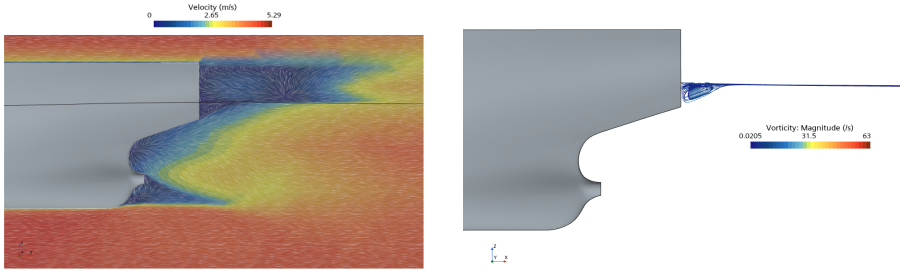

(c) T = T_s + 2 m (velocity) **(d)** T = T_s + 2 m (vorticity)

Figure E.3: Local flow behind the transom of JBC for $Fn = 0.1$ in FS (F-S, $k - \omega$ mode).

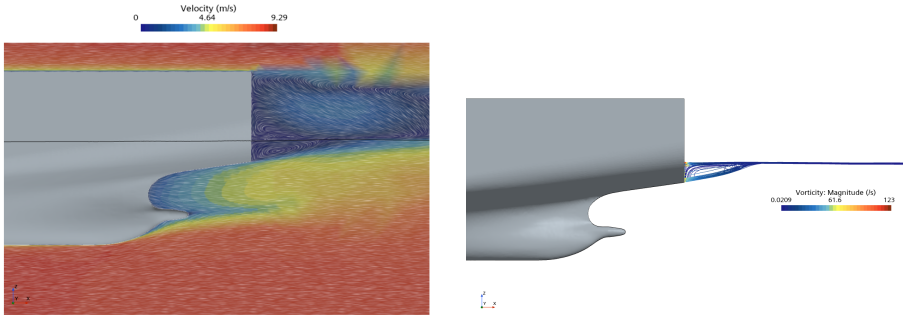

(a) T = T_s + 1 m (velocity) **(b)** T_s + 1 m (vorticity)

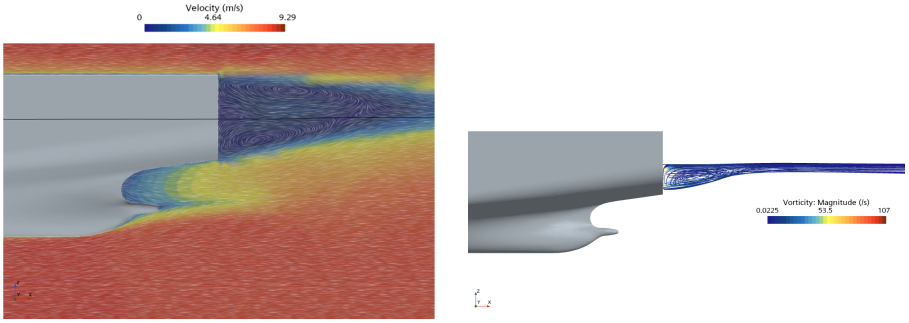

(c) T = T_s + 2 m (velocity) **(d)** T = T_s + 2 m (vorticity)

Figure E.4: Local flow behind the transom of KCS for $Fn = 0.1$ in FS (F-S, $k - \omega$ model).

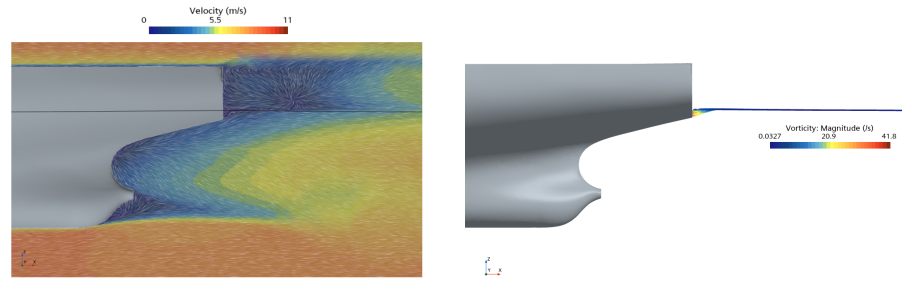

(a) T = T_s + 1 m (velocity) **(b)** T_s + 1 m (vorticity)

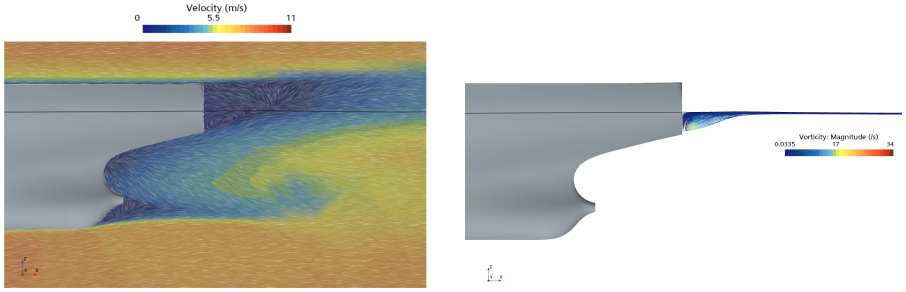

(c) T = T_s + 2 m (velocity) **(d)** T = T_s + 2 m (vorticity)

Figure E.5: Local flow behind the transom of KVLCC2 for $Fn = 0.1$ in FS (F-S, $k - \omega$ model).

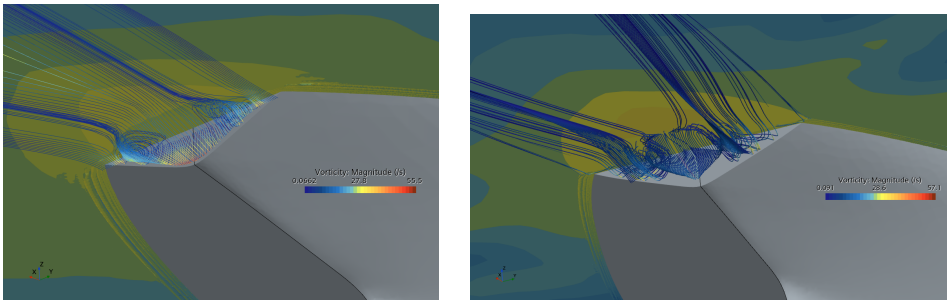

(a) T = T_s + 1 m (JBC) **(b)** T = T_s + 2 m (JBC)

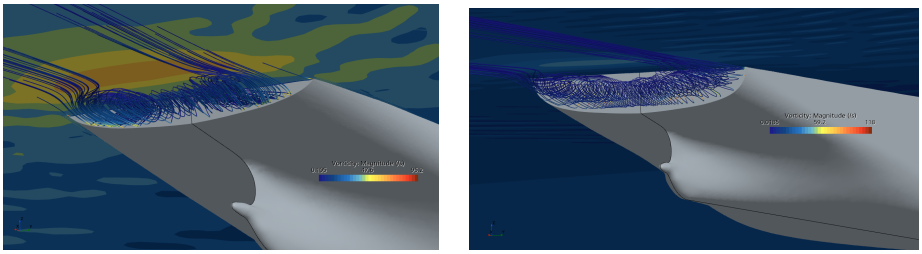

(c) T = T_s + 1 m (KCS) **(d)** T = T_s + 2 m (KCS)

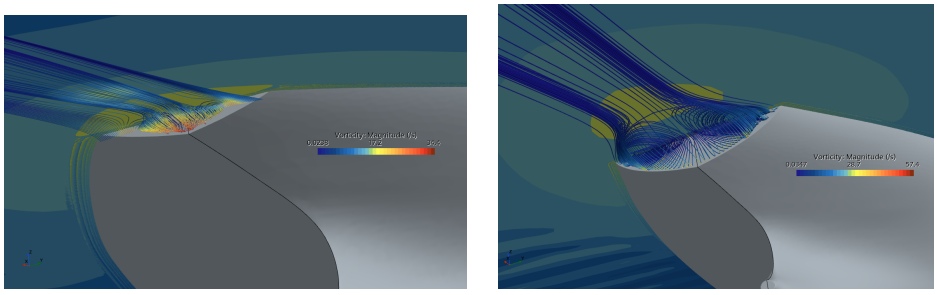

(e) T = T_s + 1 m (KVLCC2) **(f)** T = T_s + 2 m (KVLCC2)

Figure E.6: Vorticity behind the transom of the three test cases for $Fn = 0.1$ in FS (F-S, $k - \omega$ mode).

F

Appendix: DTMB 5415 and ONRT: Form Factor Results

Table F.1: Extracted CFD results for the test cases of DTMB 5415 and ONRT.

Test Case	Scale	Turbulence Model	No. of Cells	y^+	C_T [-]	C_F [-]	k (CFD)	k (EFD)	Discrepancy [%]
DTMB 5415	FS	k-ω SST	2.55×10^5	200	0.007795	0.006418	1.215	1.121	-2.72 %
		Realizable k-ϵ	2.55×10^5		0.007917	0.006528	1.213		7.66 %
	MS	k-ω SST	5.02×10^4	20	0.004579	0.004037	1.134		-1.27 %
		Realizable k-ϵ	5.02×10^4		0.003886	0.003378	1.150		-2.72 %
ONRT	FS	k-ω SST	2.84×10^5	200	0.007165	0.004480	1.174	-	-
		Realizable k-ϵ	2.84×10^5		0.007192	0.003696	1.177		
	MS	k-ω SST	2.13×10^4	20	0.004962	0.006105	1.107		
		Realizable k-ϵ	2.13×10^4		0.004177	0.006113	1.13		

DEPARTMENT OF MECHANICS AND MARITIME SCIENCES
CHALMERS UNIVERSITY OF TECHNOLOGY
Gothenburg, Sweden
www.chalmers.se

DEPARTMENT OF MECHANICAL ENGINEERING
TECHNICAL UNIVERSITY OF DENMARK
Kongens Lyngby, Denmark
www.dtu.dk

CHALMERS
UNIVERSITY OF TECHNOLOGY